COLOUR RETINAL IMAGE SEGMENTATION FOR COMPUTER-AIDED FUNDUS DIAGNOSIS

QIN LI

Doctor of Philosophy

The Hong Kong Polytechnic University

2010

The Hong Kong Polytechnic University

Department of Computing

Colour Retinal Image Segmentation for Computer-aided Fundus Diagnosis

Qin LI

A thesis submitted in partial fulfillment of the requirements for the Degree of Doctor of Philosophy

October 2009

CERTIFICATE OF ORIGINALITY

I hereby declare that this thesis is my own work and that, to the best of my knowledge and belief, it reproduces no material previously published or written, nor material that has been accepted for the award of any other degree or diploma, except where due acknowledgement has been made in the text.

_____ (Signed)

Qin LI (Name of Student)

Abstract

Colour images of the ocular fundus, or retinal images, captured using digital fundus cameras reveal to us the retinal, ophthalmic, systemic diseases such as diabetes, hypertension, and arteriosclerosis and provide a non-intrusive way to screen retinopathy. Automated segmentation of colour retinal images can help ophthalmologists, oculists, or eye-care specialist to screen larger populations. The meaningful objects to be segmented include the main regions of the retina and the lesions caused by certain diseases. The appearance of certain lesions can be the sign of certain retinal diseases and systemic diseases. The main regions of the retina are the optic disc, fovea, and blood vessels. The identification of these regions can help in the analysis of diseases that affect these regions preferentially, such as glaucoma and proliferative diabetic retinopathy. The locations of these regions can then in turn also help in locating other lesions.

The work in this thesis is in two parts. The first part addresses the segmentation of blood vessels, which are critical diagnostic features. The second part of this thesis proposes a system for segmenting the main regions and lesions of colour retinal images obtained from patients with diabetic retinopathy (DR).

Retinal vessel segmentation: Automated retinal segmentation is difficult due to the fact that the width of retinal vessels can vary from very large to very small, and that the local intensity contrast of vessels can be weak and unstable. In this thesis, we will present a simple but efficient multiscale scheme, Multiscale Production of the Matched Filter (MPMF), that uses responses as the multiscale data fusion strategy. The proposed MPMF vessel extraction scheme includes: (1) multiscale matched filtering and scale multiplication in the image enhancement step; and (2) double

thresholding in the vessel classification step. The fact that vessel structures have stronger responses to the matched filters at different scales than background noise means that multiplying the responses of matched filters at several scales enhances vessels while suppressing noise.

Another difficulty of vessel segmentation is from the affection of lesions. For example, if we need to find the dark lines in an image, the edges of bright blobs will be the major source of false line detection. Consequently, some blobs (bright lesions and the optic disc) in the retinal image may cause false detection of vessels. In this thesis, we propose a modified matched filter to suppress the false detection caused by bright blobs. The proposed modified matched filter does not respond to non-line edges and so significantly reduces the false detection of vessels.

Diabetic Retinopathy (DR) image segmentation: The objects useful for DR diagnosis include retinal lesions such as red lesions (intraretinal hemorrhages, microaneurysms), bright lesions (hard exudates and cottonwool spots) and retinal main regions such as vessels, optic disc, and fovea. Colour retinal image segmentation to assist DR diagnosis has attracted many researchers these years. But few works have been designed to extract all of these objects in one efficient scheme.

The major disadvantages of current colour retinal image segmentation works are (1) they do not take into account the correlation among different objects and this leads to many false positives; (2) the algorithms are too time-consuming so that the online application is impossible. In this thesis, we propose one efficient scheme that segments all useful objects for DR diagnosis. Our segmentation scheme answers these issues by organizing the segmentation all objects in one efficient workflow. This scheme suppresses false positives effectively and improves segmentation speed.

The segmentation speed is further improved by algorithm optimization and by keeping the algorithm as simple as possible.

Publications arising from the thesis

Book Chapter

[1] Q. Li, X.M. Jin, Q.X. Gao, J. You and P. Bhattacharya, "Screening diabetic retinopathy through color retinal images," *Computer Science Lecture Notes, LNCS* 4901, Springer-Verlag, Berlin Heidelberg, pp. 176-183, 2007.

Referred Journal Article

[2] M. Niemeijer, B. van Ginneken, M. J. Cree, A. Mizutani, G. Quellec, C. I. Sánchez, B. Zhang, R. Hornero, M. Lamard, C. Muramatsu, X. Q. Wu, G. Cazuguel, J. You, A. Mayo, Q. Li, Y. Hatanaka, B. Cochener, C. Roux, F. Karray, M. García, H. Fujita, and M. D. Abràmoff, "Retinopathy Online Challenge: Automatic Detection of Microaneurysms in Digital Color Fundus Photographs," *IEEE Transactions on Medical Imaging*, vol. 29, no. 1, pp. 185-195, 2010.

[3] L. Zhang, Q. Li, J. You and D. Zhang, "A modified matched filter with double-sided thresholding for screening proliferative diabetic retinopathy," *IEEE Trans. on Information Technology in Biomedicine*, vol. 13, no. 4, pp. 528-534, 2009.

Working Journal Article

[4] Qin Li, Lei Zhang, Jane You, and David Zhang, "Vessel Extraction in Retinal Images using Multiscale Production of Matched Filter Responses," *to be submitted.*

[5] Qin Li, Lei Zhang, Jane You, and David Zhang, "Retinal Image Feature Extraction to Assist Diabetic Retinopathy Diagnosis," *to be submitted.*

Referred Conference Article

[6] J. You and Q. Li, "On hierarchical content-based image retrieval by dynamic indexing and guided search," *Proc. 8th IEEE Int. Conf. on Cognitive Informatics (ICCI'2009)*, Hong Kong, June 15-17, 2009, pp. 188-195.

[7] Q. Li, L. Zhang, J. You, D. Zhang and P. Bhattacharya, "Dark line detection with line width estimation," *Proc. of 2008 International Conference on Image Processing, (ICIP'2008)*, San Diego, USA, Oct. 12-15, 2008.

[8] Q. Li, J. You and G. Wang, "Robust line detection based on finite Randon transform and controlled morphological reconstruction," *Proc. of International Conference on Image Processing, Computer Vision and Pattern Recognition (IPCV'2008)*, Las Vegas, USA, July 14-17, 2008.

[9] Q. Li, Y.B. Zhang, J. You and P. Bhattacharya, "Screening prolifetive diabetic retionapathy through color retrieval images," *Proc. of 2007 International Conference on Image Processing, Computer Vision and Pattern Recognition (IPCV'07)*, Las Vegas, USA, June 25-28, 2007, pp. 574-578 (ISBN 1-60132-043-4).

[10] Q. Li, J. You and P. Bhattacharya, "Robust object extraction and change detection in retinal images for diabetic clinical studies," *Proc. 2007 IEEE Symposium on Computational Intelligence in Image and Signal Processing (CIISP'2007)*, Howaii, USA, April 1-5, 2007, pp. 357-362.

[11] Q. Li, J. You, L. Zhang and P. Bhattacharya, "A multiscale approach to retinal vessel segmentation with adaptive thresholding," *Proc. of 2006 IEEE*

Conference on Systems, Man and Cybernetics (IEEE SMC'2006), Taiwan, October 19-23, 2006, vol. 4, pp. 3521-3527.

[12] Q. Li, J. You, L. Zhang and P. Bhattacharya, "A new approach to automated retinal vessel segmentation using multiscale analysis," *Proc. of International Conference on Pattern Recognition 2006 (ICPR'2006)*, Hong Kong, August 20-24, 2006, vol. 4, pp. 77-80.

[13] Q. Li, J. You, L. Zhang and P. Bhattacharya, "Automated retinal vessel segmentation using Gabor filter and scale multiplication," *Proc. of 2006 International Conference on Image Processing, Computer Vision and Pattern Recognition (IPCV'06)*, Las Vegas, USA, June 26-29, 2006, vol. I, pp. 22-28 (ISBN 1-932415-93-9).

[14] Q. Li, J. You, L. Zhang and P. Bhattacharya, "Automated retinal vessel segmentation using multiscale analysis and adaptive thresholding," *Proc. of IEEE 2006 Southwest Symposium on Image Analysis and Interpretation (SSIAI'2006)*, Denver, Colorado, USA, March 26-28, 2006, pp. 139-143.

Other Publications

Book Chapter

[15] Y.B. Zhang, Q. Li, J. You and P. Bhattacharya, "Palm vein extraction and matching for personal authentication," *Computer Science Lecture Notes, LNCS4781*, Springer-Verlag GmbH, 2007 (Editted by G. Qiu, C. Leung, X.Y. Xue and R. Laurini, ISBN 978-3-540-76413-7, pp. 154-164.

[16] J. You, Q. Li, K.H. Cheung and P. Bhattacharya, "An integration of biometrics and feature selection for personal identification," *Computer Science lecture Notes, LNCS-3687*, edited by S. Singh et al., Springer-Verlag GmbH, pp. 226-235, 2005.

Referred Journal Article

[17] Q. Li, K.H. Cheung, J. You, R. Tong and A. Mak, "A robust automatic face recognition system for real-time personal identification," *Sensor Review*, vol. 26, no. 1, pp. 38-44, 2006.

[18] Q. Li, Z.M. Wang, W.M. Zuo and J. You, "An efficient image compression scheme based on PCA and wavelet analysis with application on distance learning data," *WSEAS Transactions on Signal Processing*, vol. 2, pp. 422-428, 2006.

Referred Conference Article

[19] J. You and Q. Li, "On hierarchical content-based image retrieval by dynamic indexing and guided search," *Proc. 8th IEEE Int. Conf. on Cognitive Informatics (ICCI'2009)*, Hong Kong, June 15-17, 2009, pp. 188-195.

[20] Q. Li, L. Zhang, J. You, D. Zhang and P. Bhattacharya, "Dark line detection with line width estimation," *Proc. of 2008 International Conference on Image Processing, (ICIP'2008)*, San Diego, USA, Oct. 12-15, 2008.

[21] Q. Li, J. You and G. Wang, "Robust line detection based on finite Randon transform and controlled morphological reconstruction," *Proc. of International Conference on Image Processing, Computer Vision and Pattern Recognition (IPCV'2008)*, Las Vegas, USA, July 14-17, 2008.

[22] Y.B. Zhang, Q. Li, J. You and P. Bhattacharya, "Palm vein extraction and matching for personal identification and liveness detection," *Proc. of 2007 International Conference on Image Processing, Computer Vision and Pattern Recognition (IPCV'07)*, Las Vegas, USA, June 25-28, 2007, pp. 579-583 (ISBN 1-60132-043-4).

[23] Q. Li, J. You, R. Tong and A.Mak, "Robust human motion detection via fuzzy set based image understanding," *Proc. of SPIE Electronic Imaging 2006*, San Jose, USA, Jan. 15-19, 2006.

[24] Q. Li, J. You and P. Bhattacharya, "A new approach to human movement monitoring by monitoring robust motion," *Proc. of the 2nd IEEE International Conference on Machine Intelligence (ACIDCA-ICMI 2005)* Tozeur, Tunisia, November, 2005.

[25] Q. Li, J. You and P. Bhattacharya, "A PCA-wavelet based coding scheme for distance learning," *Proc. of IASTED International Conference on Communications, Internet and Information Technology (CIIT 2005)*, Cambridge, USA, Oct. 31 - Nov. 2, 2005, pp. 214-219.

[26] Q. Li, J. You and P. Bhattacharya, "A new approach to robust human motion detection," *Proc. of IASTED International Conference on Intelligent Systems*

and Control (ISC 2005), Cambridge, USA, Oct. 31 - Nov. 2, 2005, pp. 398-403.

[27] K.H. Cheung, J. You, Q. Li and P. Bhattacharya, Appearance-based face recognition using aggregated 2D Gabor features," *Proc. of IEEE International Conference on Systems, Man and Cybernetics (IEEE SMC'2005)*, vol. 2, Hawaii, USA, Oct. 10-12, 2005, pp. 1686-1691.

[28] Q. Li, J. You, R. Tong and A. Mak, "A robust motion detection system for real-time human movement monitoring," *Proc. of IASTED International Conference on Telehealth (Telehealth'2005)*, Banff, Canada, July 19-21, 2005.

[29] K.H. Cheung, J. You, Q. Li and P. Bhattacharya, "On aggregated 2D Gabor features for appearance-based face recognition," *Proc. of 2005 International Conference on Image Science, Systems and Technology (CISST'2005)*, Las Vegas, USA, June 27-30, 2005, pp. 33-39.

[30] K.H. Cheung, J. You, Q. Li and P. Bhattacharya, "Appearance-based face recognition using aggregated 2D Gabor features," *Proc. of Workshop on Pattern Recognition in Information Systems (PRIS'2005)*, Miami Beach, Florida, USA, May 24-25, 2005, pp. 81-93.

Acknowledgements

I would like to express my sincere gratitude to Dr. Jane Jia YOU, my chief supervisor, for her supervision and kind help over the period of my study. I would like to thank Professor David Da-Peng ZHANG, the founder and director of the Biometrics Research Centre, for granting me a great research environment.

I would like to express my greatest gratitude to, the Chairman of the Board of Examiners, to, the External Examiners, for their time and involvement in my PhD examination.

I would like to show my utmost gratefulness to Dr. Lei ZHANG for giving me so many creative ideas for my research work.

I would like to thank the personnel of Research Office and Department of Computing for providing me various kinds of help throughout the period of my study. I would also like to thank my friends King-Hong CHEUNG, Adams KONG, Wang-Meng ZUO, Dennis GUO, Jerry ZHAO, Laura LIU, for supporting me and for so many helpful discussions throughout the period of my study.

Finally I would like to thank my parents for their love and support throughout the past years, in particular, my mother who left for another world at the final stage of write-up this work. I would like to dedicate this thesis to her.

Table of contents

List of figures

List of tables

Chapter 1 Introduction

The retina is a light-sensitive tissue at the back of the eye. When light enters the eye, the retina changes the light into nerve signals. The retina then sends these signals to the brain. Images of the ocular fundus, also known as retinal images, can tell us about retinal, ophthalmic, and even systemic diseases such as diabetes, hypertension, and arteriosclerosis. All such retinal or systemic diseases which manifest by a sign in the retina can be referred to as retinopathies.

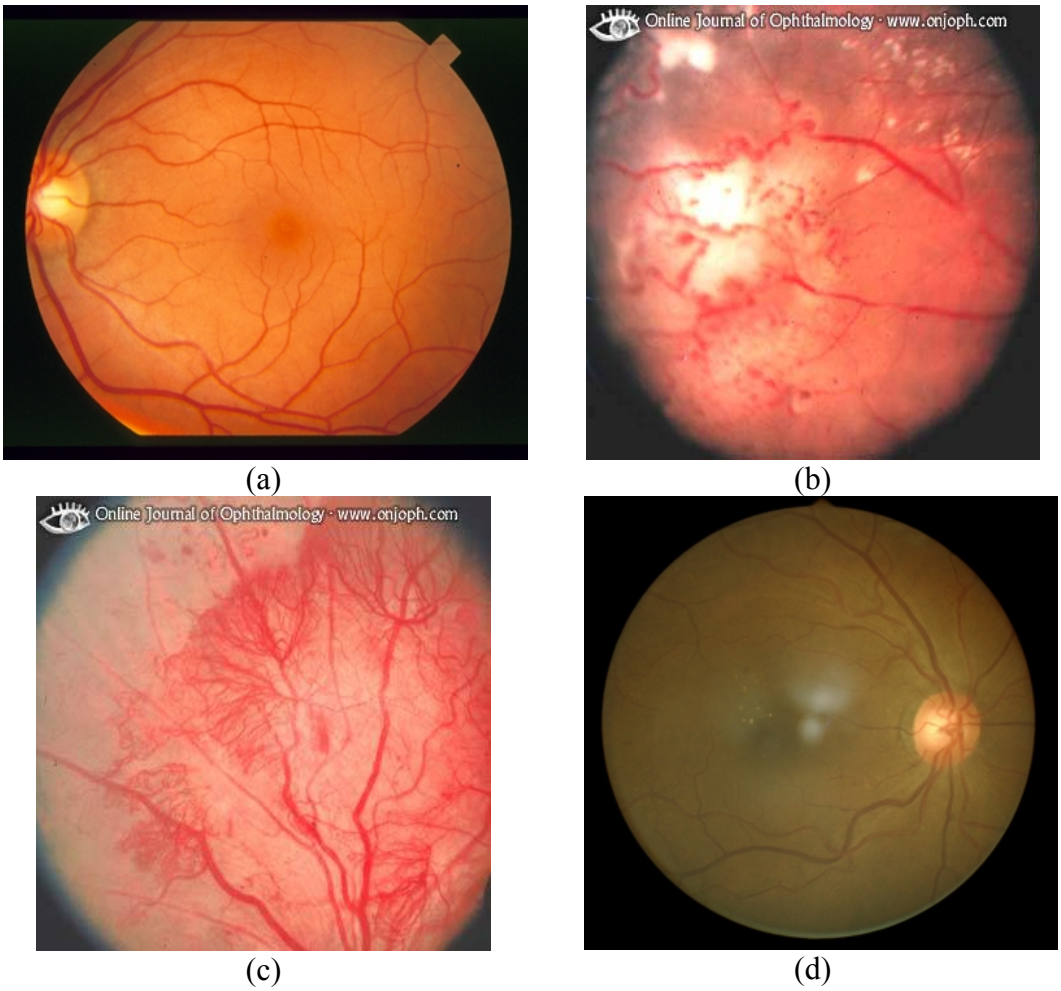

(a) (b)

(c) (d)

Figure 1.1 Retinopathies [1]. (a) Healthy retina, (b) Coat's, (c) Diabetes and (d) Hypertension

Figure 1.1 shows images of healthy retina and pathological retina (images downloaded from the website of [1] [2]). Figure 1.1(a) shows a healthy retina. Figure 1.1(b) shows a retina with Coat's disease. Figure 1.1(c) and (d) show two images with retinopathies caused respectively by diabetes and hypertension, two very common systemic diseases.

The colour retinal images captured using digital fundus cameras are widely used in clinics because they are a non-intrusive way to screen for retinopathies. A fully automated segmentation of colour retinal images can greatly help in the management of certain diseases, especially diseases such as diabetic retinopathy and hypertensive retinopathy which require the screening of large populations. Automated segmentation of colour retinal images can help eye-care specialists screen larger populations. The first project for automated fundus diagnosis, STARE (STructured Analysis of the REtina), was initiated in 1975 by Dr. Michael Goldbaum and his research team in the USA [2] [3]. They built a publicly available database STARE and did a lot of important work in fundus diagnosis. In 1989, they designed a "matched filter" for vessel segmentation [3] and it remains today the most reliable retinal vessel detector. In 1996, they published a paper on ICIP [4], which covers most of fundus diagnosis research, including image segmentation, object classification, and diagnosis using classified features. They provided the following framework for fundus diagnosis:

Step 1: Extract objects (main regions of retina such as vessel, optic disc, and fovea; lesions caused by certain diseases) in retina by image segmentation;

Step 2: Find all manifestations (abnormalities in the retina such as vein dilation, cherry red spots and cotton wool spots) in retina through object classification;

Step 3: Make diagnoses using manifestations.

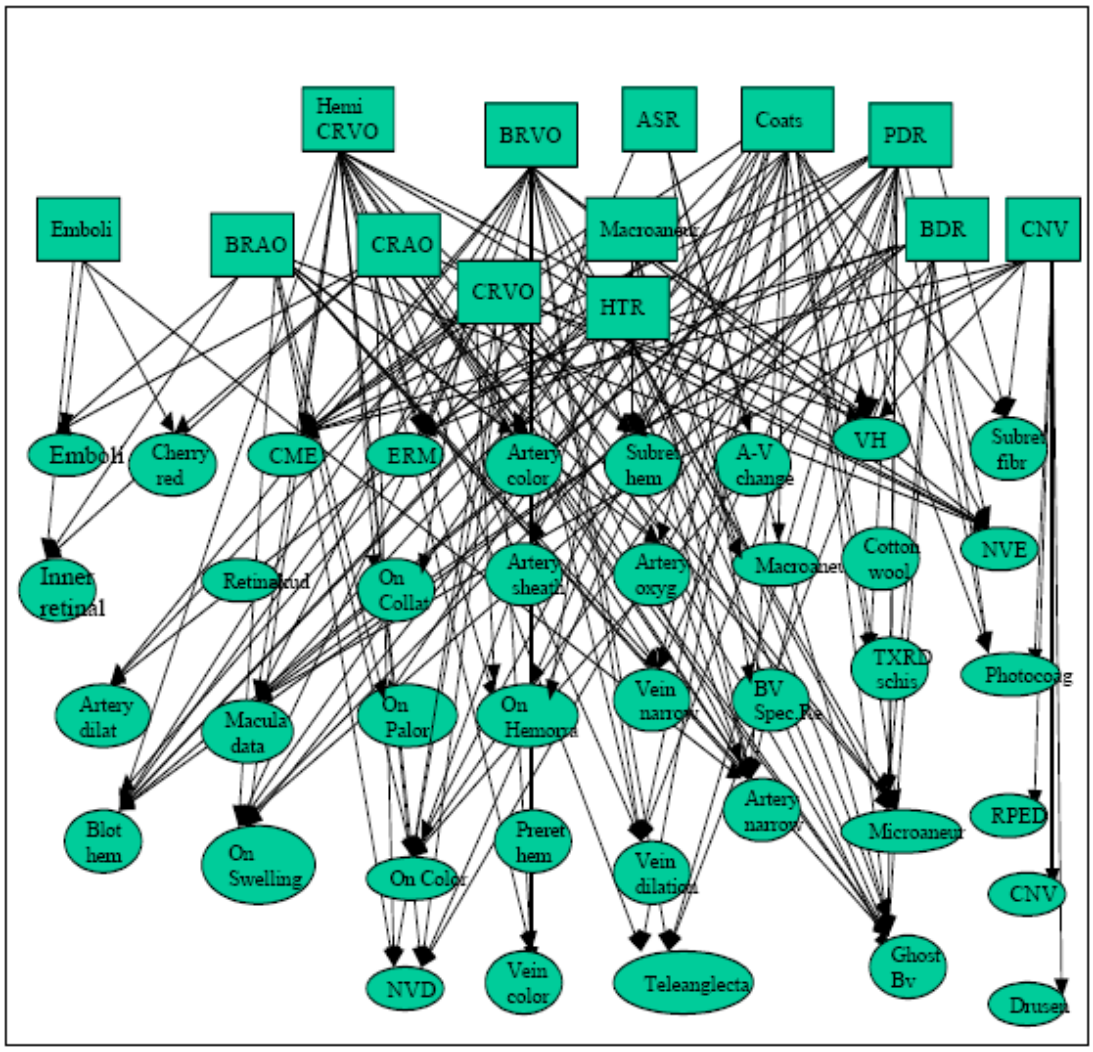

Figure 1.2 Influence diagram for fundus diagnosis proposed by R. Pai et al. [5][6].

They also published work on diagnosis using evidential reasoning [5][6], which built a theoretical foundation for automated fundus diagnosis. Figure 1.2 [5][6] shows an influence diagram that they proposed where the ovals represent the manifestations and the squares represent the diagnoses. The human retina can manifest hundreds of diseases and their system can make 13 diagnoses based on 39 manifestations. While this system is less detailed and complex than a human expert diagnoses, as we can see in the diagram, automated fundus diagnosis even in restricted form is still very complex.

The Eyecheck fundus diagnosis project EyeCheck was launched in Europe by Dr. Michael D. Abràmoff and his team [7][8]. They provided another public available

database, DRIVE, and did important work in areas such as vessel segmentation and red lesion segmentation [9][10].

Most recent research in fundus diagnosis has focused on retinal image segmentation [3][9][16]--[53][65]--[84][86]--[113] because it is the first step in fundus diagnosis and segmentation alone can identify many patients with retinopathies. The meaningful objects to be segmented include the main regions of the retina and the lesions caused by certain diseases. The appearance of certain lesions can be the sign of certain retinal diseases and systemic diseases. For example, a bright lesion is a sign of Diabetic Retinopathy (DR) [11]--[15]. The main regions of the retina are the optic disc, fovea, and blood vessels. The identifications of these regions assists in the analysis of diseases that affect these regions preferentially, such as glaucoma, which can dilate the optic disc, and proliferative diabetic retinopathy, which can cause new vessel growth [11]--[15]. A further advantage is that locating these regions assists in locating other lesions.

Diagnosis relies on the outward appearance of blood vessels. Automated segmentation of blood vessels in retinal images can help eye-care specialists screen larger populations for vessel abnormalities caused by retinal diseases or systemic diseases. The importance and usefulness of using retinal vessels to help screen Diabetic Retinopathy (DR) has been reported in [9][16] and the diagnosis of Retinopathy of Prematurity (ROP) by retinal vessel information has been reported in [17][18]. A lot of vessel segmentation algorithms have been proposed [3][9]--[40] but the results have not been very satisfactory.

While there are thousands of retinopathies that can affect the human eye, for a number of reasons, most researchers are working on the diagnosis of Diabetic Retinopathy (DR): because DR is a serious disease that causes blindness and even a

sign of death [11]--[15]; because it affects many people [11]--[15] and because it can be detected early and successfully treated [11]-[15]. The objects useful for DR diagnosis include retinal lesions such as red lesions (intraretinal hemorrhages, microaneurysms), bright lesions (hard exudates and cottonwool spots) and retinal main regions such as vessels, optic disc, and fovea [11]-[15]. It is difficult to build a system to segment all of these objects because the contents of retinal images are very complex. The major difficulty comes from the fact that retinal objects-pathological and physical- mutually affect each other, producing false positives for one feature or another.

In this thesis, we describe the major difficulties in retinal vessel segmentation and propose two novel vessel segmentation methods. Our attention is largely directed to the use of retinal image segmentation for screening for DR in large populations. We propose a robust and efficient retinal image segmentation system for segmenting the main regions of the retina and the major lesions caused by DR.

The rest of this thesis is organized as follows. Chapter 2 provides the background and a review of the color retinal image segmentation including the main regions of the retina and the segmentation of DR lesions. Chapter 3 describes the design of our own two novel retinal vessel algorithms. Chapter 4 proposes a robust and efficient retinal image segmentation system for screening for DR. Finally, Chapter 5 offers our conclusion, contributions, and some future research directions.

Chapter 2 Background and Literature Review

2.1 Medical Background

Generally, there are two groups of objects to be segmented for fundus diagnosis: main regions of the retina (optic disc, fovea, and blood vessels) and the lesions caused by certain diseases. The identifications of the main regions assists in the analysis of diseases that affect these regions preferentially, such as glaucoma, which can dilate the optic disc, hypertension, which can cause vessel tortuosity, and proliferative diabetic retinopathy, which can cause new vessel growth [11]--[15]. A further advantage is that locating these regions assists in locating other lesions. The appearance of certain lesions can be the sign of certain retinal and systemic diseases. In this chapter, we review the segmentation of images showing signs of Diabetic Retinopathy (DR), a potentially blinding complication of diabetes.

The objects useful for DR diagnosis include retinal lesions such as red lesions (intraretinal hemorrhages, microaneurysms), bright lesions (hard exudates and cotton-wool spots) and retinal main regions such as vessels, optic disc, and fovea [11]--[15]. The identification of the main regions can help to analysis DR that preferentially affects these regions. For example, proliferative diabetic retinopathy (PDR) can cause new vessel growth [11]--[15]. A further benefit of locating these regions is that the consequences of certain manifestations are worse when they are closer to some regions. For example, lesions in the fovea or new vessel growth around the optic disc can cause blindness. Dr. Michael Goldbaum and his team proposed a retinal coordinate system to locate all manifestations [4]. Figure 2.1 illustrates those main regions. Figure 2.1(a) shows the optic disc and fovea (green circles). The bright object in which many blood vessels converge is the optic disc,

the connection between the brain and the eye. The dark area in the middle of the image is the fovea, which is in charge of making an image from the incident light. Figure 2.1(b) shows the manually segmented retinal blood vessels which are in charge of the blood and oxygen supply to the retina.

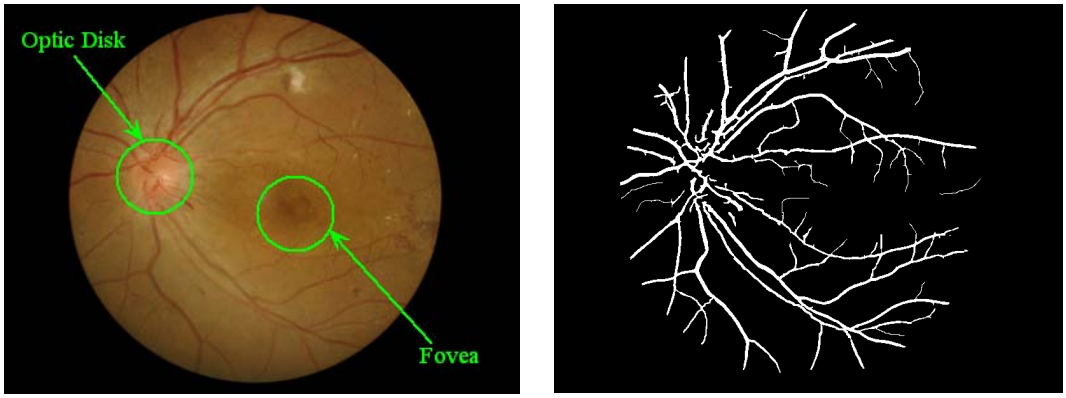

(a) (b)

Figure 2.1 Main regions of retina. (a) Optic Disc and Fovea, (b) Blood vessels.

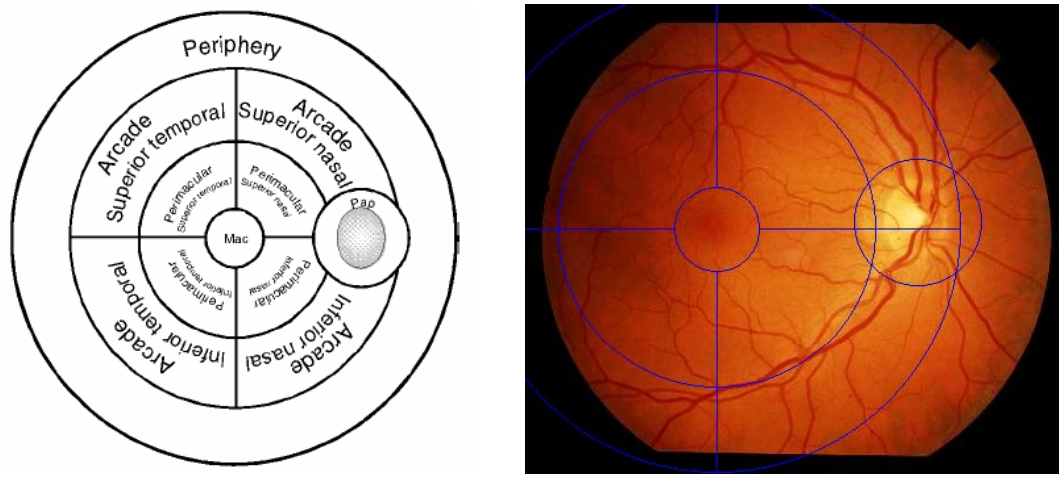

Figure 2.2 Retinal coordinates system [4].

Figure 2.2 shows this coordinate system, which is based on the optic disc and fovea.

In the following we briefly introduce DR. DR can be roughly classified according to severity into four stages [11]--[15].

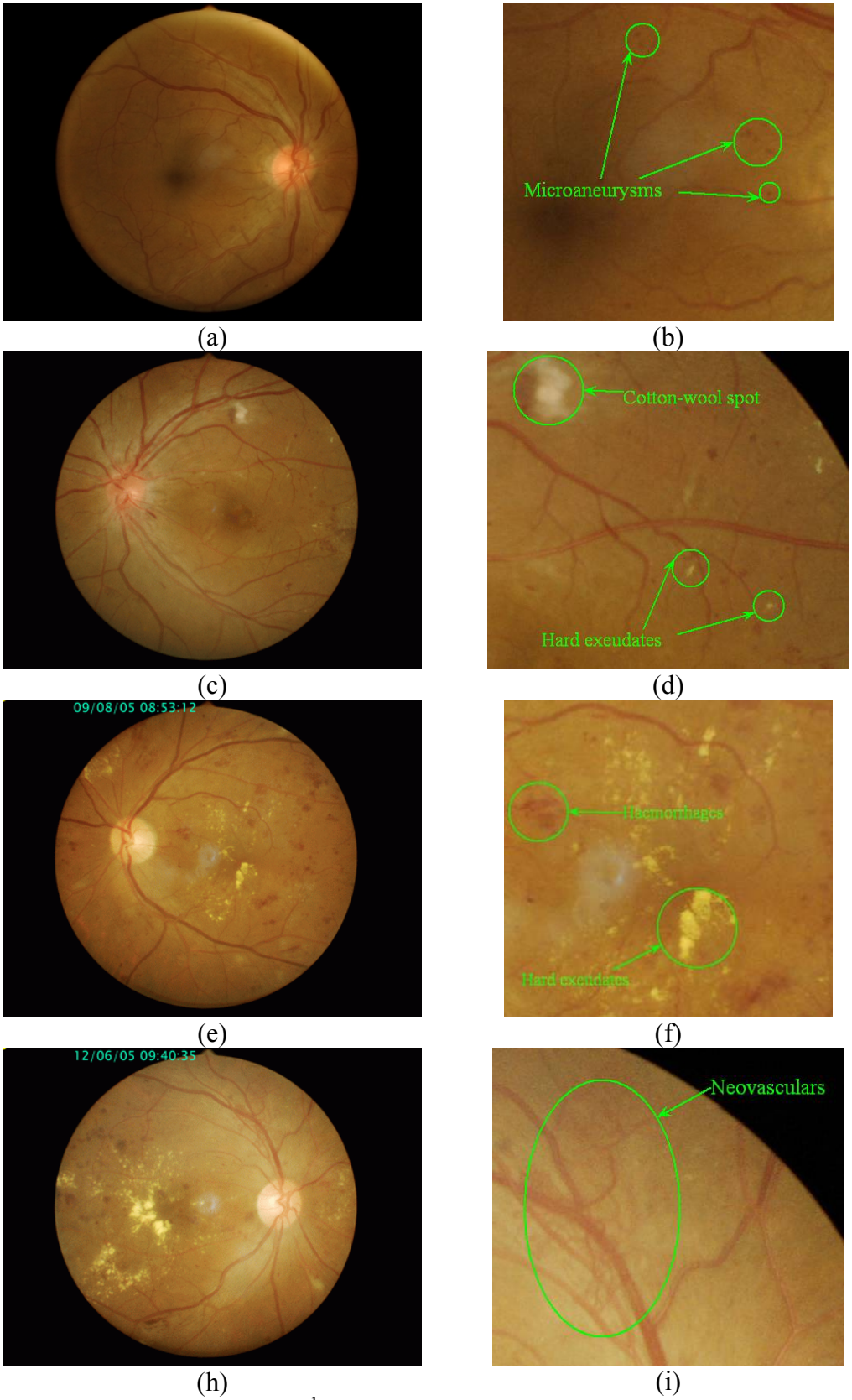

(a) (b) (c) (d) (e) (f) (h) (i)

Figure 2.3 Four stages of DR[1].

[1] The images were collected from the patients in the Ophthalmologic Department, the First Affiliated Hospital of Henan Medical College, Henan Province, China.

Stage 1: Mild non-Proliferative Diabetic Retinopathy (NPDR). In this stage, only microaneurysms or very small intraretinal hemorrhages appear. Figures 2.3(a) & (b) shows an example.

Stage 2: Moderate NPDR. In this stage, bright lesions appear beside red lesions. But the damaged area of the retina is small and there is no severe damage to the fovea and optic disc. Figures 2.3(c) & (d) show an example.

Stage 3: Severe NPDR. In this stage, more retinal areas have been damaged and severe damage may appear on the fovea and optic disc. Figures 2.3(e) & (f) show an example.

Stage 4: Proliferative Diabetic Retinopathy (PDR). In this stage, new vessels (neovasculars) grow from the damaged vessels. This is a severe stage of DR. The Neovasculars bleed easily and cause blindness. Neovasculars are predictive of death within 5-10 years. Figures 2.3(h) & (i) show an example.

DR is normally visible in the retina. That makes the automated diagnosis of DR through image segmentation possible. The following briefly introduces the state of the art of automated retinal image segmentation.

2.2 Segmentation of Main Regions

2.2.1 Retinal Vessel Segmentation

Vessel segmentation is a specific line detection problem and hence many vessel extraction algorithms originated from the line detection techniques [54]--[60]. Generally speaking, there are two steps in vessel segmentation: vessel enhancement and vessel classification (some methods may go directly to the second step).

Step1) Vessel enhancement In this step, vessels are enhanced and noise is suppressed. Vessel enhancement is usually implemented locally by using a window centered at the pixel to be enhanced. This class of techniques

originated from the classical image processing problem: finding parallel edges and ridges in an image [54]--[60]. Line detectors include high-pass filters [55][56], band-pass filters [57][59][60], and mathematical morphology filters [54]. There are two basic line models Figure 2.4, the bar-shaped model that is used to find parallel edges and the Gaussian-shaped model used to find ridges [59].

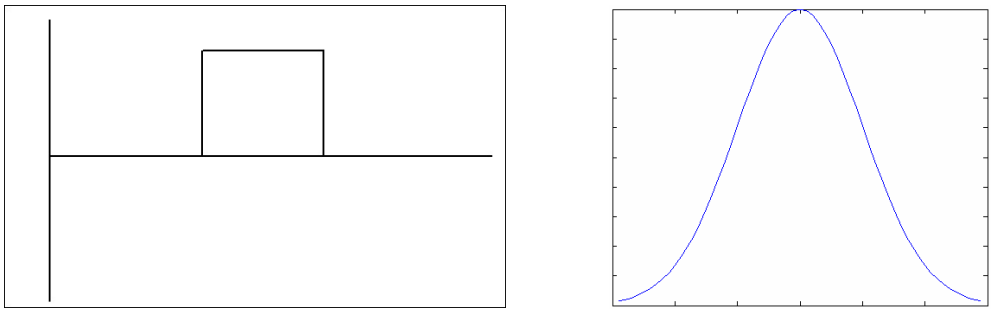

(a) (b)

Figure 2.4 Line models: (a) bar-shaped; (b) Gaussian-shaped.

The bar-shaped line is defined by Equation 2.1 where *h* is the height of the line and *w* is the width of the line [59].

$$f_b(x) = \begin{cases} h, & |x| \le w \\ 0, & |x| > w \end{cases} \tag{2.1}$$

The Gaussian-shaped line is defined by Equation 2.2 where σ is the standard derivation of Gaussian [58].

$$f_\sigma(x) = e^{-\frac{x^2}{2\sigma^2}} \tag{2.2}$$

In [54], Koller *et al.* found the parallel edges of the bar-shaped line using a pair of high-pass filters defined in Equation 2.3, where σ is the standard derivation of Gaussian and *s* is the shift of the filter. As shown in Figure 2.5, in order to detect a line of width *w*, the best enhancement is achieved at $\sigma = \frac{w}{2}$ [56].

$$\begin{cases} G_\sigma(x) = e^{-\frac{x^2}{2\sigma^2}} \\ E_l(x) = -G_\sigma'(x+\sigma) \quad and \quad E_r(x) = G_\sigma'(x-\sigma) \end{cases} \tag{2.3}$$

In [59], Steger detected the bar-shaped line using the second derivative of Gaussian, which is a band-pass filter and defined by Equation 2.4. As shown in Figure 2.6, in order to detect lines of arbitrary widths, this filter has to be iterated in scale space. The constraint $\sigma \geq \frac{2w}{\sqrt{3}}$ has to be satisfied to produce a maximum response at the center of the line of width *w*.

$$G_\sigma''(x) = \frac{x^2 - \sigma^2}{\sqrt{2\pi}\sigma^5} e^{-\frac{x^2}{2\sigma^2}} \tag{2.4}$$

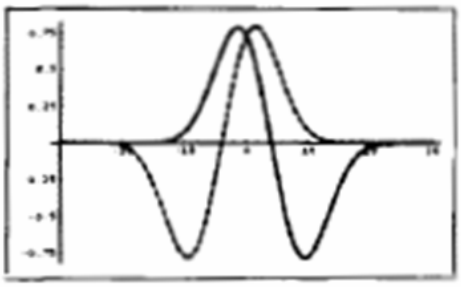

Figure 2.5 A pair of high-pass filters.

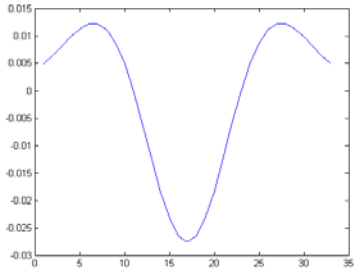

Figure 2.6 The second derivative of Gaussian.

The 2-D Gabor filter [62] is a band-pass filter being widely used in image processing because of its tunable orientations, radial frequency bandwidths and center frequencies and optimal joint resolution in space and spatial frequency.

In [60], Deemer and Buf proposed an edge and line detection scheme using Gabor filters. In most cases, only the real part of the Gabor filter is used for convolution with the modulation axis parallel to the envelope axis, which is expressed by Equations 2.5 - 2.7 where ϕ is the filter direction, σ is the standard deviation of Gaussian envelope, and *f* is the frequency of cosine wave. For convenience, the modulating Gaussians of filters are set to have the same direction as the complex sine grating so that there is only one direction parameter. Liu *et al.* [61] has proved that to produce a single peak response on the center of a line of width *w* using Gabor filters rotated in *n* directions the parameters can be set as Equations 2.8 - 2.10 where $\alpha \in [1,1.5]$, $\beta \in [0.5,1]$, $\lambda = \sqrt{2\ln 2/\pi}$, and $\kappa = 0.85$. Figure 2.7 shows an example of 1-D Gabor filters of the same σ but different *f*. We can see that the response of a line of a particular width is highly dependent on the parameter f, and the ability to denoising is highly dependent on the parameter σ.

$$g_{\phi}(x,y) = \exp\left\{-\pi\left(\frac{x'^2}{\sigma_x{}^2} + \frac{y'^2}{\sigma_y{}^2}\right)\right\}\cos\left(2\pi f x'\right) \tag{2.5}$$

$$x' = x\cos\phi + y\sin\phi \tag{2.6}$$

$$y' = -x\sin\phi + y\cos\phi \tag{2.7}$$

$$f = \beta / w \tag{2.8}$$

$$\sigma_x = \frac{n\lambda w}{\alpha\beta\pi} \tag{2.9}$$

$$\sigma_y = \kappa\sigma_x \tag{2.10}$$

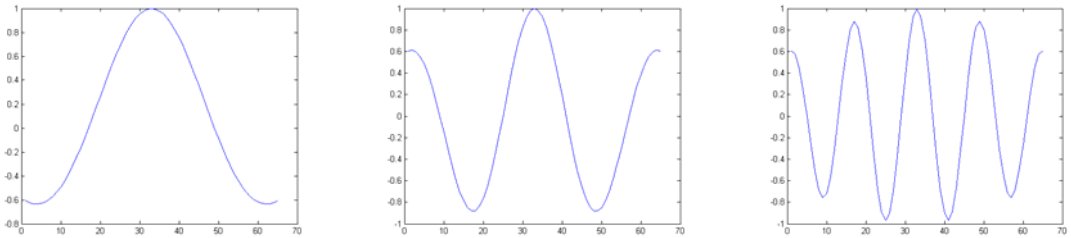

(a) Cosine period = 64 (b) Cosine period = 32 (c) Cosine period = 16

Figure 2.7 A series of Gabor filters of Gaussian window width = 64**.**

If it is to detect lines of arbitrary widths, this filter has to be iterated in scale space. Figure 2.8 (a) shows a family of 2-D Gabor filters along scale space. Figure 2.8 (b) illustrates the spatial frequency responses.

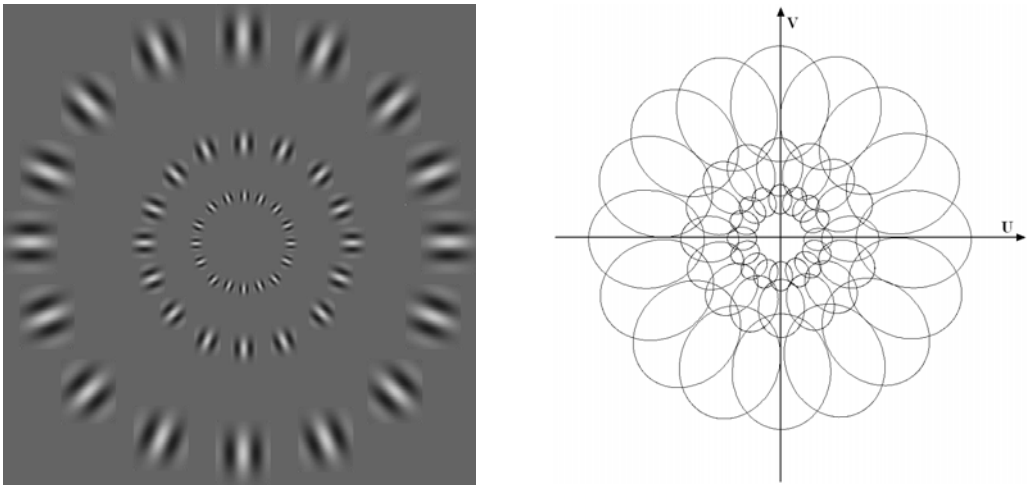

(a) (b)

Figure 2.8 A family of the Gabor filters with the spatial frequency responses.

In spite of those time-frequency analysis, a morphological Top-hat operation [54] is also an effective way to find lines in images. The Top-hat operation is used to separate foreground from background. Mathematically, it can be defined as Equation 2.11 or 2.12, where $\bullet$ represents morphological closing, $\circ$ represents morphological opening, S_c represents the structural elements used for closing, and S_o represents the structural elements used for opening.

$$TopHat(I) = I \bullet S_c - I \tag{2.11}$$

$$TopHat(I) = I - I \circ S_o \tag{2.12}$$

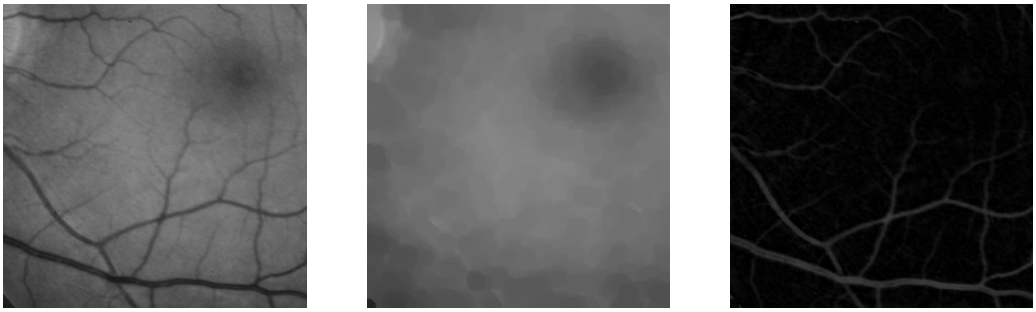

(a) (b) (c)

Figure 2.9. Top-hat operation. (a) Original image; (b) Background estimated by closing; (c) Foreground produced by calculating the difference between original image and background.

As shown in Figure 2.9, the background is estimated by a morphological closing operation, and then the foreground is generated by calculating the difference between the original image and the background.

In [27], Can *et al.* enhanced the vessels by using a pair of high-pass filters for the left and right edges of vessels. The Gabor filters were reported to enhance vessels in [16][22]. In [3], the use of a matched filter was proposed as a way of detecting retinal vessels. The matched filter is an effective technique for enhancing vessels by exploiting the prior information that the cross-section of a retinal vessel is Gaussian-shaped. The matched filter is defined by Equation 2.13 where σ represents the scale of the filter; $m = -\left(\int_{-3\sigma}^{3\sigma} \exp\left(-x^2/\sigma^2\right)dx\right)/6\sigma$ is used to normalize the mean value of the filter to 0, which is actually a band-pass filter in Gaussian shape.

$$g(x,y) = -\exp\left(-x^2/\sigma^2\right) - m, \quad \text{for } |x| \le 3\sigma, \quad |y| \le L/2 \tag{2.13}$$

The use of mathematical morphology filters to enhance vessels was reported in [23][36]. In [23], Mendonça proposed a modified Top-hat operation which is defined by Equation 2.14, where the closing operation is used to smooth the

original image so that the small background intensity fluctuations can be eliminated and the minimum operation is used to eliminate the small intensity fluctuations in the difference image.

$$TopHat(I) = I - \min\left(\left(I \bullet S_c\right) \circ S_o; I\right) \tag{2.14}$$

The Hessian based methods were reported in [33][34][37]. In [33][34], Martinez *et al*. proposed a vessel segmentation method based on gradient magnitude and principle curvature. The gradient magnitude is defined by Equation 2.15 where ∂ represents partial derivatives. The principle curvature is derived from Hessian matrix which is defined by Equation 2.16. The partial derivatives of an image can be estimated by convolving the image with derivatives of a Gaussian kernel. Thus, it can be regarded as a combination of high-pass filter and band-pass filter.

$$\left|\nabla I\right| = \sqrt{\left(\partial_x I\right)^2 + \left(\partial_y I\right)^2} \tag{2.15}$$

$$H = \begin{pmatrix} \partial_{xx} I & \partial_{xy} I \\ \partial_{yx} I & \partial_{yx} I \end{pmatrix} \tag{2.16}$$

The combination of filters is also reported in other works. In [23], the images are processed using high-pass filters and morphological filters. In [18], the vessels were enhanced through combing morphological filter and the second order derivative operator (band-pass).

Step 2 Vessel classification. After vessel enhancement, the pixels are classified as vessel pixels and non-vessel pixels. Methods for classification can be summarized as supervised methods [9][16][19][50] and un-supervised methods. Supervised methods need a manually produced training set. The use of Neural networks is reported in [19][50]. In [8], A KNN-classifier is proposed by Staal

at al. [9], which is defined by Equation 2.17, where $p(vessel)$ is the posteriori probability to be a vessel pixel, *k* means *k* neighbors, and *n* of *k* neighbors are labeled as vessels.

$$p(vessel) = \frac{n}{k} \tag{2.17}$$

In [16], Soares applied a GMM classifier on the images enhanced by Gabor filter. This GMM classifier is actually a Bayesian classifier in which each class-conditional probability density function is described as a linear combination of Gaussian functions [63][64]. As a two-class classification problem, this Bayesian classifier is defined as Equation 2.18 [16] where $p(v|C_i)$ is the class-conditional probability density function and $P(C_i)$ is the prior probability of class C_i. The class-conditional probability density function is described in Equation 2.19 where k_i is the number of Gaussians modeling $p(v|C_i)$ and each $p(v|j,C_i)$ is a Gaussian distribution of weight P_{ij}.

$$\begin{aligned} &Decide\, C_1 \quad if \quad p(v|C_1)P(C_1) > p(v|C_2)P(C_2) \\ &otherwise \quad decide \quad C_2. \end{aligned} \tag{2.18}$$

$$p(v|C_i) = \sum_{j=1}^{k_i} p(v|j,C_i)P_{ij} \tag{2.19}$$

Unsupervised methods are much more popular in vessel segmentation. The easiest way for vessel segmentation is to find an optimal threshold to classify the pixels according to their intensities. The classification results can be improved at a price of more computation. A threshold probing of the matched filter was proposed in [20] to improve the accuracy by analyzing the region-based attributes of the vessel network structure. In [24], a

multi-threshold probing algorithm was applied directly to the original retinal images for classification. The snakes and tracking based methods, which utilize not only the intensity information but also the geometrical and topological information, were reported in [18]-[31] . In [26], a vessel tracking algorithm based on fuzzy clustering was proposed. In [27], the vessels were segmented through tracking parallel edges. In [31], an intensity ridge traversal based method was proposed with the optimization of some major elements in ridge tracking (initialization, noise, singularities, and scale). A region growing scheme was proposed in [33][34] with the analysis of both spectral information (gradient and curvature) and spatial information.

2.2.2 Optic Disc Segmentation

All vessels converge at the optic disc which connects the retina and the brain. In a normal retina, the optic disc is the brightest region. Current optic disc detection methods can be divided to intensity-based [50][65][66], template-based [67]--[73], shape-based [75][76], and vessel-based [77]--[84].

The optic disc normally is the brightest region in the retina. Thus, the intensity information can be used to detect the optic disc. In [50][65], Sinthanayothin *et al.* detected the optic disc by locating the region with the highest average intensity variation because normally many dark blood vessels converge at the bright optic disc. In [66], Walter and Klein detected the optic disc as the largest and brightest object in the retina by assuming that all bright lesions are much smaller than the size of the optic disc.

Template matching is a classical way to find the target object in an image [54]. In [67][68][69], Li and Chutatape employed PCA [63][64] to extract features of the optic disc. They first manually cut sub-images around the optic disc region from the

training images [67][68][69] and then used PCA to obtain the "eigen-discs" that describing "disc-space". Figure 2.10 shows some examples of eigen-discs. Using a template moving throughout a retinal image, the candidate sub-images were projected onto the disc-space and the candidate sub-image with the smallest reconstruction error was regarded as the optic disc [67][68][69]. In [71][72][73], Osareh *et al*. proposed to locate the optic disc by using a template matching approach based on a normalized correlation coefficient. The images were normalized at first, and then the optic disc region from 25 normalized images was averaged to produce a template. Finally they used the normalized correlation coefficient to find the most perfect match between the template and all the candidate sub-images. In [70], Lalonde *et al.* proposed a Hausdorff-based template matching. First, a multiresolution processing was employed through pyramidal decomposition. Small bright lesions were eliminated at lower resolutions, which speeds searching of the optic disc because it reduces the number of false candidates. A confidence value was calculated for all the candidate regions, then the Canny edge detector [55] was applied on the green channel image regions corresponding to the candidate regions to construct a binary edge map. Finally, the Hausdorff distance was used to match the edge map regions to a circular template of various different radii.

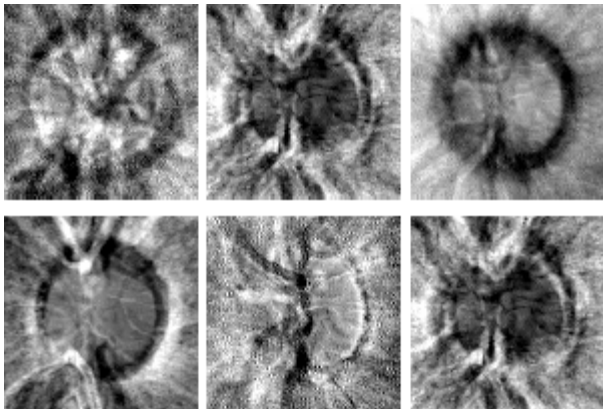

Figure 2.10. Eigen-discs.

The fact that the optic disc appears as a large circular shape in the retina makes it possible to detect it using the Hough transform, which is capable of detecting geometric shapes in an image [75][76]. In [76], Abdel-Ghafar *et al*. detected the optic disc using the circular hough transform (CHT). First the retinal vessels were suppressed using a morphological closing operator. Then the Sobel operator [54] was used to extract the edges in the image. Finally the CHT was applied to the edge map, and the the optic disc was identified as the largest circle.

Since all vessels converge at the optic disc, it is also possible to identify the optic disc by vasculature features [77]--[84]. In [77][78], Hoover and Goldbaum proposed a fuzzy convergence technique for identifying the optic disc as the convergence point of the retinal vasculature. First, the retinal vessels were segmented using the matched filter [3] then each vessel branch was modeled using a fuzzy segment to form a convergence image. The intensity of each pixel on the convergence image is equal to how much of the fuzzy segment crossed that pixel. The strongest convergence point was regarded as the retinal vasculature convergence. Figure 2.11 shows an example of this fuzzy convergence [77][78]. In [4][80], the optic disc was located using three optic disc features: (1) the blood vessels convergence at the optic disc; (2) the optic disc appears as a bright disc; (3) the large vessels entering the OD from above and below. In [81][82][83], the optic disc was located using vasculature-related features: (1) probability distributions describing the luminance across the retina; (2) the density of the vasculature; (3) average thickness of the vasculature; (4) average orientation of the vasculature. In [81], Tobin *et al.* located the optic disc using a Bayesian classifier [64] trained using fifty images. In [82][83], Abràmoff and Niemeijer used the KNN regression [64] trained using hundreds of images. In [79][84], the optic disc was located based on the fact that the retinal vasculature

originates from the optic disc following a similar directional pattern in all retinal images.

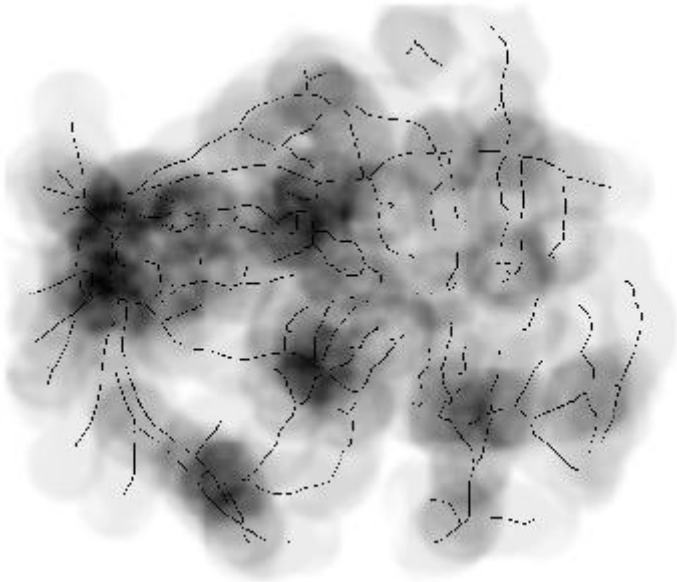

Figure 2.11. Fuzzy convergence [77][78]**.**

Figure 2.12 illustrates this directional pattern [84]. In [79], Foracchia *et al.* located the optic disc using a geometrical model of the retinal vessels structure. First, the main vessels originating from the optic disc were geometrically modeled using two parabolas, enabling the center of the optic disc to be located as the common vertex of the two parabolas. In [84], Youssif *et al.* located the optic disc using a proposed vessel direction matched filter. First, the retinal vessels were segmented using a 2-D Gaussian matched filter. Then the same segmentation algorithm was used to obtain a map of the directions of the vessels of the segmented retinal vessels. The segmented vessels were then thinned to represent the candidate centers of the optic discs. They then measured the difference between the proposed vessel direction matched filter and the directions of vessels at the surrounding area of each of the candidate center of the optic disc. The center of the optic disc center is the candidate with the minimum difference.

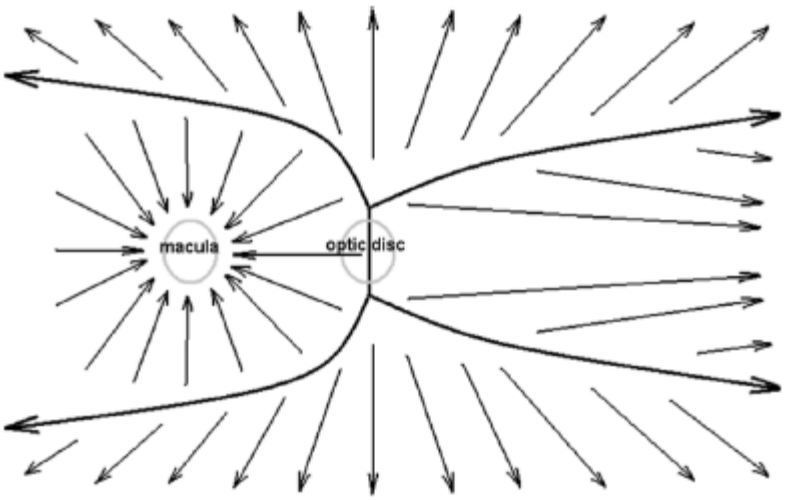

Figure 2.12. Vessel's direction pattern [84].

2.2.3 Fovea Segmentation

Fovea segmentations are relatively less studied. There are two groups of fovea segmentation/detection methods: (1) template-based [50][65]; (2) vasculature-based [68][69][83].

The fovea appears as a large dark disc and is centered at the image approximately 2.5 times the optic disc diameter from the optic disc. This motivated Sinthanayothin [50][65] *et al.* to detect fovea using a template matching approach. The template was defined as a 2D Gaussian to approximate a typical fovea. Equation 2.20 described this template. The location with the maximum correlation coefficient between the template and the image was chosen as the location of the fovea, restricted to the condition that it should be an acceptable distance from the optic disc. They reported accuracy 80.4% on 100 images.

$$g(i,j) = 128\left[1 - \exp\left(\frac{-\left(i^2 + j^2\right)}{2\sigma^2}\right)\right] \tag{2.20}$$

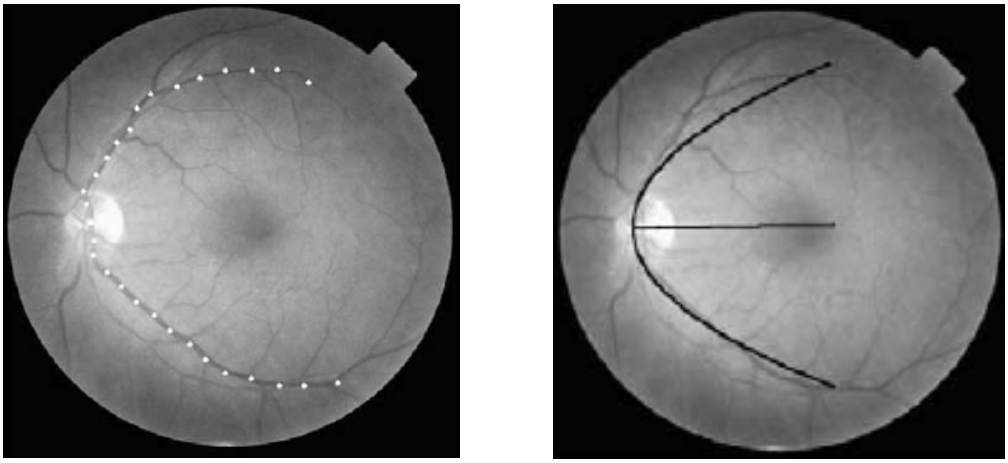

Figure 2.13. ASM used for fovea detection [68][69]. (a) An example of 30 landmark points; (b) An example of parabola fitting.

The fovea are supposed to be in the middle of the two large vessel trunks emanating from the optic disc and it can be detected using vasculature-related features [68][69][83]. In [68][69], Li and Chutatape extracted the main courses of the blood vessels using a modified Active Shape Model. ASM [85] consists of building a point distribution model (PDM) from a training set and an iterative searching procedure to locate instances of shapes in a new image. The main courses of blood vessels were described using 30 landmark points. They used eight landmark sets to train the PDM then the fovea was located by fitting the main courses on a parabola. Figure 2.13(a) shows an example of landmark points; Figure 2.13 (b) shows an example of parabola fitting. In [83], Niemeijer and Abràmoff proposed a PDM to detect the optic disc, vessel arch, and the fovea together. This PDM was defined by 16 points as illustrated in Figure 2.14. This PDM was derived from a set of 500 training cases.

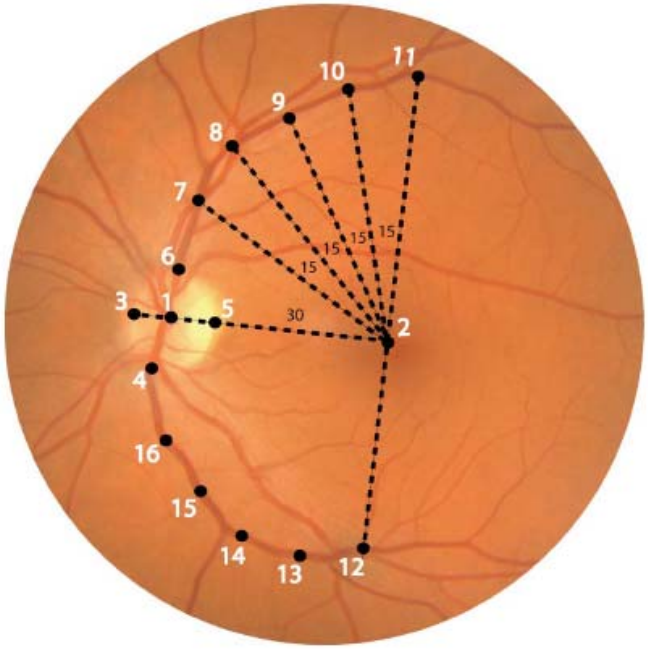

Figure 2.14. PDM for the detection of the optic disc, vessel arch, and the fovea [83].

2.3 Segmentation of Lesions

2.2.1 Bright Lesion Segmentation

The appearance of bright lesions including hard exudates and cotton wool spots is a very important sign of DR. Bright lesion segmentation is an easier task once the optic disc is segmented. Previous work on bright lesion segmentation can be divided into four groups: thresholding-based [4][86]--[91]; region growing based [50][68][69]; edge detection based [53]; and supervised [73][74] [92]--[94].

Bright lesions are bright objects in the retina. The most straightforward way to segment them is thresholding. In [4], Goldbaum *et al.* found the vessels first and then the bright lesions were found in the green channel image where the intensity is more than 1.2 times the mean vessel intensity. Due to the large illumination invariance in the retinal image, it is impossible to find a global threshold for segmenting all bright lesions. In [88], Liu *et al.* proposed a dynamic thresholding algorithm which calculates a local threshold according to a local histogram. In [90], Sagar *et al.*

proposed a dynamic thresholding scheme based on Otsu's algorithm [95]. First, because the colour of bright lesions varies widely across patients and images, the images were normalized to a reference image using histogram specification. Then the images were enhanced through local contrast enhancement. Then the dynamic thresholding was applied on the green channel of the image. The image was divided into blocks of 64x64 pixels each and there was 50% overlap between adjacent pairs so that each pixel belongs to four blocks as shown in Figure 2.15. If the histogram of a block were unimodal, a high threshold value was set. Otherwise Otsu's thresholding algorithm [95] was used to find the threshold for the block. The threshold t of a candidate pixel is interpolated from the threshold values of the four blocks to which it belongs as described by Equation 2.21.

$$t = t_1 \times \frac{(x_2 - x)(y_2 - y)}{(x_2 - x_1)(y_2 - y_1)} + t_2 \times \frac{(x - x_1)(y_2 - y)}{(x_2 - x_1)(y_2 - y_1)} + t_3 \times \frac{(x - x_1)(y - y_1)}{(x_2 - x_1)(y_2 - y_1)} + t_4 \times \frac{(x_2 - x)(y - y_1)}{(x_2 - x_1)(y_2 - y_1)} \tag{2.21}$$

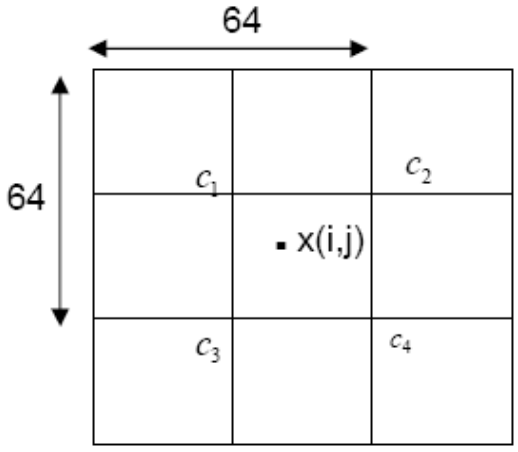

Figure 2.15. Dynamic thresholding [90].

Region growing is the classic technique for finding connected regions in an image [54]. In [50], Sinthanayothin proposed a recursive region growing segmentation (RRGS) algorithm to segment hard exudates based on the fact that adjacent pixels in an exudate should have fairly homogeneous grey scale properties. Using an initial pixel as a seed, the difference between the seed and its neighbors was calculated. If the difference was small, the neighbor was set as a seed. This procedure was repeated until no more neighbors could be merged as seeds. Once the whole image was completely segmented into different regions, the regions were thresholded as exudate or non-exudate using the median intensity of the region. In [68][69], Li and Chutatape proposed a region growing to segment exudates based on the fact that adjacent pixels in an exudate should have fairly homogeneous color properties. First the retinal image was divided into 64 subimages. Then, in each subimage, the pixels adjacent to seeds were tested, and the region was allowed to grow from the seeds until reaching a strong edge.

A strong edge is a significant feature of bright lesions, especially for hard exudates. In [90], Sagar *et al.* used edge information to distinguish exudates from non-exudates in the thresholded image. In [68][69], Li and Chutatape used the edge information as a constraint to stop the region growing. In [46], Walter *et al.* used edge information to locate candidate exudates. First, because most of the vessels have strong edges, all vessels in the retinal images were erased using morphological closing. The variation in the local intensity of each pixel within a local window $W(x)$ is calculated using Equation 2.22 where e_1 is the vessel erased image, μ is the mean intensity. The local intensity variation was produced by thresholding the edge map of the bright objects and then the regions inside edges were filled to obtain exudates candidates. Next, all candidates in the original image were filled using

morphological reconstruction to generate the background image. Finally the exudates were segmented by thresholding the difference between the original image and the background image. Figure 2.16 illustrates this procedure.

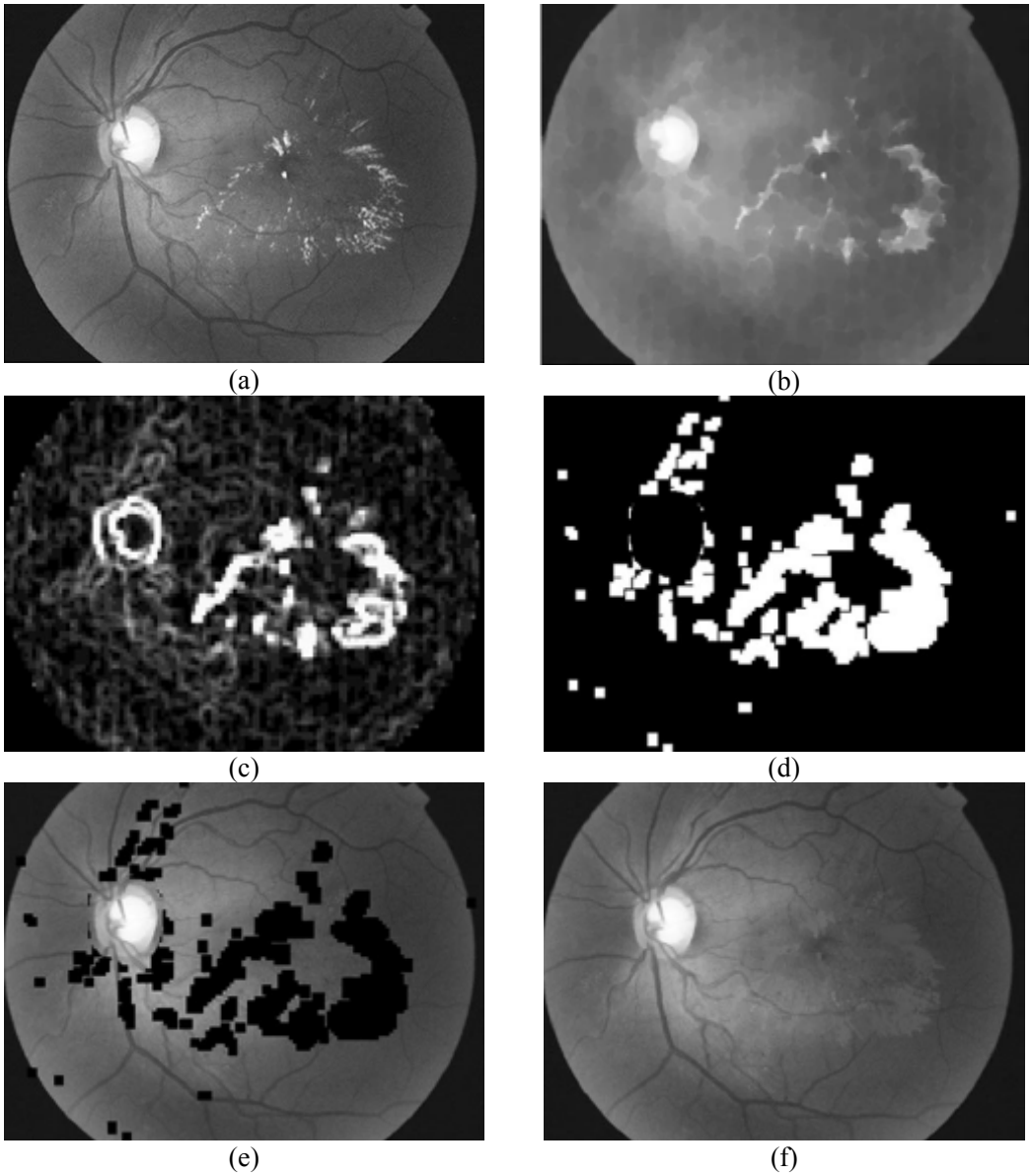

Figure 2.16. Bright lesion segmentation by edge detection and morphological reconstruction [53]. (a) Original image; (b) Vessel erased image; (c) Local intensity variation; (d) & (e)exudate candidates; (f) Background image.

$$e_2(x) = \frac{1}{N-1} \cdot \sum_{\xi \in W(x)} \left(e_1(\xi) - \mu_{e_1}(x) \right)^2 \tag{2.22}$$

Using manually segmented bright lesion samples, it is also possible to segment bright lesions using supervised methods [73][74] [92]--[94]. Wang *et al.* [92] segmented bright lesions by applying a Bayesian statistical classifier and using color

features as a feature space. In [73][74], Osareh *et al.* proposed a two step segmentation: unsupervised clustering followed by supervised classification. First, a Fuzzy C-Means clustering [97] was used to segment the candidate exudates. Then a neural network was applied to classify the exudates from non-exudates. In [93][94], Sanchez *et al.* proposed to segment the hard exudates by using a multilayer perceptron (MLP) classifier. First the retinal image was segmented to coarsely find all exudate candidate regions. Then, 24 features including the mean RGB values inside the region, the region size, the region edge strength were extracted from the candidate regions. The feature selection was carried out using a classifier-independent technique called logical regression (LR). Finally, the selected features were used as inputs of the MLP classifier with one hidden layer and trained with the backpropagation algorithm [96]. In [49] Zhang and Chutatape proposed a bottom-up strategy for bright lesion segmentation and classification. First, the Improved Fuzzy C-Means clustering was proposed and applied in Luv color space to segment all candidate bright-lesion regions. Then the SVM classifier was used to classify all candidates as bright lesions or non-lesions. SVM is a statistical learning method that can map the input vector x into a high dimensional feature space by choosing a nonlinear mapping kernel [98]. The optimal separating hyperplane in the feature space is given by Equation 2.23 where y_i are the labels, K is the kernel function, b is the bias, α_i are the Lagrange multipliers. Using 2 features (edge strength and color difference between inside region and surrounding region) extracted from candidates regions, the candidates were classified to bright lesions or non-lesions. Finally the bright lesions were classified as hard exudates or cotton wool spots using 4 features (edge strength, color difference between inside region and surrounding region, region size, and u and v of Luv color space).

$$f(x) = \mathrm{sgn}\left(\sum_{i=1}^{l} y_i \alpha_i K(x_i, x) + b \right) \tag{2.23}$$

2.2.1 Red Lesion Segmentation

Red lesions such as intraretinal hemorrhages and microaneurysms are major signs of DR. Microaneurysms appear as small reddish isolated patterns of circular shape in fundus images such as color fundus images and fluorescein angiographies (FA) [11]. The diameter of a microaneurysm is normally smaller than 125 μm. Microaneurysms are situated on capillaries and capillaries are not visible in color fundus images and FA. Microaneurysms normally appear as isolated patterns. FA can be used to more accurately detect microaneurysm. They are not popular because they are invasive, costly, and may provoke allergic reactions. Most recent research works concentrated on color fundus images. Hemorrhages are much more difficult to segment than microaneurysms because they are unpredictable in size and shape and many are connected to blood vessels in fundus images.

Previous work on red lesion detection and segmentation can be grouped into 7 categories: (1) thresholding based [4][89]; (2) region growing based [50]; (3) circular Hough transform based [99]; (4) matched filter based [100]; (5) mathematical morphology based [101]--[110]; (6) block classification based [49][111][112]; (7) pixel classification based [113].

Red lesions appear as local minima in gray scale images and they can be segmented by thresholding. In [4], Goldbaum *et al.* first segmented blood vessels then from images extracted red lesions scaled between zero and 1.2 times blood vessel intensity. In [89], Ege *et al.* first estimated the background using a median filter then segmented the red lesion candidates by using a threshold setting below the background. Finally, they used three different classifiers, Bayes classifier,

Mahalanobis distance classifier, and KNN classifier [64] which were trained to classify the candidates as hemorrhages, microaneurysms, or non-lesions.

Region growing is a classic way to segment connected regions in an image [54]. In [50], Sinthanayothin *et al.* proposed segmenting all red lesion candidates using recursive region growing. Since red lesions are similar to blood vessels in color, this region growing method segmented vessels and red lesions together and then neural networks is used to remove all blood vessels.

Microaneurysms appear as red circular patterns in fundus images. They can be detected by their shape information. In [99], Abdelazeem proposed a Circular Hough Transform based method for segmenting all microaneurysms.

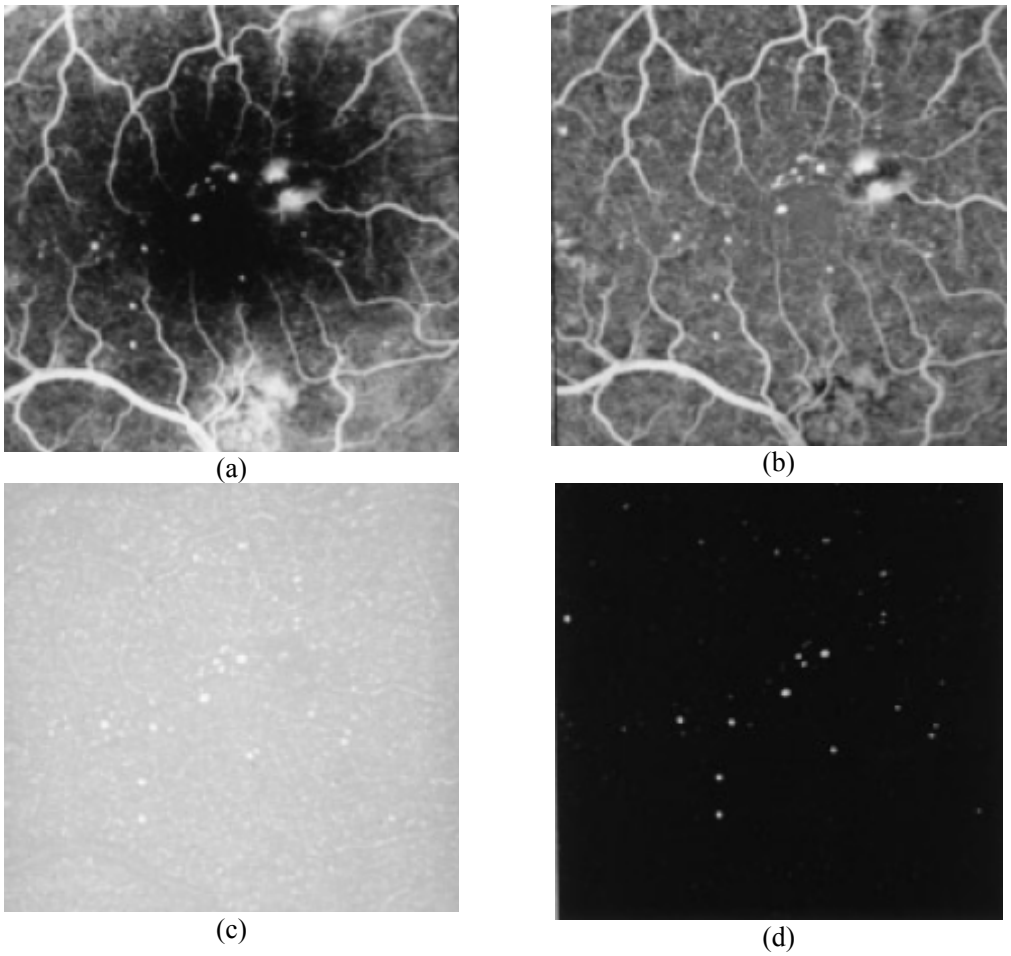

Figure 2.17. Spencer and Frame Scheme for microaneurysm segmentation [101][102]. (a) Original image; (b) shade corrected image; (c) vasculature removed by top-hat operation; (d) microaneurysms enhanced by the matched filter.

Microaneurysms can be regarded as 2D Gaussians in gray scale fundus images,moreover. They can be found by some filters “matching” them. In [100], Spencer *et al.* used the 2D Gaussian as the matched filter to find microaneurysms. Their work was done on FA images. In [101][102], Spencer *et al.* and Frame *et al.* first removed blood vessels by using morphological filters. Then the matched filter was used to enhance the contrast between background and red lesions. (See Figure 2.17 for more details) This work was also done on FA images.

Red lesions appear as morphological “holes” in fundus images, they can be found by a mathematical morphological operation. In [103], Øien and Osnes proposed a method for finding microaneurysms using morphological hit and miss operation. This was the first publication dealing with microaneurysm detection on color fundus images. In [101][102], Spencer *et al.* and Frame *et al.* proposed a microaneurysm segmentation scheme based on the fact that microaneurysms appear as small circular patterns but vasculature appears as a linear structure. A morphological top-hat transformation was used to discriminate between circular, non-connected red lesions and the elongated vasculature. First a shade correction was applied on the green channel of the image by subtracting the estimated background from the original image to “correct” the intensity variation on the background. Then the top-hat operation applied based on morphologically opening a FA image using a linear structuring element at 12 different orientations. The length of the structuring element should be larger than the largest microaneurysm. Therefore, microaneurysms were erased at all opened images. But the vasculature can remain in at least one opened image in which parts of the vasculature has the same orientation with the linear structuring element. Taking the maximum pixel value at each pixel location in all 12 images made it possible to obtain a map of only the vasculature. Finally

microaneurysms were enhanced using the 2D Gaussian matched filter. In [113], Niemeijer *et al.* extended this Spencer-Frame scheme on color fundus images. Bright lesions do not appear on FA images but they do appear on color fundus images. This can give rise to false positives. They first applied the shade correction and then removed all bright lesions by removing all pixels with a positive value from the shade corrected image. In [110], Fleming *et al.* segmented microaneurysms using the similar morphological operation. Their work focused on that how image contrast normalization can improve the ability to distinguish between microaneurysms and other dots that occur on the retina. A watershed transform based region growing was used to derive a region that contains no vessels or other lesions. False positives can also appear on the vasculature because there are many red dots on the vasculature due to the intensity variation. Finally, a local vessel detection technique was used to reject false detected microaneurysms on vessels. Because of the limited number of orientations considered by the morphological operations mentioned above, tortuous vessel like patterns that cannot contain a structuring element may be recognized as microaneurysms. In [107][108][109], criteria based closings were proposed to overcome this problem. In [53], Walter *et al.* defined diameter opening and diameter closing. Defining the diameter of a connected region as its max extension allows the diameter opening to be written as the supremum of all openings with structuring elements having a diameter greater than or equal to a threshold. The diameter closing was defined in the same way on the inverted image. First they applied the diameter closing on the green channel of the image and all microaneurysm candidates were thresholded. Then a trained KNN classifier was used to classify all candidates as microaneurysms or non-microaneurysms. Finally, vasculature was segmented to further reduce false positives.

Figure 2.18. Example of the first 10 eigen-red-lesions.

Block classification based methods [49][111][112] are effective ways to locate the center of microaneurysms. In [111], Gardner *et al.* proposed a neural network based technique for detecting red lesions. Each image was divided into 20 × 20 pixel blocks. Then each block was individually classified. In [112], Pallawala *et al.* proposed an eigenvector [64] based technique to extract microaneurysms. In [49], Zhang, and Chutatape defined the input pattern to the trained classifier as a 15 × 15 pixel window centered at the location of interest. The dimension of the input vector is $N \times N \times 3$ in color retinal images. PCA [64] was applied to reduce the dimension of the input space. The SVM [64] classifier was trained to locate the center of a red lesion. Finally the level set based technique was used to segment the red lesions.

A pixel classification based technique was proposed by Niemeijer *et al.* [113] to segment red lesion candidates, which is a possible solution to the problem caused by limited sizes considered by the methods mentioned above. Gaussian derivatives with different scales at each pixel were used as the input vector to the trained KNN classifier defined by Equation 2.24, where $p(redlesion)$ is the posteriori probability that a sign is a red lesion, *k* means *k* neighbors, and *n* of *k* neighbors are labeled as red lesions.

$$p(redlesion) = \frac{n}{k} \tag{2.24}.$$

Then the probabilistic map generated by the KNN classifier was thresholded to obtain all red lesion candidates. To avoid false negatives, the Spencer-Frame

scheme [101][102] was combined with pixel classification. Finally all candidates were classified using KNN [64] classifier through 21 features, such as area, circularity, compactness, generated from the candidates.

Chapter 3 Segmentation of Retinal Vessels

Images of the ocular fundus, also known as images of the retina, can tell us about retinal, ophthalmic, and even systemic diseases such as diabetes, hypertension, and arteriosclerosis [11][12]. These diagnoses often depend upon the appearance of blood vessels in the ocular fundus. One rather common retina-damaging complication of diabetes is prolifetive diabetic retinopathy (PDR), one sign of which is the appearance of neovascular (new vessel growth) [11][12]. The best approach to protecting against PDR is to screen for it and diagnosis it early. Retinal vessel information has been used in screening for Diabetic Retinopathy (DR) [9][10] and in diagnosing Retinopathy of Prematurity (ROP) [17][18] and we believe that the development of an efficient algorithm for the automated segmentation of blood vessels in retinal images would help eye-care specialists to screen larger populations for vessel abnormalities.

Many retinal vessel extraction methods have been proposed [3][4][9][10][16]-[40] yet retinal vessel extraction is still not as accurate as we might wish. The difficulty of accurate automated retinal segmentation is largely associated with the fact that (1) the width of retinal vessels can vary from very large to very small. To illustrate, consider that we manually cut many vessel cross-sections from the STARE [2] and DRIVE [4] database to observe the width of vessels and found that it varied from 3 pixels to 15 pixels); (2) the local intensity contrast of vessels can be weak and unstable; (3) different kinds of retinal lesions, especially bright lesions, may cause false positives in vasculature detection.

The rest of this chapter is organized as follows: Section 3.1 will describe a vessel segmentation technique using Multiscale Production of Matched Filters (MPMF) to

overcome the difficulties of vasculature width variance and weak contrast. Section 3.2 will describe a vessel segmentation technique that reduces false positives by using Modified Matched Filter with Double-Side Thresholding (MMFDST) to suppress the false positives caused by lesions. Section 3.3 will offer a conclusion.

3.1 Segmentation of Retinal Vessels Using MPMF

In this section, we describe the retinal vessel segmentation using Multiscale Production of Matched Filters (MPMF). Vessel segmentation is a specific line detection problem and hence many vessel extraction algorithms originated from line detection techniques [54]--[60]. In order to segment vessels, we usually need to enhance vessels at first. Vessel enhancement is usually implemented locally by using a window centered at the pixel to be enhanced. This class of techniques originated from the classical image processing problem: finding edges and lines in an image [54]--[60]. In [3], the matched filter was first proposed to detect retinal vessels. The matched filter is an effective technique for enhancing vessels by exploiting the prior information that the cross-section of the vasculature is Gaussian-shaped. However, the matched filter at a single scale cannot effectively enhance all the vessels of variant widths. Even when multiple filters with multiple scales are used, some small and weak vessels still cannot be detected due to the low density contrast and relatively heavy background noise. The Gabor filters were also employed [16][22] to enhance vessels. The use of mathematical morphology filters to enhance vessels was reported [23][36]. The Hessian based methods were reported in [37][33][34]. In [18], the vessels were enhanced through combing morphological filter and second derivative operator. Among above methods, the matched filter with threshold probing [20] provided good performance with relatively low complexity.

The matched filter is based on the prior knowledge that the cross-section of a retinal vessel is Gaussian-shaped. Therefore a Gaussian-shaped filter can be used to "match" the vessel. If there exists a vessel and its width matches the scale of the filter, a strong response will appear and then the vessel can be detected. Another advantage of the Gaussian-shaped matched filter is that it can smooth noise. In [20], a single scale matched filter was used to detect vessels in the retinal image and the scale of the filter was determined by experience. The matched filter with a single scale, however, cannot produce strong responses to all vessels in the retinal image when the width variance is large. To solve this problem, multiscale filters should be introduced.

Some multiscale schemes have been proposed for vessel detection [16][23][32][33][34]. In [16], the 2-D Gabor filters are applied to retinal images at different scales in order to account for vessels of different widths. In [23], a modified top-hat transform was applied to retinal images using circular structuring elements of different radius to detect vessels of different widths. In [32][33][34], the multiscale filter responses were synthesized by taking maximum responses along all scales after optimal normalization of filter responses at each scale. Those multiscale schemes synthesize the responses of several scales together as the final map of vessels. However, some small and weak vessels still cannot be detected because they are not successfully enhanced at any of the multiple scales.

In this section, we propose a new multiscale vessel extraction scheme that uses Multiscale Production of the Matched Filter (MPMF) responses as the multiscale data fusion strategy. The proposed MPMF vessel extraction scheme includes: (1) multiscale matched filtering and scale multiplication in the image enhancement step; and (2) double thresholding [55] in the vessel classification step. Considering that

the vessel structures will have relatively strong responses to the matched filters at different scales but the background noise will not, multiplying the responses of matched filters at several scales will further enhance the vessels while suppressing the noise. The vessel pixels can then be detected and fused in the scale production domain. This scale multiplication strategy has three advantages. One is that the vessels of variant widths can be detected concurrently because it can incorporate the multiscale information. Another is that it can detect the small and weak vessels which cannot be detected by other methods because the weak vessels could be better enhanced (while the noise being significantly suppressed) in the scale production domain. The third advantage of the proposed method over some snakes and tracking based classification methods [25]--[31][33][34] is that it is much easier to implement and has much lower complexity.

The rest of this section is organized as follows. Section 3.1.1 analyzes the problems in traditional matched filter. Section 3.1.2 defines our MPMF scheme. And the experimental results are given in section 3.1.3 to evaluate the performance of our MPMF scheme.

3.1.1 The Matched Filter and Its Problems in Vessel Enhancement

Since vessels are line-like structures, the retinal vessel enhancement methods originate from the classical image edge/line detection schemes [54]--[60]. Traditional line detection methods proceed either by finding parallel edges [56] or by finding ridges [57][58][59]. The major problem in traditional line detectors is that their performances are limited by the variances of line width. Parallel edge detection usually makes use of a bar-shaped model of lines. In [56], a pair of edge detectors (the first derivative of Gaussian) was used to detect the left and right edges of a line. Ridge-based detection methods usually use Gaussian-shaped line model. In

[57][58][59], the ridges were defined as the points on the image where the curvature reaches maximum. The second derivate of Gaussian is often used as a line detector in the ridge-based methods. The performances of all of those methods are limited by the selection of filter scale. To generate a single maximum response on the center of a line, the widths of the filter and the line should be constrained in a proper ratio. In order to detect lines of arbitrary widths, it is often necessary to iterate the detection procedure in the scale space.

The matched filter for retinal vessel detection was first proposed in [3] because it has been observed that the cross-section of the vessels in a retinal image is similar to a Gaussian function. A Gaussian-shaped filter can be used to "match" the vessels, to which strong filtering responses will be expected. The 2D matched filter is defined as a Gaussian function along the *x*-axis and this function is repeated in a neighborhood along the *y*-axis. Mathematically, the matched filter is defined by [3]

$$g(x,y) = -\exp\left(-x^2/\sigma^2\right) - m, \quad \text{for } |x| \le 3\sigma, \quad |y| \le L/2 \tag{3.1}$$

where σ represents the scale of the filter; $m = -\left(\int_{-3\sigma}^{3\sigma} \exp\left(-x^2/\sigma^2\right)dx\right)/6\sigma$ is used to normalize the mean value of the filter to 0 so that the smooth background can be removed after filtering; L is the length of the neighborhood along *y*-axis to smooth noise. In practice, we will rotate $g(x,y)$ to detect the vessels of different orientations and the maximum filter response of all orientations is retained as the final response at that scale. The rotation of $g(x,y)$ with angle ϕ is

$$\begin{cases} g^{\phi}(x',y') = g(x,y) \\ x' = x\cos\phi + y\sin\phi \\ y' = y\cos\phi - x\sin\phi \end{cases} \tag{3.2}$$

The setting of angular resolution is a relatively easy task. Based on the research in [3], the angular resolution larger than $\pi/12$ will not improve the detection

significantly. We use the same orientation setting as in [3], which ranges from $0 \sim 11\pi/12$ in the step of $\pi/12$. Same with classical line detector [54]--[60], how to set the scale, σ, of the matched filter is a key problem. In [3], the scale σ was set as 2 by experience. However, the widths of retinal vessels can vary from very large to very small and using just one scale $\sigma = 2$ cannot accurately detect all the vessels.

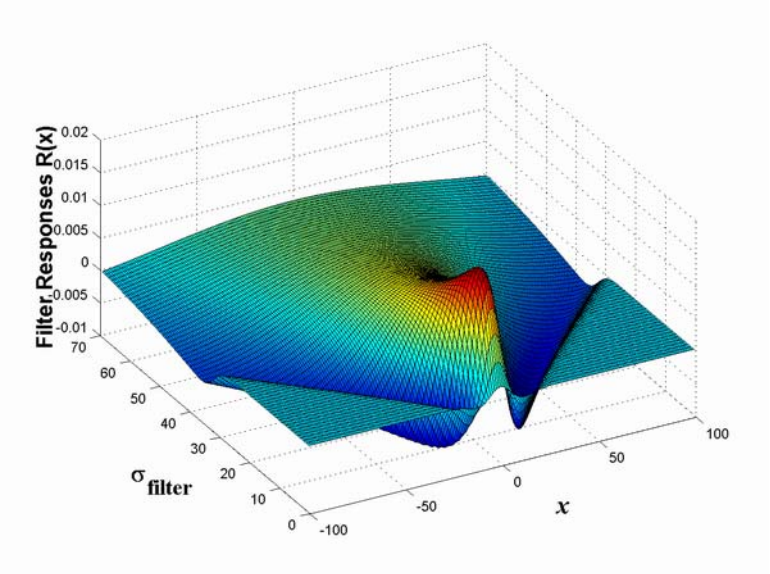

(a) Gaussian-shaped line

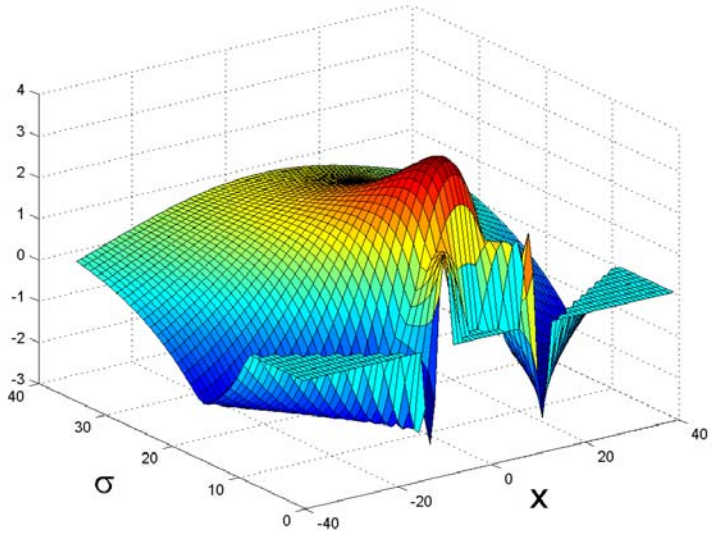

(b) Bar-shaped line

Figure 3.1. Matched filter response to a line model along scale space.

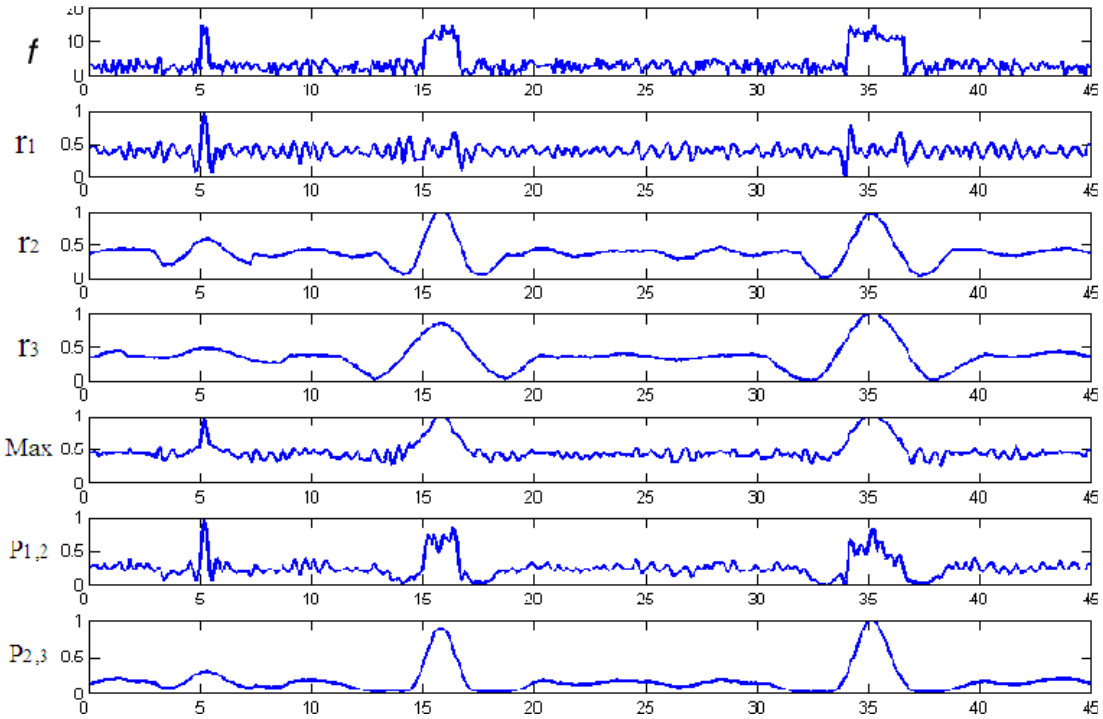

Figure 3.2. Multiscale matched filters and scale production. *s* is the original signal; *f* is the noisy measurement of *s*; R_1, R_2 and R_3 are the matched filter responses to *f* at different scales. *Max* means the maximum values among R_1, R_2 and R_3. $P_{1,2}$ is the scale production of R_1 and R_2, and $P_{2,3}$ is the scale production of R_2 and R_3. (Referring to Section 3.1.1 about $P_{1,2}$ and $P_{2,3}$.)

To analyze the scale of the matched filter, we denote by $G(x) = -\exp\left(-x^2/\sigma_{line}^2\right)$ the cross-section of a line model and denote by $g(x) = -\exp\left(-x^2/\sigma_{filter}^2\right) - m$ the matched filter. Here we skip the neighboring dimension y for the convenience of expression and discussion. The response of the line to the matched filter is $R(x) = G(x) * g(x)$, where * represents convolution. To generate a strong response in the center of the line, the scale of the filter, i.e. σ_{filter} should be properly selected. With a fixed line width, i.e. fixing σ_{line}, in Figure 3.1 we show the matched filter responses $R(x)$ by changing the filter scale σ_{filter}. We can see that for both bar-shaped and Gaussian-shaped line not every scale can lead to a strong

response. Only filters with particular scales can produce strong responses to the lines with particular widths.

In order to detect lines of variant widths, it is often necessary to iterate the detection procedure in the scale space instead of using only one scale as in [3][20]. Figure 3.2 simulates vessel detection using multiple matched filters. Original signal *s* consists of the cross-sections of several lines of different width. Noisy signal *f* is the measurement of *s* by adding background noise. R_i is the response of the matched filter to *f* at scale σ_i. As shown in Figure 3.2, small scale matched filters can detect the lines of small widths but they cannot detect the lines of big widths and cannot remove noise effectively. On the other hand, big scale matched filters can detect wide lines but they fail to detect the thin lines because the thin lines are smoothed too much. However, as the vessels in a retinal image can vary from very large to very small, it is rarely possible to find a single scale which is suitable for detecting all vessels.

Multiscale line detectors can be used to overcome the difficulty of single scale detector. We apply multiple filters at different scales to the signal and obtain multiple responses. Then a fusion strategy is used to synthesize the multiscale responses. The maximum rule is commonly used to fuse multiscale responses [16] [32][33][34] [37]. However, as seen in Figure 3.2, although both the big and small width vessels can be identified, too much noise is preserved and this noise will greatly degrade the final segmentation result.

3.1.2 The Multiscale Matched Filters using Scale Production

In [114], Mallat and Zhong illustrated mathematically that signals and noise have different singularities and that edge structures will present observable magnitudes along the scales, while noise will decrease rapidly. This property has been used by

Bao and Zhang [115][116] in the applications of noise reduction and edge detection. They used scale multiplication as a strategy to enhance edges and suppress noise. We adopt this idea to vessel detection and propose a multiscale matched filter scheme. The proposed method could be able to detect large and small vessels concurrently. It also offers an efficient way to suppress noise, making it possible to detect some small weak vessels with low local contrast.

3.1.2.1 Scale Production of the Multiscale Matched Filters

The effectiveness and efficiency of matched filters have been demonstrated in [3][20], where the retinal vessels are enhanced and extracted from noisy background using a single filter at a single scale. The matched filter is adopted in our multiscale scheme because it well exploits the prior knowledge that the cross-section of a retinal vessel is Gaussian-shaped. We re-write the function of the matched filter defined in Equation 3.1 as

$$g_i(x,y) = -\exp\left(-x^2/\sigma_i^2\right) - m_i, \quad \text{for } |x| \le 3\sigma_i, \quad |y| \le L_i/2 \tag{3.3}$$

where σ_i is the standard deviation of the Gaussian function at scale. Correspondingly, $m_i = -\int_{-3\sigma_i}^{3\sigma_i} x\exp\left(-x^2/\sigma_i^2\right)dx$, and is the length of the filter in y direction at that scale. The rotation of $g_i(x,y)$ with angle ϕ is then implemented by using $g_i^{\phi}(x',y') = g_i(x,y)$, where $x' = x\cos\phi + y\sin\phi$ and $y' = y\cos\phi - x\sin\phi$. Figure 3.3 (a) plots the 1D cross section of a matched filter and Fig. 3.3 (b) shows the 2D matched filters at 3 different scales and in 8 directions.

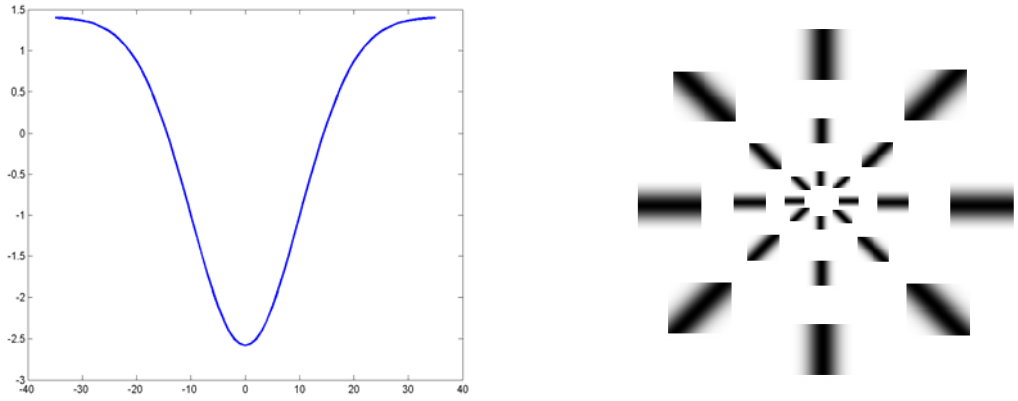

(a) **(b)**

Figure 3.3. (a) The 1-D cross section of a matched filter. (b) The 2-D matched filters at 3 different scales and in 8 directions.

Without loss of generality and for the convenience of expression, we only discuss the multiscale matched filter in the horizontal direction. The filters in other directions can be derived similarly. The response of a matched filter $g_i(x,y)$ to an input image $f(x,y)$ can be expressed by

$$R_i(x,y) = g_i(x,y) * f(x,y) \tag{3.4}$$

The scale production is defined as the product of filter responses at two different scales

$$P_{i,j}(x,y) = R_i(x,y) \cdot R_j(x,y) \tag{3.5}$$

Referring to Figure 3.2, examples of the scale multiplication of the matched filters are shown. $P_{1,2}$ is the production of the filter responses at scales 1 and 2, while $P_{2,3}$ is the production of the filter responses at scales 2 and 3. Obviously, the filter responses to vessels of all widths can be better enhanced in $P_{1,2}$ and $P_{2,3}$ than in R_1, R_2 and R_3. The noise is also better suppressed in $P_{1,2}$ and $P_{2,3}$. The width of thin vessels will be enlarged by large scale filters, such as g_2 and g_3. Interestingly, this distortion could be corrected to some extent by employing a smaller scale filter in the scale production, as we can see in $P_{1,2}$. Finally, the vessels of variant widths

and noise can be more easily discriminated in the scale production than in the original filter responses by using a simple thresholding strategy.

Based on the above observation and discussion, in our multiscale matched filters, the production $P_{1,2}$ is used to extract small, thin vessels and the production $P_{2,3}$ is used to extract big, wide vessels after thresholding. We will then get two binary vessels maps and they are directly fused by using an "OR" logic operation to yield the final vessel map. Two key issues in our scheme are multiscale selection and thresholding.

3.1.2.2 Multiscale Selection

In our multiscale matched filter scheme, three filters at three scales (small, middle, and big) are employed and hence two scale productions are computed. The selection of scales is very important. In the case of retinal images, the widths of vessels vary from 3 to 15 pixels (STARE and DRIVE databases). To determine the reasonable scales of the three filters, there are two issues required to be figured out: (1) Small vessels are overwhelmed by Gaussian noises; (2) High frequency signal with high energy can pass low frequency band of a band-pass filter so that small vessel's width can be over-estimated. Our objectives are to generate good signal-to-noise ratio and good width information. We analyze the scale selection using both Gaussian model vessel and bar model vessel. The bar model is defined by Equation (3.6) where *w* is the width of a vessel. The Gaussian model is defined by Equation (3.7) where is the σ standard derivation and the width is estimated by 3σ. We re-defined matched filter using the second derivative of Gaussian in Equation (3.8) and (3.9). Equations (3.6)-(3.8) are illustrated in Figure 3.4.

$$v(x) = \begin{cases} -h, & |x| \le w \\ 0, & |x| > w \end{cases} \tag{3.6}$$

$$g_\sigma(x) = -\frac{1}{\sqrt{2\pi}\sigma} e^{-\frac{x^2}{2\sigma^2}} \tag{3.7}$$

$$g_\sigma^{''} = \frac{x^2 - \sigma^2}{\sqrt{2\pi}\sigma^5} e^{-\frac{x^2}{2\sigma^2}} \tag{3.8}$$

$$m_\sigma(x, y) = \frac{x^2 - \sigma^2}{\sqrt{2\pi}\sigma^5} e^{-\frac{x^2}{2\sigma^2}}, \quad for \quad |y| \le L/2 \tag{3.9}$$

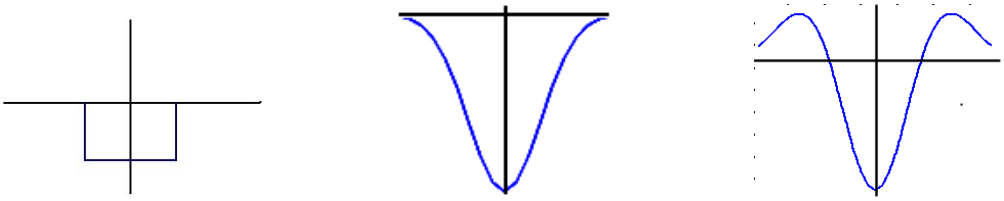

(a) (b) (c)

Figure 3.4. Vessel modelled using Gaussian (a) and bar (b), and the matched filter defined using second derivative of Gaussian.

Matched filter response described using bar model is

$$\begin{aligned} r(x, \sigma, w, h) &= g_\sigma^{''}(x) * v(x) \\ &= \int_{-\infty}^{\infty} g_\sigma^{''}(t) v(x-t) dt \\ &= \int_{-\infty}^{x-w} g_\sigma^{''}(t) \cdot 0 dt + \int_{x-w}^{x+w} g_\sigma^{''}(t) \cdot (-h) dt + \int_{x+w}^{\infty} g_\sigma^{''}(t) \cdot 0 dt \\ &= h\left(g_\sigma^{'}(x-w) - g_\sigma^{'}(x+w) \right) \end{aligned} \tag{3.10}$$

where

$$g_\sigma^{'}(x) = \frac{-x}{\sqrt{2\pi}\sigma^3} e^{-\frac{x^2}{2\sigma^2}} \tag{3.11}.$$

By solving

$$\frac{\partial r(0, \sigma, w, h)}{\partial \sigma} = 0 \tag{3.12},$$

we have r to exhibit a local maximum at center of a bar if $\sigma \geq \frac{w}{\sqrt{3}}$. Width is estimated as the zero-crossings of the filter response r. The zero-crossings can be found by solving Equation (3.13)

$$g'_{\sigma}(x-w) = g'_{\sigma}(x+w) \Rightarrow e^{\frac{2xw}{\sigma^2}} = \frac{x+w}{x-w} \qquad (3.13).$$

This Equation can only be solved numerically as illustrated in Figure 3.5. We can see that the best width is estimated by $\sigma = \frac{w}{\sqrt{3}}$. The larger scale makes the worse width estimation.

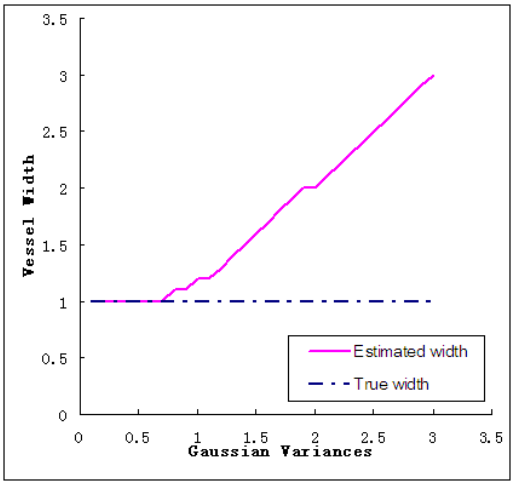

Figure 3.5. Filter peak responses to the thinnest and widest vessels along scale space.

Following we analyze the filter response normalization according to this observation. Filter response is required to be normalized because it decreases along scales. Here we re-write the classical ridge normalization multiplier derivation by Lindeberg [122] for Gaussian model. Equation (3.14) is the center filter response produced by convolving the second derivative of Gaussian whose standard variation is σ with the Gaussian whose standard variation is σ_0.

$$r^{lind}(0,\sigma,\sigma_0)=\frac{1}{(2\pi)^{1/2}(\sigma+\sigma_0)^{3/2}} \tag{3.14}$$

The filter response normalization is defined in Equation (3.15) using a multiplier.

$$r^{lind}_{\alpha-norm}(0,\sigma,\sigma_0)=\sigma^{\alpha}r(0,\sigma,\sigma_0,h) \tag{3.15}$$

The peak of Equation (3.15) can be found by solving Equation (3.16).

$$\frac{\partial r^{lind}_{\alpha-norm}(0,\sigma,w,h)}{\partial\sigma}=0 \quad \Rightarrow \quad \sigma=\frac{2\alpha}{3-2\alpha}\sigma_0 \tag{3.16}$$

We have $\alpha=\frac{3}{4}$ by setting $\sigma=\sigma_0$.

Because the vessel is not really Gaussian, we derive the normalization multiplier using bar model. Equation (3.17) is the center filter response produced by convolving the second derivative of Gaussian whose standard variation is σ with the bar whose width is w.

$$r(0,\sigma,w,h)=h\left(g'_{\sigma}(-w)-g'_{\sigma}(w)\right) \tag{3.17}$$

The normalization is defined by Equation (3.18). The peak of Equation (3.18) can be found by solving Equation (3.19).

$$r_{\alpha-norm}(0,\sigma,w,h)=\sigma^{\alpha}r(0,\sigma,w,h) \tag{3.18}$$

$$\frac{\partial r_{\alpha-norm}(0,\sigma,w,h)}{\partial\sigma}=0 \quad \Rightarrow \quad \sigma=\frac{w}{\sqrt{3-\alpha}} \tag{3.19}$$

We have $\alpha=2$ if $\sigma=w$.

In fact, vessel is bar smoothed by Gaussian, so the normalization should be set in $\frac{3}{4}<\alpha<2$. Small α can not give large scale filter enough compensation but

large α will over-estimate width. In our experiments, we empirically found that setting α around 5/4 is a good balance between filter peak response and width estimation.

Good normalization is helpful to width estimation, but the fact that retinal vessel width varies a lot makes the multiscale selection difficult. We propose a solution based on a middle scale which (1) will denoise for small vessel; (2) will not over-estimate small vessel width much; (3) will give reasonable response for large vessel. Following we describe how to find this middle scale. The center matched filter response described using bar model is defined in Equation (3.20).

$$\begin{aligned} r(0,\sigma,w,h) &= h\left(g_\sigma'(-w) - g_\sigma'(w)\right) \\ &= h\left(\frac{w}{\sqrt{2\pi}\sigma^3}e^{-\frac{w^2}{2\sigma^2}} - \frac{-w}{\sqrt{2\pi}\sigma^3}e^{-\frac{w^2}{2\sigma^2}}\right) \\ &= \frac{2hw}{\sqrt{2\pi}\sigma^3}e^{-\frac{w^2}{2\sigma^2}} \end{aligned} \tag{3.20}$$

For retinal vessels in STARE and DRIVE database, $\mathbf{1 \le w \le 7}$. Therefore the middle scale can be found by solving Equation (3.21).

$$e^{-\frac{1}{2\sigma^2}} - 7e^{-\frac{7^2}{2\sigma^2}} = 0 \quad \textit{and} \quad \sigma \ge \frac{7}{\sqrt{3}} \tag{3.21}$$

Because the bar-model may not describe vessel perfectly, we find the middle scale by learning the retinal database. We manually cut 100 cross-sections of the smallest/largest vessels and use the averaging as model to describe smallest/largest vessel. And then we use the learned vessel model to produce filter response $r_{\alpha-norm}(0,\sigma,1,1)$ and $r_{\alpha-norm}(0,\sigma,7,1)$. Finally the middle scale can be numerically solved by finding the cross of $r_{\alpha-norm}(0,\sigma,1,1)$ and $r_{\alpha-norm}(0,\sigma,7,1)$. This procedure is illustrated in Figure 3.6.

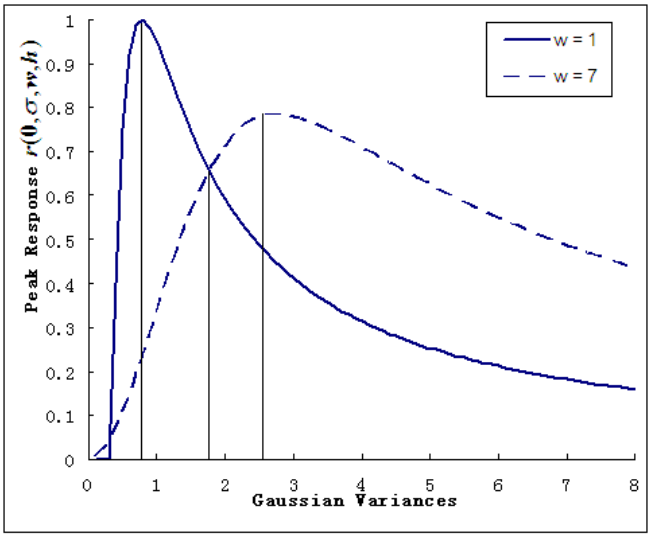

Figure 3.6. Filter peak responses to the thinnest and widest vessels along scale space.

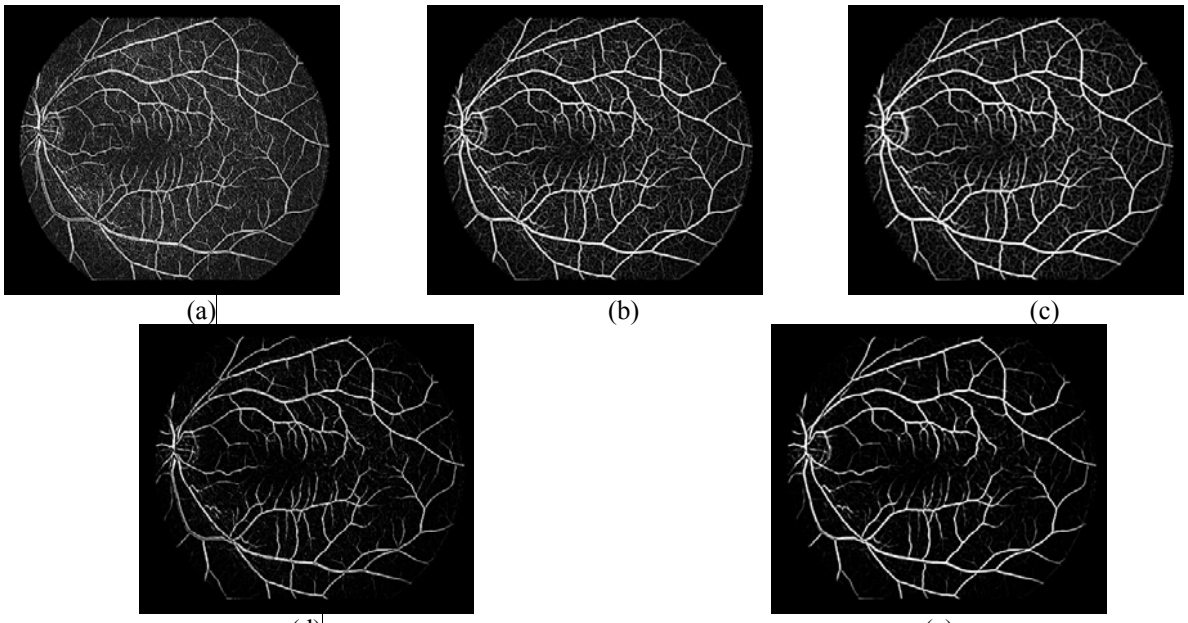

Figure 3.7. Multiscale filtering of a retinal image. (a), (b), and (c) are the matched filter responses to the retinal image at three scales; (d) is the scale production of (a) and (b); (e) is the scale production of (b) and (c).

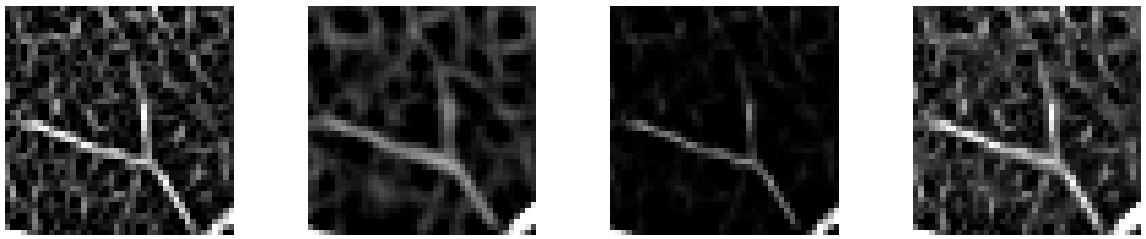

Figure 3.8. (a) and (b) are cropped and enlarged images from Figures 3.5 (a) and (b); (c) is the scale production of (a) and (b); (d) is the maximum of all the three scales (a), (b) and (c) in Figure 3.5.

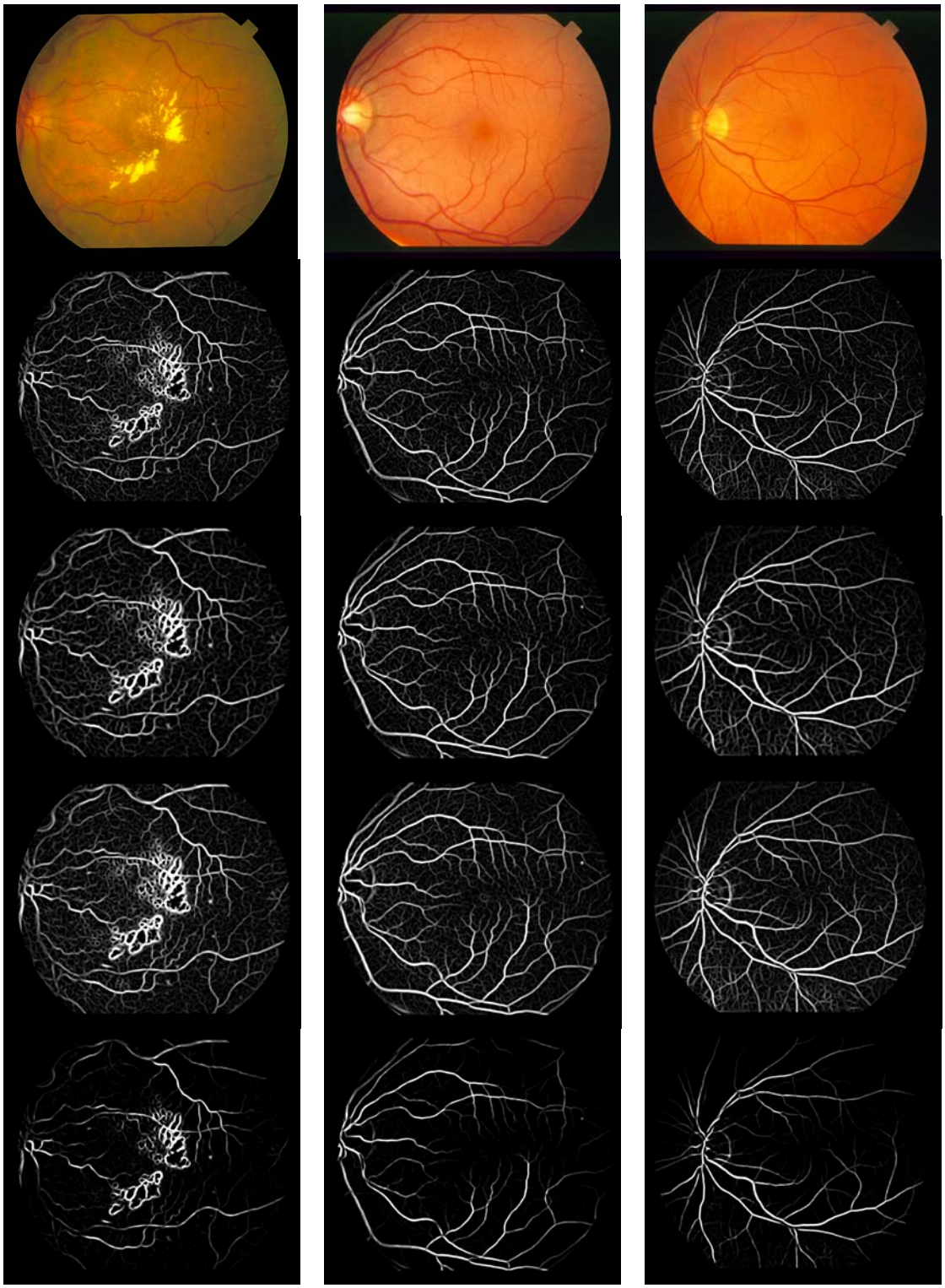

Figure 3.9. Fusion of multiscale line responses. First row gives the original images. Second row and third row are line responses at different scale. Fourth row gives the maximum of multiscale line responses. Last row gives the scale products of multiscale line responses.

We see that the matched filer g_i will get the highest response to the thin vessel if its scale parameter is set as $\sigma_i = r_1(0.8)$. On the other hand g_i will get the highest response to the wide vessel if its scale parameter is set as $\sigma_i = r_3(2.6)$. The two curves cross at $\sigma_i = r_2(1.8)$. Guided by Figure 3.4, we set the scales of the three matched filters as $\sigma_1 = r_1$, $\sigma_2 = r_2$ and $\sigma_3 = r_3$, respectively. Correspondingly the three filters are denoted as g_1, g_2 and g_3. We detect the small, thin vessels in the scale production $P_{1,2}$ of the responses of g_1 and g_2, and detect big, wide vessels in the scale production $P_{2,3}$ of the responses of g_2 and g_3. Figure 3.7 shows an example of the proposed multiscale filtering scheme. Figure 3.7 (a)-(c) are the filter responses R_1, R_2, and R_3 at scales $\sigma_1 = r_1$, $\sigma_2 = r_2$ and $\sigma_3 = r_3$. Fig. 3.7 (d) is the scale production $P_{1,2}$ and Figure 3.7 (e) is the scale production $P_{2,3}$. We see that $P_{1,2}$ and $P_{2,3}$ suppress most of the noise and well enhance the thin and wide vessels respectively. For a better visualization to show the effectiveness of scale production, we crop and zoom-in part of the images in Figure 3.8. Figure 3.8 (a) and (b) are cropped and enlarged from Figure 3.7 (a) and (b). Figure 3.8 (c) is cropped and enlarged from Figure 3.7 (d). For the purpose of comparison, in Figure 3.8 (d) we show the result by applying the max rule on the three response images. It is seen that scale production can better discriminate vessels from background noise while the max rule can introduce many false vessel pixels. Figure 3.9 gives more examples to show the performance of scale production.

3.1.2.3 Thresholding

We determine the three matched filters of variant scales and then apply them to the retinal image and obtain three responses. The responses are multiplied to obtain two

scale production images, one in which the responses to vessel structures are enlarged in the other the responses to noise are weakened.

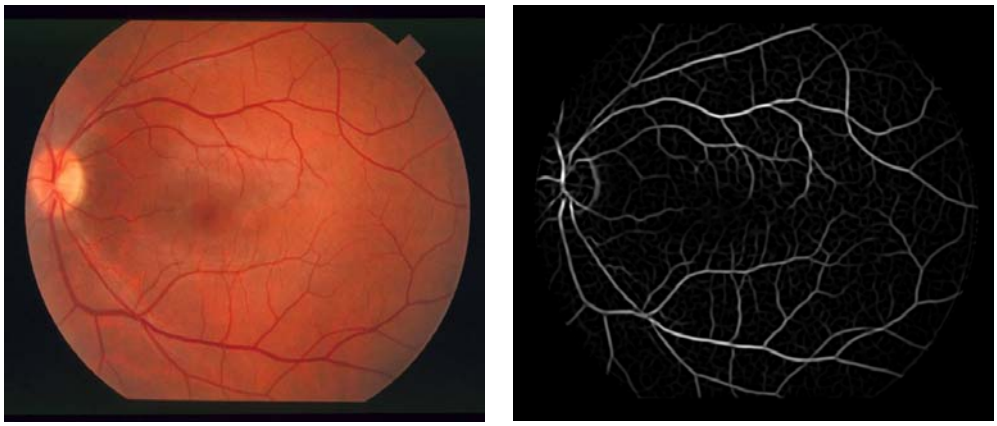

(a) (b)

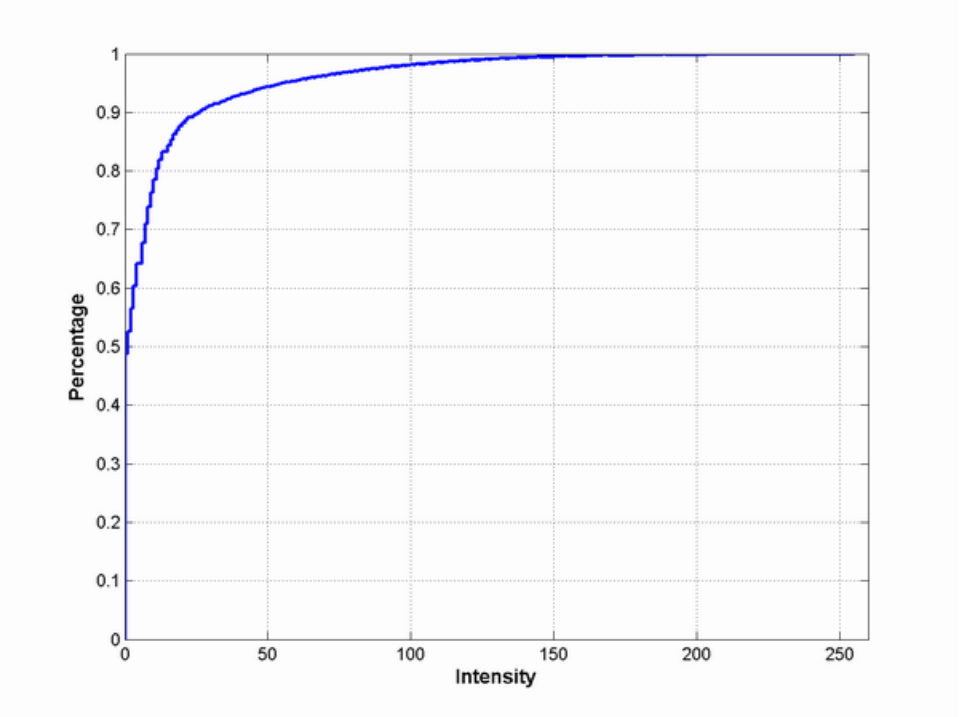

(c)

Figure 3.8. Amplitude distribution of the matched filters response of a retinal image.

A simple single-thresholding or double-thresholding [55] operation could effectively distinguish vessels from noise. Since double-thresholding can better suppress noise while preserving the connectivity of lines and edges, we adopt this strategy as in [55] and apply it to both $P_{1,2}$ and $P_{2,3}$. Take $P_{1,2}$ for example, with double-thresholding a low threshold t_l and a high threshold $t_h = 2t_l$ are imposed on $P_{1,2}$ and then two vessels maps V_l and V_h are obtained. The final vessel map

will be formed by selecting vessels in V_l that link to the vessels in V_h. We implement double-thresholding through morphological reconstruction.

Following we discuss how to find t_l. Generally, there are two kinds of strategies to determine the thresholding parameter: (1) Learning the database to obtain an "optimal" t_l; (2) Selecting t_l according to users' requirement. We introduce 2 learning methods here. In the experiments of this work, we find the "optimal" t_l by exhausting all possible values. A simple way to determine t_l is to use the fact that the background area is normally the same for human beings. Figure 3.8 gives an example of the amplitude distribution of the matched filter responses. Figure 3.8(a) is an original image ($f(x,y)$; Figure 3.8(b) is its scale products of Gabor responses ($P^{s_j}(x,y)$; Figure 3.8(c) is the cumulative histogram of (b). By observing retinal images of large populations, the vessels occupy 10% - 15% of a retina, which means the background is 85% - 90%. Therefore we can set t_l and t_h based on the percentage of background area.

Another way is based on the fact that filter responses to noise and vessels should have different distributions. Suppose the background noise in retinal image $f(x,y)$ is Gaussian white noise $n(x,y)$ with zero mean and standard deviation υ where υ is learned from retinal images. The filters' responses to $n(x,y)$ at two scales are $N_1(x,y) = g_1(x,y) * n(x,y)$ and $N_2(x,y) = g_2(x,y) * n(x,y)$. N_1 and N_2 are smoothed noise images and their standard deviations are respectively $\upsilon_1 = \|g_1\|\upsilon$ and $\upsilon_2 = \|g_2\|\upsilon$, where $\|g(x,y)\| = \sqrt{\iint g^2(x,y)dxdy}$ is the norm of the filter. N_1 and N_2 are jointly Gaussian distributed with correlation coefficient

$$\rho_{1,2} = \frac{\iint g_1(x,y) \cdot g_2(x,y) dxdy}{\sqrt{\iint g_1^2(x,y) dxdy \cdot \iint g_2^2(x,y) dxdy}} \tag{3.6}$$

If the input image is pure noise $n(x,y)$, the scale production will be $Z_{1,2}(x,y) = N_1(x,y) \cdot N_2(x,y)$. The probability density function (PDF) of $Z_{1,2}$ is [117] (p. 42)

$$\Pr(z) = \frac{1}{\pi \Gamma(1/2)\sigma_1\sigma_2\sqrt{1-\rho^2}} \exp\left(\frac{\rho z}{(1-\rho^2)\sigma_1\sigma_2}\right) K_0\left(\frac{|z|}{(1-\rho^2)\sigma_1\sigma_2}\right) \tag{3.7}$$

where $\Gamma(t) = \int_0^\infty e^{-u} u^{t-1} du$ is the Gamma function and K_0 is the modified Bessel function of the second kind with order zero. The standard deviation of $Z_{1,2}$ is

$$\kappa = \sqrt{E[z^2]} = \sqrt{1+2\rho_{1,2}^2} \cdot \upsilon_1\upsilon_2 \tag{3.8}$$

We take $t_l = c\kappa$ as the low threshold to suppress $Z_{1,2}$ in $P_{1,2}$, where c is a constant. The values in $P_{1,2}$ below t_l are removed as noise and the remaining values are extracted as vessel map V_l. $t_h = 2c\kappa$ is then used to obtain another map V_h. Selecting the vessels in V_l that link to the vessels in V_h leads to the vessel map according to $P_{1,2}$. The same procedure goes to $P_{2,3}$ and the final vessel map is made by fusing the outputs of $P_{1,2}$ and $P_{2,3}$ with "OR" logic operation.

3.1.2.4 Post-processing

The MPMF works well for normal retinal images but not for abnormal (pathological) retinal images because retinal lesions may cause false positives. Therefore some post-processing operations are used to improve the segmentation accuracy. Figure 3.9 (a) and (b) shows an abnormal retinal image segmented by the proposed MPMF scheme. We can see that there are 2 major problems: (1) the false positives caused by

bright lesions; and (2) some unlinked small vessels. In this section, we implement some simple post-processing procedures to solve the two problems.

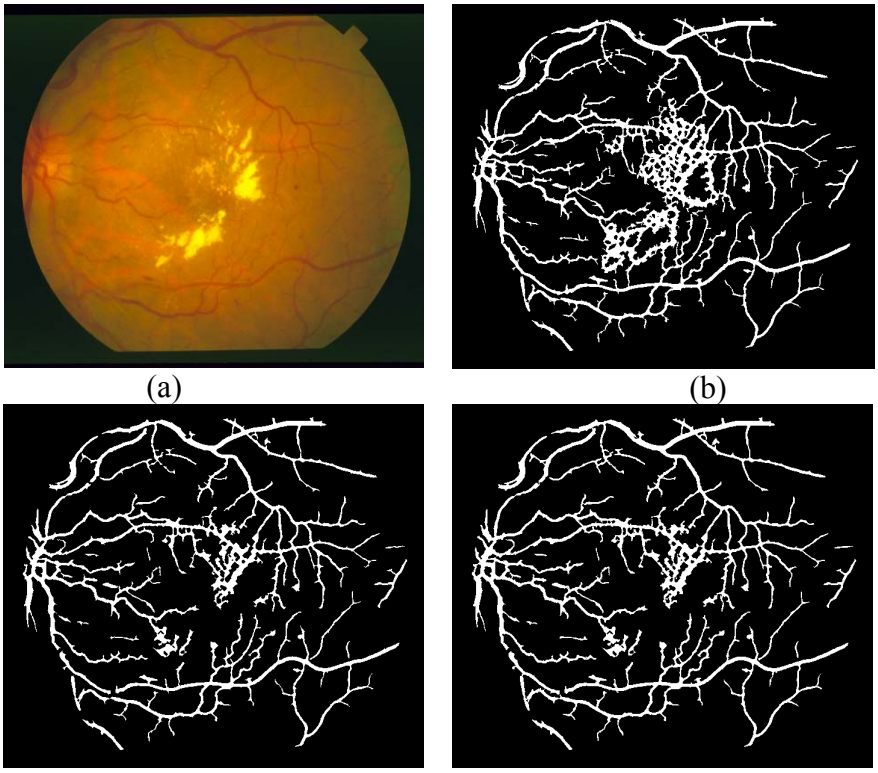

(a) (b) (c) (d)

Figure 3.9. The vessel segmentation of a retinal image with bright lesion. (a) The original image with bright lesions in STARE database; (b) Vessel segmentation result by MPMF; (c) Suppress false positives caused by bright lesions; and (d) link small broken vessels.

(a) (b) (c) (d)

Figure 3.10. (a) and (c) are cropped and enlarged images from Figure 3.9 (a); (b) and (d) are cropped and enlarged images from Figure. 3.9 (d).

Eliminating the false positives caused by bright lesions

The matched filter responses not only to Gaussian-shaped lines but also to step edges; the bright lesions can cause false positives. In [27], the vessels were extracted by tracing parallel edges. In their model, each vessel pixel should have two edge pixels along the normal direction, and the gradient direction of each edge pixel should be

the opposite of the other (both of them should normally point outward). This idea was adopted by [32] to suppress the matched filter response to bright lesions. We adopt this parallel-edge vessel model in the post-processing of the proposed MPMF scheme. For each vessel pixel classified by the MPMF, i.e. for each white pixel in Figure 3.9 (b), we find the pair of boundary pixels along the normal direction of the vessel. The normal direction is defined as the direction with the maximum matched filter response. The boundary pixels are simply generated by subtracting Figure 3.9 (b) from its dilated version. The gradient map is generated using a canny operator. If the gradient direction of both the two boundary pixels is pointing outward normal, the current vessel pixel is classified as a true positive. Otherwise it is a false positive. Figure 3.9 (c) shows the false positive eliminating result of Figure 3.9 (b).

Linking broken vessels

The broken vessels in Figure 3.9 (b) are caused by the vessels with discontinuous intensities, especially the small vessels whose intensities are very close to background. Even though the matched filter has already smoothed the intensity along the direction of the tangent of vessels, the matched filter responses of some pixels are still too weak to distinguish them from noise. Although the tacking based methods [31] can somewhat improve the segmentation result, they are iterative and very time consuming. Here we use an anisotropic morphological operation to link the broken vessels segmented by MPMF. First, we segment the scale production using a very low threshold $t_{vl} = \alpha t_l$, where α is a constant (we set $\alpha = 0.3$). The pixels within interval $[t_{vl}, t_l]$ are defined as potential vessel pixels to be linked. At each potential vessel pixel, we apply morphological closing using a linear structure. The direction of the linear structure is perpendicular to the direction of the maximum matched filter response. In the experiments we set the length of the linear structure

are 9 pixels. Figure 3.9 (d) shows the vessel linking result of Figure 3.9 (c). To make it easier to see, we have cropped and zoomed-in part of the images in Figure 3.9 and show them in Figure 3.10.

3.1.2.5 Computational complexity

In this section, we discuss the computational complexity of MPMF. MPMF consists of convolution and thresholding. The convolution complexity of MPMF is $O(n)$ where n is the image size. The thresholding complexity of MPMF is $O(n \cdot r)$ where r is the parameter to control morphological reconstruction. The convolution complexity of Hoover's method [20] is also $O(n)$. But the thresholding of Hoover's method is $O(n \cdot r \cdot k)$ where k is the parameter to probe thresholds. Mendonça's method [23] consists of modified top-hat operation and multiscale thresholding. The top-hat operation is $O(n)$ and the multiscale thresholding is $O(n \cdot r \cdot s)$ where s is the parameter to control scales. Generally k is much larger than s so that Hoover's method [20] is most time consuming and MPMF is most efficient.

3.1.3 Experimental Results

In this section we describe two sets of experiments. In the first set, the proposed scheme was applied to retinal images we collected for diabetic retinopathy (DR) screening. In the second set, we applied it to the STARE and DRIVE retinal image databases so as to make comparisons with other vessel extraction schemes.

3.1.3.1. Experiments on the diabetic retinal images

We apply the proposed method to retinal images with DR to evaluate its performance in DR screening. These images[2] were collected using a Kowa VK-3 fundus camera at 45^{o} field of view (FOV) and stored in a 24-bit digital format. The spatial resolution of the images is 800×608 pixels. The appearance of Neovascularization (new vessels growth) stands for proliferative diabetic retinopathy (PDR) [11][12], which is a very severe stage of DR. Neovasculars are small, thin vessels. If they can be automatically detected, it will be particularly helpful to the eye-care specialists in PDR diagnosis.

We compared the proposed MPMF scheme with three other state of the art schemes: the traditional matched filter developed by Chaudhuri *et al* [3]; the scheme developed by Hoover *et al* [20]; and a scheme that applies the max rule to the multiscale responses.

Figure 3.11 (a) shows a PDR retinal image; (b) shows the extracted vessel image using the matched filter [3]; (c) is the output of method [20]; (d) is the result obtained by using the max rule on three scales; and (d) is the vessel map obtained by using the proposed MPMF. We see that the MPMF extracts many weak, thin neovascular vessels, which cannot be detected by the other three schemes. To allow a better view, we cropped and zoomed-in part of the images, as in Figure 3.12. It can be clearly seen that the abnormal fine. Neovascular structures could be effectively detected by using MPMF. Figure 3.13 and 14 show another example of PDR.

[2] The images were collected from the patients in the Ophthalmologic Department, the First Affiliated Hospital of Henan Medical College, Henan Province, China.

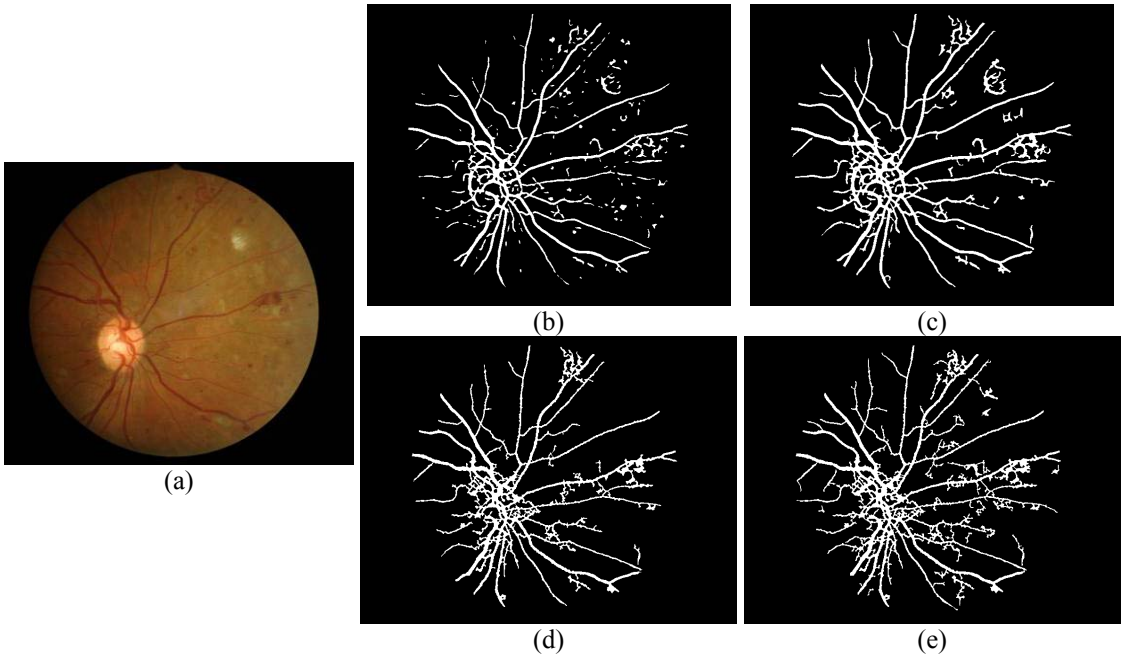

Figure 3.11. (a) An original PDR image; the extracted vessel images using schemes (b) [3]; (c) [20]; (d) the max rule with post-processing; and (e) the proposed MPMF with post-processing.

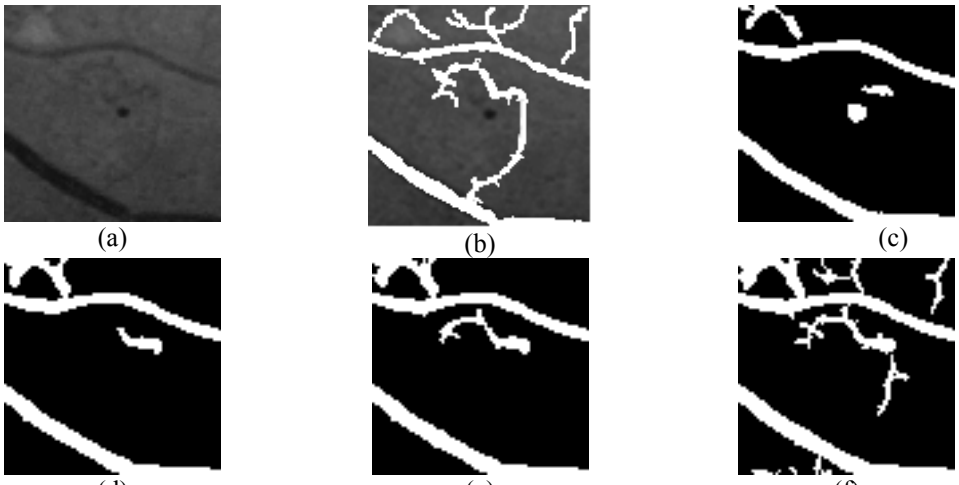

Figure 3.12. Zoom-in images of Figure 3.11. (a) Original image; (b) manually segmented image; (b) method [3]; (d) method [20]; (e) the max rule; and (f) the proposed MPMF.

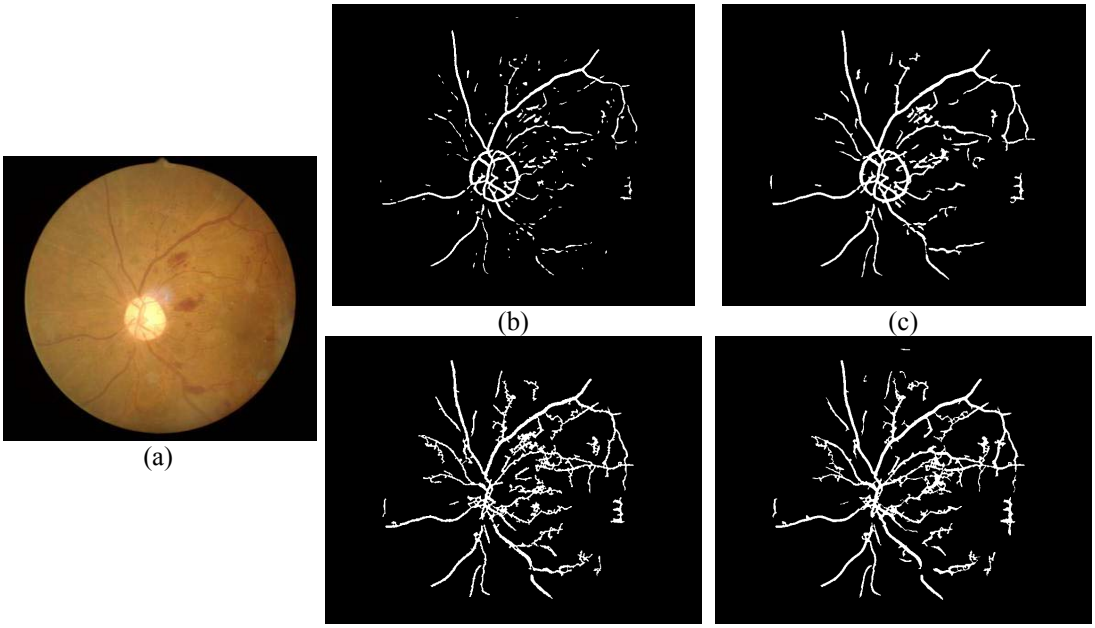

Figure 3.13. (a) An original PDR image; the extracted vessel images using schemes (b) [3]; (c) [20]; (d) the max rule with post-processing; and (e) the proposed MPMF with post-processing.

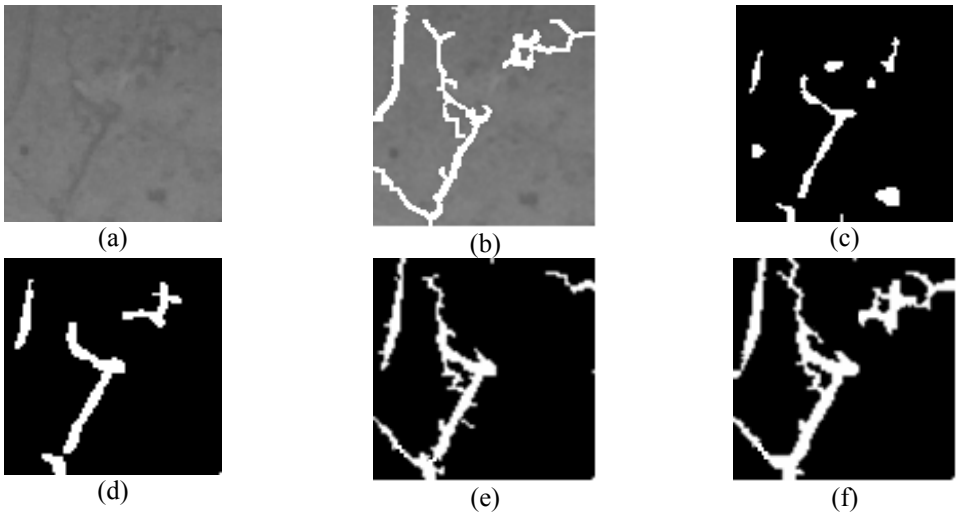

Figure 3.14. Zoom-in images of Figure 3.13. (a) Original image; (b) manually segmented image; (b) method [3]; (d) method [20]; (e) the max rule; and (f) the proposed MPMF.

3.1.3.2. Experiments on STARE and DRIVE databases

In this section we test the proposed automated vessel segmentation method on the open STARE and DRIVE databases. The STARE database consists of retinal images captured with a TopCon TRV-50 fundus camera at 35° FOV, which were digitized at 24-bits and a spatial resolution of 700×605 pixels. We used a total of 20 images, ten

from healthy ocular fundi and ten from unhealthy fundi. The database also provides hand-labeled images as the ground truth for vessel segmentation so that the algorithms can be evaluated for comparison. The DRIVE databases consists of 40 images captured with a Canon CR5 camera at 45° FOV, which were digitized at 24-bits with a spatial resolution of 565×584 pixels. Seven of the images are pathological. Hand-labeled images are also available in this database.

It is not possible to make a valid comparison of the four methods in question here by simply directly matching the segmented vessel map with the ground-truth. This is because large vessels are both easier to detect and make up most of the white pixels in the ground truth and some methods may be better at the task of identifying large vessels but not small vessels. So, in order to create a task in which the methods must be able to detect both large and small vessels, we carried out the matching only after thinning the segmented and ground truth images. We then calculated the sensitivity against predictive value [46], which is defined as following.

The same vessel may not be matched in the precision of one pixel after thinning. Thus, we dilate the thinned images for matching, which means that the true positives (TP), vessel pixels correctly classified, are defined as

$$TP = \#\left[S\left(\delta^{B}(v_m) \wedge v_c\right)\right] \tag{3.9}$$

where # means "the number of", $S(f)$ is the support of f, $\delta^{B}(f)$ means dilating f using structure element B, $\wedge$ is the logical "and" operation, v_m is the manually segmented vessel, and v_c is the automated segmentation result. Here we set B as a disc with 1 pixel radius. The false positives (FP), background pixels classified as vessel pixels, and false negatives (FN), vessel pixels classified as background pixels, are defined as [46]

$$FP = \#\left[S(v_c) \setminus S\left(\delta^B(v_m) \wedge v_c\right)\right] \tag{3.10}$$

$$FN = \#\left[S(v_m) \setminus S\left(v_m \wedge \delta^B(v_c)\right)\right] \tag{3.11}$$

where \ is the set difference. In the thinned images, the FP will be always very small. We plot sensitivity against predictive value to evaluate the performance. The sensitivity and predictive value [46] are defined as

$$sensitivity = \frac{TP}{TP + FN} \tag{3.12}$$

$$predictive\ value = \frac{TP}{TP + FP} \tag{3.13}$$

The sensitivity is the rate of correctly classified vessel pixels. The predictive value is the probability that a pixel that has been classified as a vessel really is a vessel. We compare MPMF with single scale matched filter [3] and multiscale matched filters fusing by maximum rule. All of these three kinds of filter responses are thresholded by double-thresholding without any postprocessing so that we can clearly see the improvements to be had from different fusion strategies.

The 10 normal images in STARE database and the ground truth generated by the second human expert (labels-vk) are used to plot the sensitivity against predictive value shown in Figure 3.15 (a). The 16 normal images in DRIVE database and the ground truth generated by the second human expert (2nd_manual) are used to plot the sensitivity against predictive value shown in Figure 3.15 (b). The different values of sensitivity and predictive values are generated by varying the value of t_1. (Scale production is a strategy to improve signal-to-noise ratio but the matched filter produce high responses to lesions. Therefore we only use normal images in this experiment to demonstrate the efficiency of scale production.)

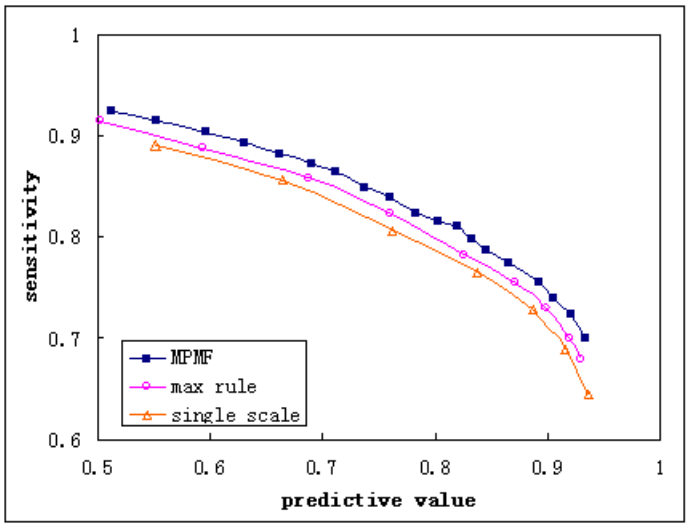

(a)

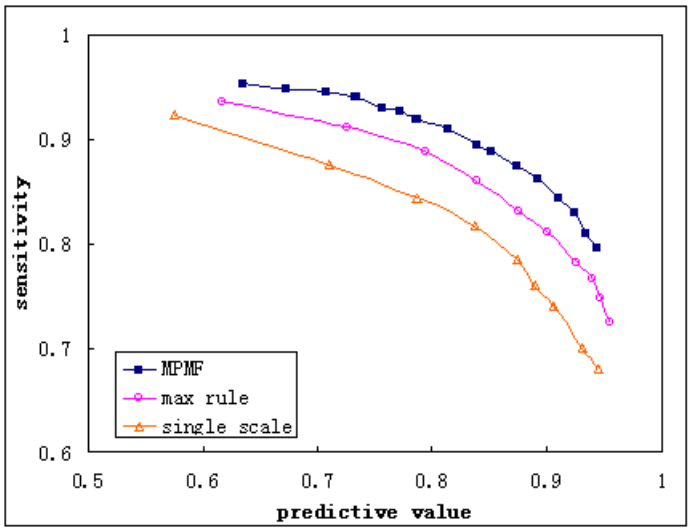

(b)

Figure 3.15. Sensitivity vs. predictive value. (a) STARE database; (b) DRIVE database.

Tables 3.1-3.3 compare our method (MPMF plus postprocessing) with the state-of-the-art schemes [9][16][20] [23][33] by using three performance measures (1) detection accuracy, and the corresponding (2) true positive rate (TPR) and (3) false positive rate (FPR) at that accuracy. The detection accuracy is defined as the ratio of the total number of correctly classified pixels (the vessel pixels classified as vessel pixels and the non-vessel pixels classified as non-vessel pixels) to the number of pixels inside FOV. The TPR is defined as the ratio of the number of correctly classified vessel pixels to the number of total vessel pixels in the ground truth. The FPR is defined as the ratio of the number of non-vessel pixels inside FOV but

classified as vessel pixels to the number of non-vessel pixels inside FOV in the ground truth.

Table 3.1 presents the performance of our method on the STARE database. The performance measures of Staal [9], Mendonça [23], and Martínez-Pérez [34] were obtained from their papers. The performance measures of Soares *et al.* [16] and Hoover *et al.* [20] were calculated using the segmented images obtained from their websites. The FOV used for STARE database is generated using the code provided by Soares *et al.* [16]. All 20 images are used for the experiment. The images hand-labeled by the first human expert (labels-ah) are used as ground truth.

Table 3.2 presents the performance of our method for DRIVE database. The performance measures of Staal *et al.* [9] and Soares *et al.* [16] were calculated using the segmented images obtained from their websites. The performance measures of Mendonça *et al.* [23] and Martínez-Pérez *et al.* [34] were obtained from their papers. The DRIVE database provides FOV. All 20 images in the test set are used for the experiment. The images hand-labeled by the first human expert (2nd_manual) are used as ground truth.

Table 3.3 presents the different performances of our method for normal and abnormal images in STARE database. The performance measures of Soares *et al.* [16] and Hoover *et al.* [20] were calculated using the segmented images obtained from their websites. The performance measure of Mendonça *et al.* [23] was obtained from that paper.

From Tables 3.1-3, we can see that the proposed MPMF method is competitive with those state-of-the-art methods. It achieves very high TPR, especially for the normal retinal images. The MPMF achieves the best results for retinal images without bright lesions. The performance of MPMF become lower when bright

lesions exist but it is still competitive. It should be noted that the proposed MPMF method is much easier to implement and has much lower complexity than the snake and tracking based classification methods [20][25]--[31] and the supervised methods [9][16]. This makes the building of a real-time system possible. The execution time for processing one retinal image is around 20 seconds (Matlab programming environment without optimization, Pentium III 1.0 GHz CPU, and 512 MB memory).

Table 3.1 Extraction Results for 20 Images in STARE Database

Method	Accuracy	TPR	FPR
2nd Human observer	0.9354	0.8949	0.0610
Hoover	0.9267	0.6751	0.0433
Staal	0.9516	0.6970	0.0190
Soares	0.9485	0.7211	0.0235
Mendonça	0.9479	0.7123	0.0242
Martínez-Pérez	0.9410	0.7506	0.0431
MPMF	**0.9436**	**0.7390**	**0.0289**

Table 3.2 Extraction Results for 20 Images (Test Set) in DRIVE Database

Method	Accuracy	TPR	FPR
2nd Human observer	0.9473	0.7761	0.0275
Staal	0.9442	0.7194	0.0227
Soares	0.9466	0.7283	0.0212
Mendonça	0.9463	0.7315	0.0219
Martínez-Pérez	0.9344	0.7246	0.0345
MPMF	**0.9396**	**0.7368**	**0.0262**

Table 3.3 Extraction Results for 20 Images in STARE Database (Normal versus Abnormal Cases)

Method	Accuracy	TPR	FPR
Normal cases			
2nd Human observer	0.9283	0.9646	0.0764
Hoover	0.9324	0.6766	0.0338
Soares	0.9467	0.7325	0.0261
Mendonça	0.9531	0.7366	0.0178

MPMF	**0.9546**	**0.8130**	**0.0263**
	Abnormal cases		
2nd Human observer	0.9425	0.8252	0.0456
Hoover	0.9211	0.6736	0.0528
Soares	0.9504	0.7096	0.0206
Mendonça	0.9426	0.6801	0.0306
MPMF	**0.9327**	**0. 6650**	**0. 0314**

Figure 3.16-17 show the vessel segmentation results on two retinal images (im0077, and im0255) in the STARE database using the four schemes: [20], [16], the max rule and the proposed MPMF. The segmented results of [20] and [16] were obtained from their websites. We varied the threshold to achieve the greatest sensitivity at the smallest cost of accuracy. The proposed MPMF achieves the highest sensitivity at accuracy similar to other schemes. It can be seen that the matched filter scheme in [20] misses many thin vessels; the multiscale scheme with the max rule extracts some thin vessels but also introduces some false vessels due to noise; the proposed MPMF scheme can find many weak and thin vessels which cannot be found by the other three schemes. It also does a good job of suppressing false vessels caused by background noise.

To provide a better view on the results of the proposed scheme, we cropped several parts of the images in Figures 3.16-17 and zoomed-in in Figure 3.18. The first row shows the original cropped images; the second row shows their corresponding ground truth vessel maps; the third row shows the vessel extraction results when using the matched filter scheme in [20]; the fourth row shows the results using Soares' supervised method [16]; the fifth row shows the results by using the Max rule over three scales; the bottom row shows the results of MPMF. We see that MPMF scheme can extract both thin and wide vessels simultaneously. The low contrast weak vessel can also be extracted from the noisy background using MPMF. In addition, MPMF can also preserve better vessel width information.

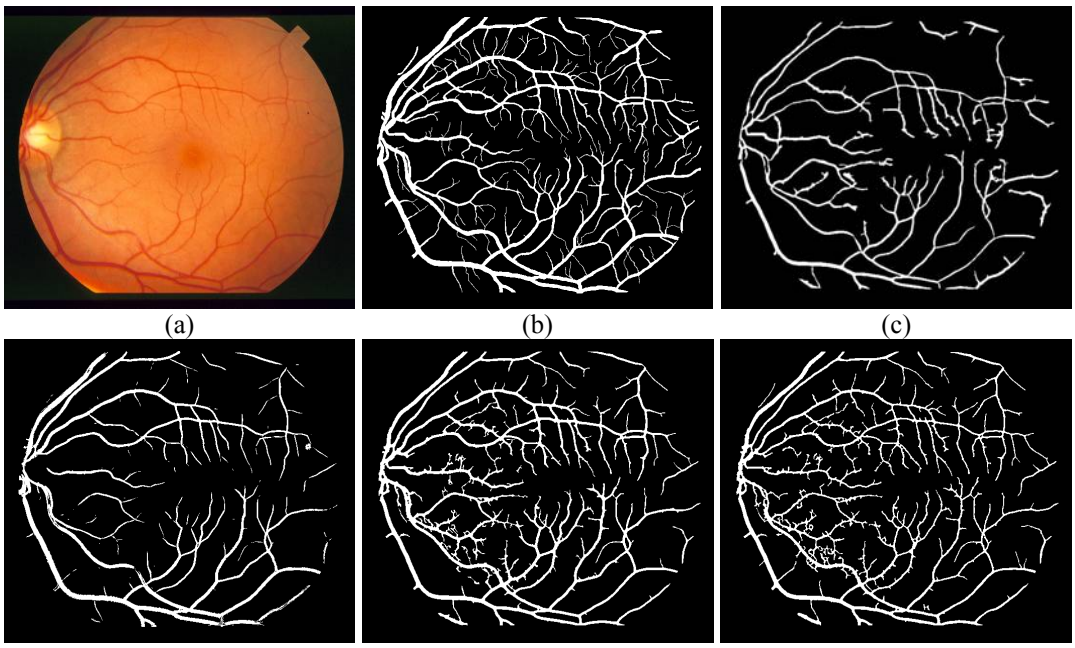

Figure 3.16. (a) The original image im0077 in the STARE database; (b) the ground truth vessel map; the extraction results by (c) Hoover [20], Accuracy = 0.8984, Sensitivity = 0.5652, Predictive = 0.9399; (d) Sores [16], Accuracy = 0.9282, Sensitivity = 0.5917, Predictive = 0.9410; (e) the max rule, Accuracy = 0.9272, Sensitivity = 0.7259, Predictive = 0.8972; and (f) the proposed MPMF, Accuracy = 0.9229, Sensitivity = 0.7482, Predictive = 0.9069.

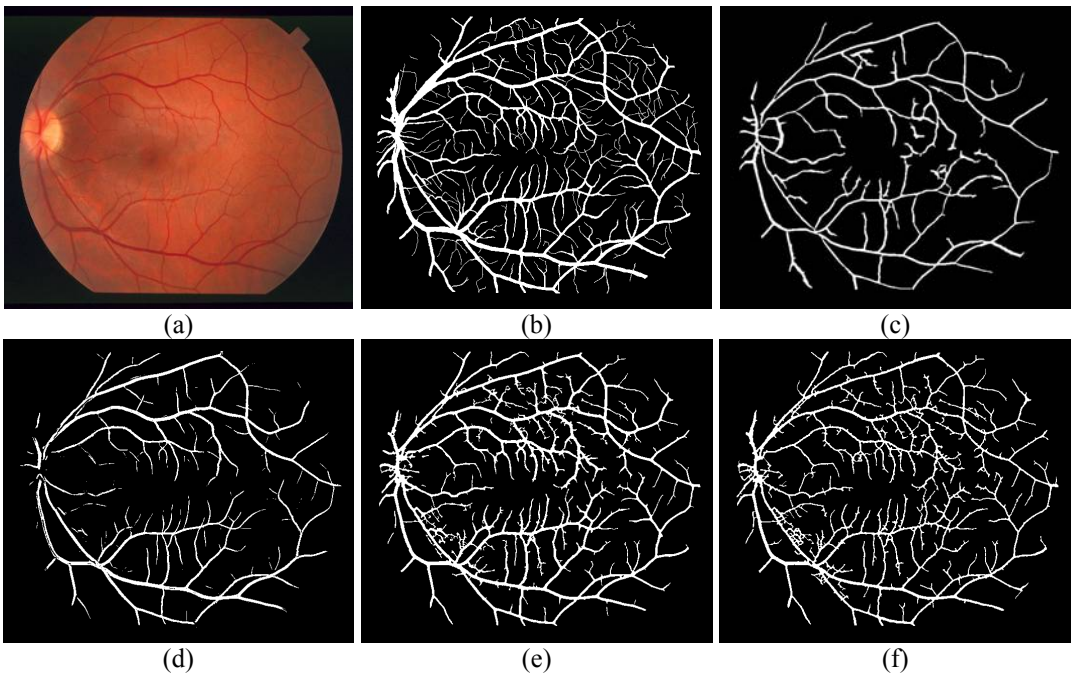

Figure 3.17. (a) The original image im0255 in the STARE database; (b) the ground truth vessel map; the extraction results by (c) Hoover [20], Accuracy = 0.8932, Sensitivity = 0.4664, Predictive = 0.9322; (d) Sores [16], Accuracy = 0.9117, Sensitivity = 0.5144, Predictive = 0.9461; (e) the max rule, Accuracy = 0.9218, Sensitivity = 0.6957, Predictive = 0.8991; and (f) the proposed MPMF, Accuracy = 0.9204, Sensitivity = 0.7169, Predictive = 0.9060.

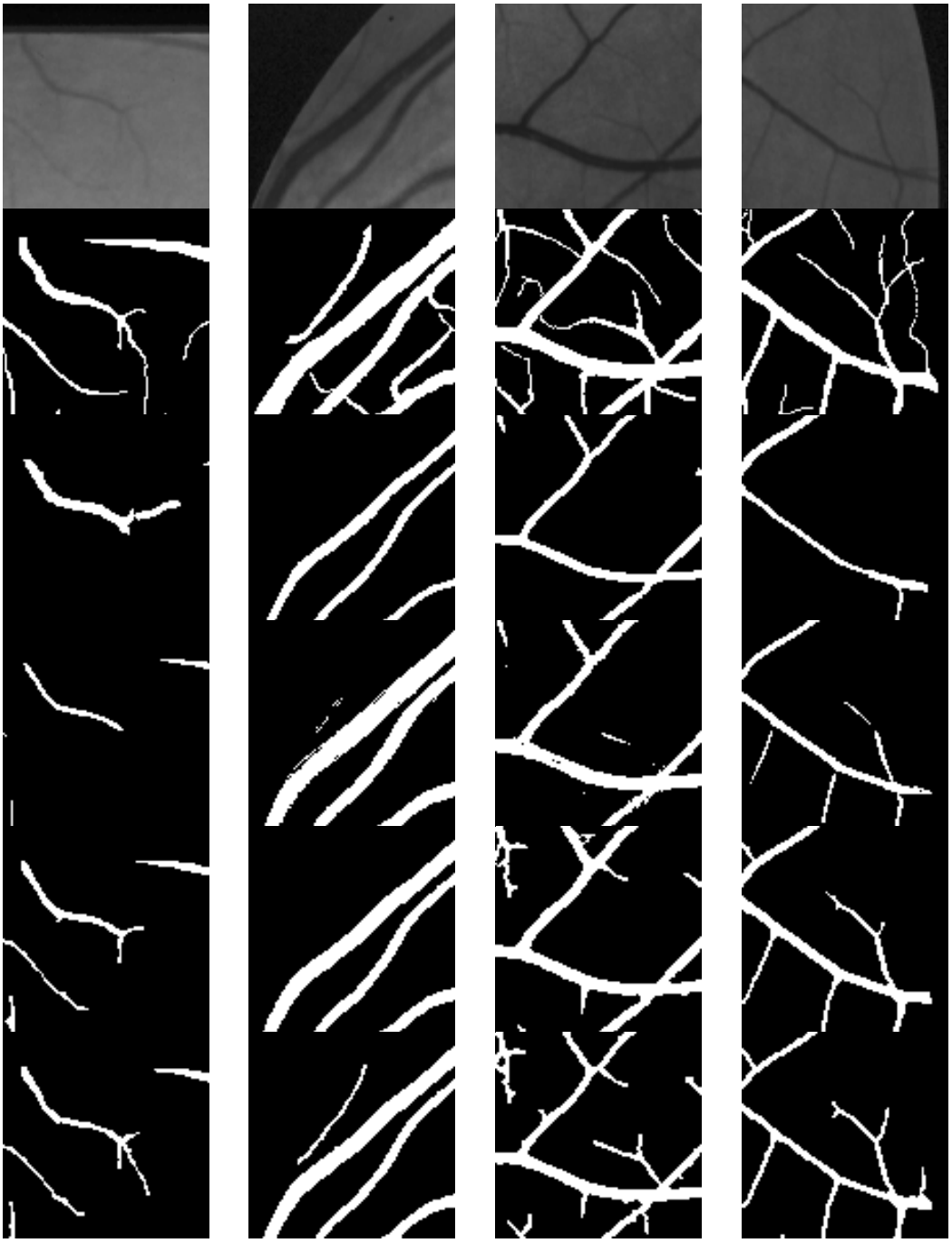

Figure 3.18. Zoom-in subimages in Figures 16-17. The first row shows some cropped blocks from the original images; the second row shows their corresponding ground truth vessel maps; the third row shows the vessel extraction results using method by Hoover [20]; the fourth row shows the results using method by Soares [16]; the fifth row shows the results using the multiscale max rule; and the sixth row shows the results using the proposed MPMF method.

Figures 3.19-20 show the vessel segmentation results on two retinal images (01_test, and 02_test) in the DRIVE database using four schemes: [9], [16] the max rule and the proposed MPMF. The segmented results of [9] and [16] were obtained from their websites. The cropped and zoomed-in images of Figures 3.19-20 are shown in Figure 3.20.

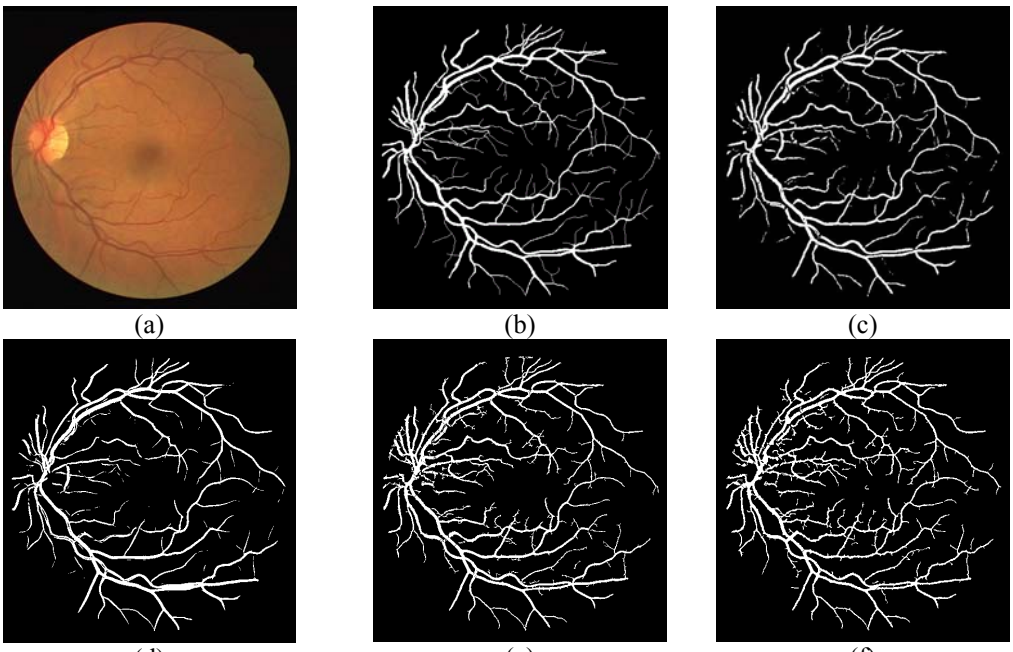

Figure 3.19. (a) The original image 01_test in the DRIVE database; (b) the ground truth vessel map; the extraction results by (c) Staal [9], Accuracy = 0. 9495, Sensitivity = 0. 8143, Predictive = 0. 9696; (d) Sores [16], Accuracy = 0. 9495, Sensitivity = 0. 7939, Predictive = 0. 9542; (e) the max rule, Accuracy = 0. 9441, Sensitivity = 0. 8601, Predictive = 0. 8681; and (f) the proposed MPMF, Accuracy = 0. 9406, Sensitivity = 0. 8806, Predictive = 0. 8649.

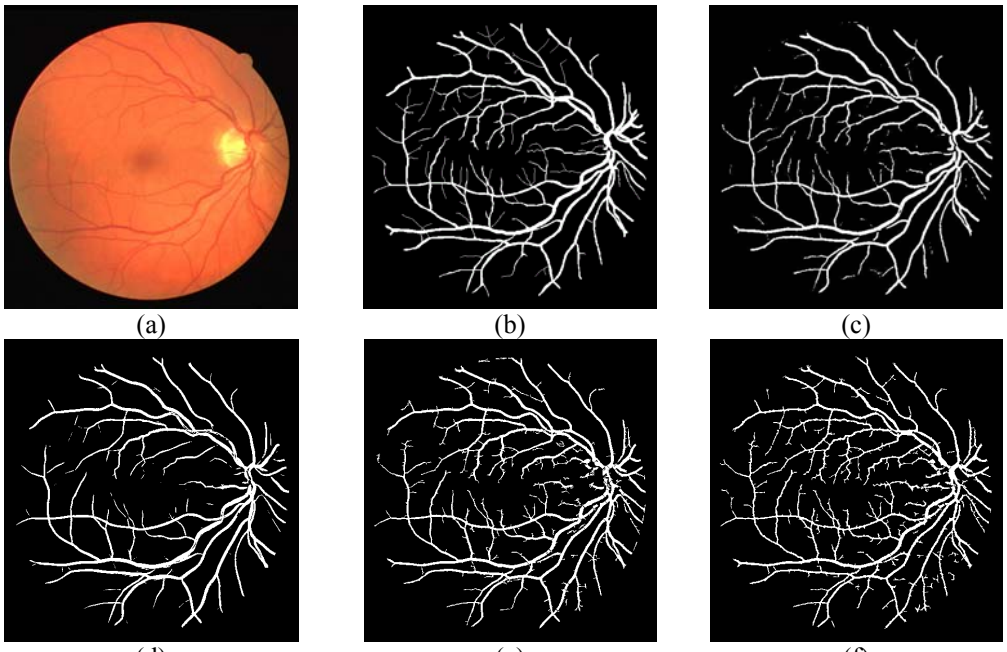

Figure 3.20. (a) The original image 02_test in DRIVE database; (b) the ground truth vessel map; the extraction results by (c) Staal [9], Accuracy = 0. 9564, Sensitivity = 0. 8273, Predictive = 0. 9678; (d) Soares [16], Accuracy = 0.9529, Sensitivity = 0. 7777, Predictive = 0. 9582; (e) the max rule, Accuracy = 0. 9467, Sensitivity = 0. 8618, Predictive = 0. 8450; and (f) the proposed MPMF, Accuracy = 0. 9426, Sensitivity = 0.9025, Predictive = 0.8622.

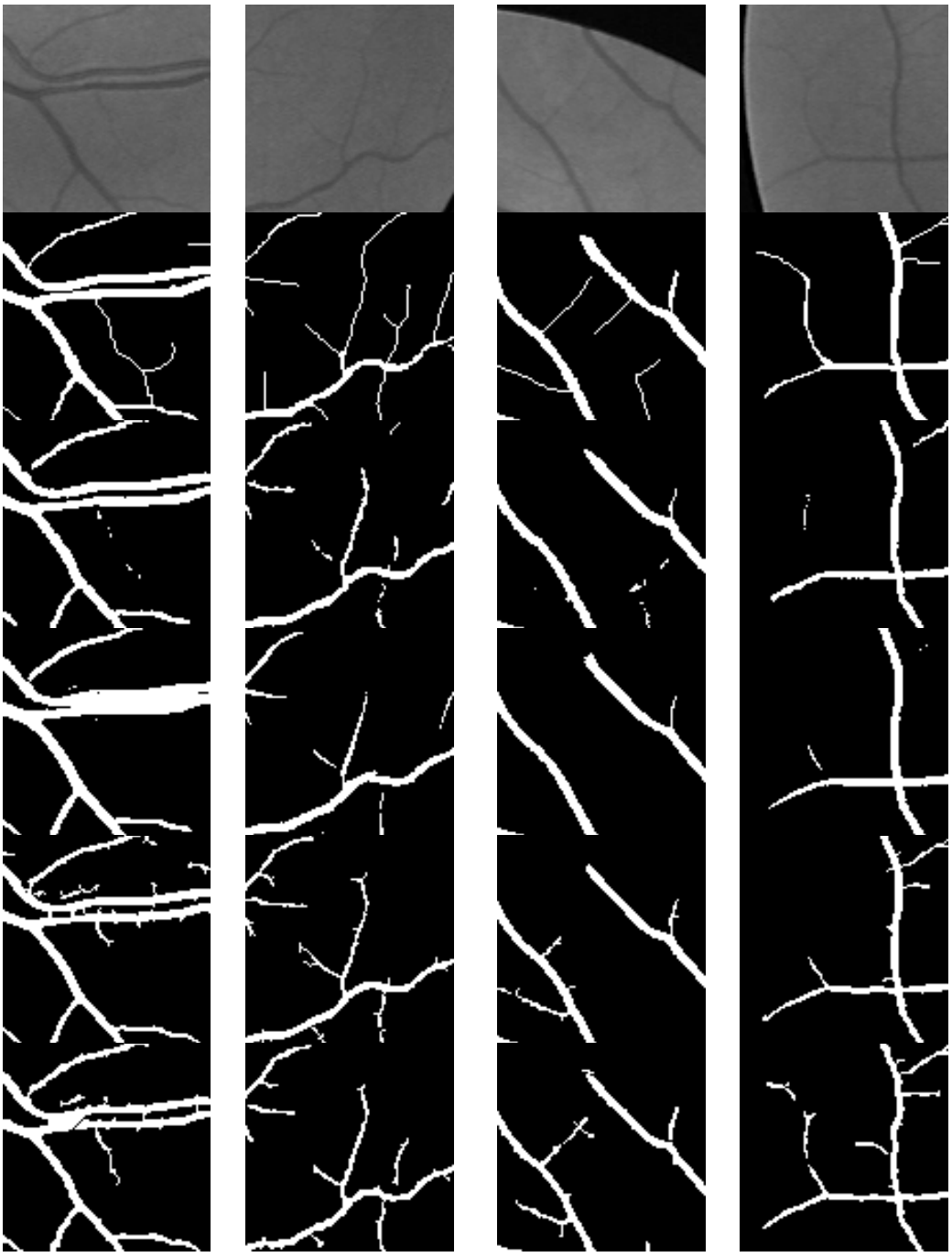

Figure 3.21. Zoom-in subimages in Figures 19-20. The first row shows some cropped blocks from the original images; the second row shows their corresponding ground truth vessel maps; the third row shows the vessel extraction results using method by Staal [9]; the fourth row shows the results using method in [16]; the fifth row shows the results using the multiscale max rule; and the sixth row shows the results using the proposed MPMF method.

3.2 Segmentation of Retinal Vessels Using MMFDST

The importance and effectiveness of using retinal vessels in screening Diabetic Retinopathy (DR) have been reported in [9][16]. As a serious stage of DR, Proliferative Diabetic Retinopathy (PDR) is a common complication of diabetes that damages the eye's retina and an early diagnosis of PDR is critical to protecting patients' vision. The appearance of neovascular (new vessel growth) stands for PDR [11][12]. The false positives of vessels will distort the diagnosis a lot. In this section, we will describe a retinal vessel segmentation scheme using Modified Matched Filter and Double Site Thresholding (MMFDST), which can suppress the false positives efficiently.

By now, many retinal vessel extraction methods have been proposed [9]--[40] yet neovascular extraction is still a difficult problem in terms of accuracy. The matched filter proposed in [3] is a line detector for finding valleys in an image and is one of the most successful retinal vessel extraction methods. It employs the prior information that the cross-section of a retrial vessel is Gaussian-shaped; therefore, a Gaussian filter can be used to "match" the vessel. However, like other line detectors such as the second derivative of Gaussian [59] and Gabor filters [16] [22][60], the matched filters respond not only to vessels but also to non-vessel edges. For example, if we need to find the dark lines in an image, the edges of bright blobs will be the major false detections for line detection, which is a curse for all band-pass filters. Consequently, some blobs (bright lesions and the optic disc) in the retinal image may cause false detection of vessels. If there are several lesions tangled together, they may be detected as a neovascular net and hence lead to a false diagnosis of PDR.

The post-processing technique that we proposed in Section 3.1.2.4 can deal with this but it is not easy to implement and may give rise to false negatives to vessel

segmentation. In [23], a vessel detection scheme was proposed that used the first derivative of Gaussian and a modified top-hat operation. The use of the first derivative of Gaussian can suppress the false detections caused by bright blobs. But the preprocessing of small line enhancement and the later morphological reconstruction will produce more false detections. In [35], Lam and Yan proposed a technique based on Gradient Vector Field (GVF) [118][119][120]. Their technique works well for avoiding false positives in pathological images. But their technique is very time consuming and cannot describe very well the boundary and width of vasculature, which is important information for neovasculars.

In this section, we propose a modified matched filter that suppresses the false detections caused by bright blobs. Instead of subtracting the local mean from the response for removing background and then thresholding to detect vessels as in the traditional matched filter, we first enhance the retinal image by using Gaussian filters and then analyze the local structures of filtering outputs by a double-side thresholding operation. The proposed modified matched filter could avoid responding to non-line edges, which would significantly reduce the false detection of vessels.

The rest of this section is organized as follows. Section 3.2.1 analyzes the problems in vessel segmentation in pathological images. Section 3.2.2 defines our MMFDST scheme. And the experimental results are given in section 3.1.3 to evaluate the performance of our MMFDST scheme.

3.2.1. Problems with Using the Matched Filter on Pathological Images

The fact that the cross-section of the vessels in a retinal image has the shape of a Gaussian function means that a Gaussian-shaped filter can be used to “match” the

vessels, to which strong filtering responses are expected. Mathematically, the matched filter can be described as in Equation 3.1 and 3.2.

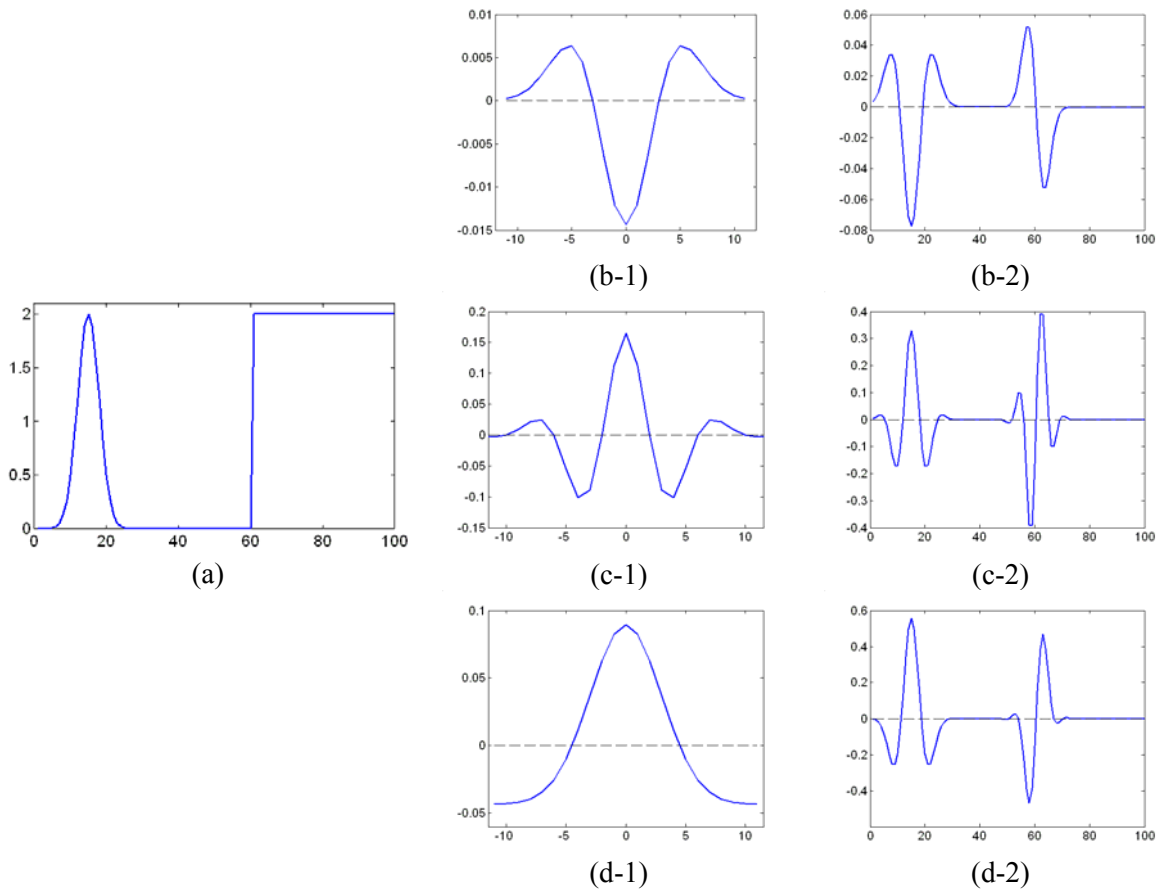

Figure 3.22. Responses of different line detectors to a Gaussian line cross-section and an ideal step edge. (a) a Gaussian line cross-section and an ideal step edge; (b-1) the second order derivative of Gaussian and (b-2) its filter response; (c-1) Gabor filter and (c-2) its filter response; (d-1) matched filter and (d-2) its filter response.

One major problem of the matched filter is that it responds not only to lines but also non-line edges. This problem also exists in other line detectors such as the Gabor filter and the second order derivative of a Gaussian function. Figure 3.22 illustrates this by showing the responses of different filters to a Gaussian function (i.e. the cross-section of a vessel) and an ideal step edge. We can see that all three filters have strong responses to both the line cross-section and the non-line ideal step edge. Figure 3.23 shows the response image of the matched filter to a retinal image. Therefore, in pathological images, the strong responses to the vessels are clear, as

well as the edges of the bright lesions. After thresholding, both the vessels and the edges of lesions will be detected.

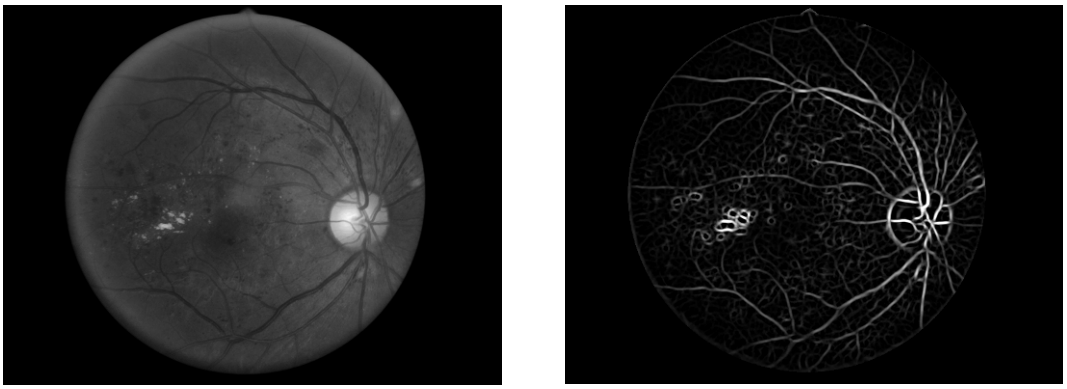

(a) (b)

Figure 3.23. (a) A retinal image with NPDR; (b) the matched filter response to the image in (a).

3.2.2 Modified Matched Filter with Double-Side Thresholding

Our Modified Matched Filter with Double-Site Thresholding is defined in this section.

3.2.2.1 Modified Matched Filter

In the definition of matched filter in Equation 3.1, the mean value m is subtracted from the Gaussian function to remove the smooth background in the filtering output. Then a thresholding operation can be used to detect the vessel pixels. However, as we have seen in Section 3.2.1 shown in Figure 3.23, the matched filter will also give strong response to non-vessel edge structures (bright lesions, dark lesions) and the thresholding cannot distinguish them well from the vessel structures. In this section, we present a new scheme to solve this problem. We don't subtract the mean from the Gaussian filter and modify the matched filter in Equation 3.1 as

$$g(x,y) = \exp\left(-x^2/\sigma^2\right), \quad \text{for } |x| \le 3\sigma, \quad |y| \le L/2 \tag{3.14}$$

This 2D modified matched filter in Equation 3.14 is a truncated Gaussian function in x direction and the Gaussian function repeats in y direction. Figures 3.24 (a) and (b) show the 1D cross-section of the filter and the 2D filter along 4 different directions.

Figures 3.24 (c) and (d) show a 1D noisy signal, which contains a Gaussian function and a step edge, and its filtering response.

For the convenience of analysis, the modified matched filter will be applied to the complement of the original retinal image, in which the vessels are brighter than the background. The image will be filtered by $g(x,y)$ along 8 directions. Each of the 8 filtering responses will be thresholded to generate a vessel map. Finally the 8 vessels maps are fused through a logical 'OR' operation. Next we introduce the proposed thresholding strategy.

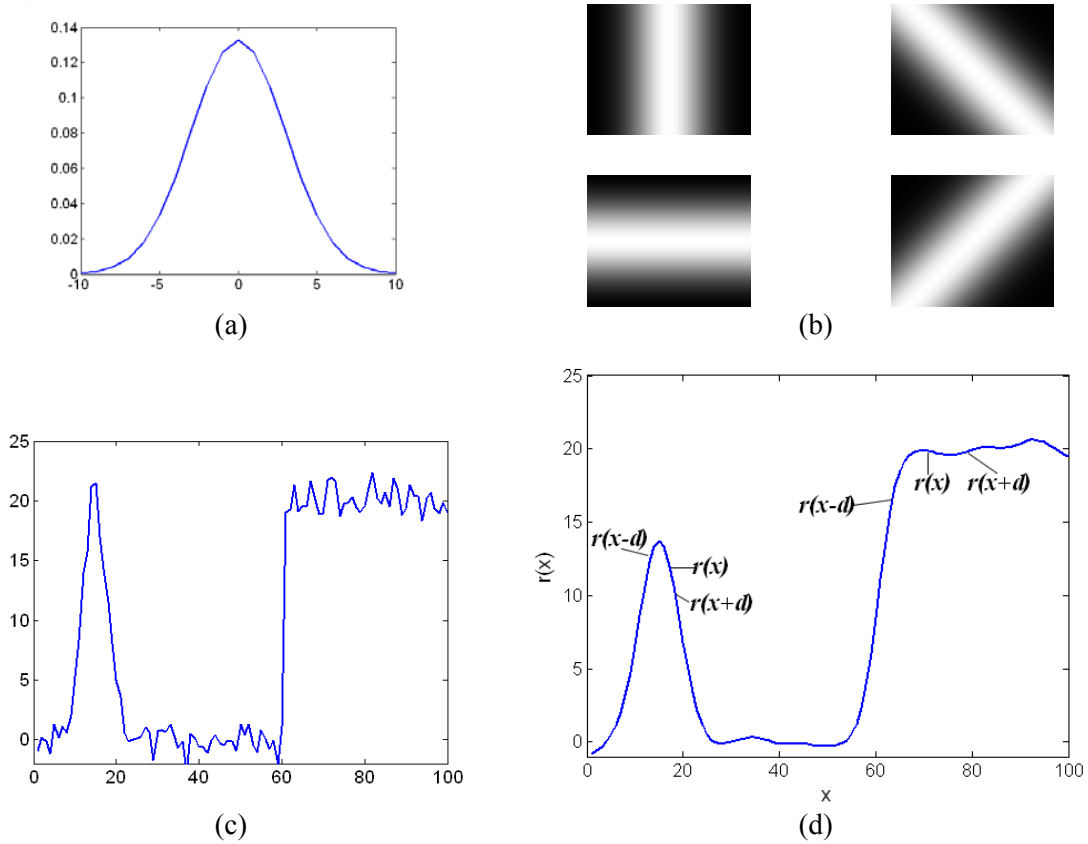

Figure 3.24. The modified matched filter in 1D (a) and 2D (b); (c) a Gaussian function and a step edge with noise; (d) the modified matched filter's response to the signal in (c).

3.2.2.2 Double-Site Thresholding

After image enhancement by using the modified matched filters, the pixels must be classified as either vessel or non-vessel pixels. To classify pixels with suppressing the false positives of vessels, we propose here a local double-side thresholding

scheme to segment the retinal image. To simplify the analysis of filter responses for thresholding, we consider the 1D case, i.e. a 1D signal $f(x)$ is convolved with the 1D matched filter $g(x)$. Referring to Figure 3.24 (d), we can see that if $r(x)$ is the peak point of a Gaussian shaped cross-section of a vessel, it should be greater than both its left and right neighboring points. If $r(x)$ is from the non-vessel edges, it will not be much greater than its neighbors in both sides. Based on this observation, the vessels and non-vessel edges can be distinguished.

Taking this into account, we define that a point $r(x)$ is a vessel point if it is greater than its neighbors $r(x-d)$ and $r(x+d)$ with a threshold T. Mathematically, there is:

$$\begin{cases} r(x)-r(x-d)>T \\ r(x)-r(x+d)>T \end{cases} \tag{3.15}$$

where d is a parameter concerning the width of the vessel to be detected and T is a threshold to evaluate the vessel points.

Obviously, one key issue in Equation 3.15 is the determination of parameters d and T. These two parameters are not independent. We use a matched filter $g(x)$ with standard deviation (std) σ to detect the vessels whose Gaussian-shaped cross-sections have std around σ. Thus we can set

$$d = c_d \cdot \sigma \tag{3.16}$$

where c_d is a constant. In this work, we set it about 2.

Suppose the std of the Gaussian-shaped vessel cross-section $f(x)$ to be detected by $g(x)$ is also σ, the filtering output $r(x)$ will still be a Gaussian function, and its std will be $\sigma_r = \sqrt{\sigma^2+\sigma^2} = \sqrt{2}\sigma$. Denote by x_0 the peak point of $r(x)$. It can be easily calculated that

$$r(x_0)-r(x_0-d)=r(x_0)-r(x_0+d)$$
$$=\frac{1}{\sqrt{2\pi}\sigma_r}\left(1-\exp(-\frac{d^2}{2\sigma_r^2})\right)=\frac{1}{2\sqrt{\pi}\sigma}\left(1-\exp(-\frac{d^2}{4\sigma^2})\right) \quad (3.17)$$

Denoting $\Gamma=\frac{1}{2\sqrt{\pi}\sigma}\left(1-\exp(-\frac{d^2}{4\sigma^2})\right)$, for a point x_1 in the neighborhood of x_0, we can see that $r(x_1)-r(x_1-d)<\Gamma$ and $r(x_1)-r(x_1+d)<\Gamma$. Thus to detect point x_0 and its neighbors, which are considered as vessel points, we set the threshold T in Equation 3.15 as

$$T=c_T\cdot\Gamma \quad (3.18)$$

where c_T is a constant and $c_T<1$. In this work, we choose $0.5<c_T<0.8$.

One way of producing better segmentation results is to adopt the double-thresholding strategy as in [55]. A low threshold $T_l=c_T\cdot\Gamma$ and a high threshold $T_h=2T_l$ are set and then two vessels maps V_l and V_h are obtained. The final vessel map will be formed by selecting vessels in V_l that link to the vessels in V_h. Another way is to use multiple filters $g(x,y)$ at multiple scales to detect vessels of different widths. For example, we can use two filters, g_1 with std σ_1 and g_2 with std σ_2, to implement the vessel detection procedure described above. This gives us two vessel maps, denoted by V_1 and V_2, which we can fuse using the "OR" logic operation to produce a more robust vessel map.

3.2.2.3 Computational complexity

In this section, we discuss the computational complexity of MMFDST. MMFDST consists of convolution, double side thresholding, and double thresholding. The complexity of these procedures are $O(n)$, $O(n)$, and $O(n\cdot r)$, respectively.

Therefore MMFDST is more efficient than Hoover's method [20] is and Mendonça's method [23].

3.2.3 Experimental Results

This section gives the experimental results of our method. Two databases, ZUEYE and STARE, are used for our experiments. The indices that used to quantitatively measure the performance of different algorithms include: (1) detection accuracy (ACC); (2) the corresponding true positive rate (TPR) and (3) the false positive rate (FPR) at that accuracy. The ACC is defined as the ratio of the total number of correctly classified pixels (the vessel pixels classified as vessel pixels and the non-vessel pixels classified as non-vessel pixels) to the number of pixels inside FOV; the TPR is defined as the ratio of the number of correctly classified vessel pixels to the number of total vessel pixels in the ground truth; the FPR is defined as the ratio of the number of non-vessel pixels inside field of view (FOV) but classified as vessel pixels to the number of non-vessel pixels inside FOV in the ground truth.

3.2.3.1 Evaluation on the ZUEYE database

We evaluated the performance of proposed MMFDST scheme on screening PDR by applying it to the ZUEYE database, which consists of retinal images from DR patients[3]. The color fundus images were captured by using Kowa VK-3 fundus camera at 45^{o} field of view (FOV) and they were stored in 24-bits digital format. The resolution of the images is 800×608. There are 20 retinal images with DR in ZUEYE, including 15 NPDR and 5 PDR. Figure 3.25 and 3.26 present 2 examples of vessel extraction by applying the proposed method to one PDR and one NPDR retinal images in ZUEYE. The improved matched filter developed by Hoover [20] is used

[3] The images were collected from the patients in the Ophthalmologic Department, the First Affiliated Hospital of Zhengzhou University, Henan Province, China. The ground truth maps of vessels were manually labeled by the experts in that hospital.

for comparison. In the experiments, we set $\sigma_1 = 1$ to extract small vessels and $\sigma_2 = 1.7$ to extract large vessels. By varying the values of T_h, different true positive ratios and false positive ratios can be obtained. Table 3.4 lists the most accurate results obtained using the the Hoover's method [20] and our MMFDST.

Figure 3.25 (a) shows an NPDR retinal image. Figure 3.25 (b) is the hand-labeled ground truth of vessel map and Figures 3.25 (c) and (d) show the vessel maps extracted using respectively the Hoover's method [20] and the proposed MMFDST method. We see that the proposed MMFDST method can eliminate most of the false detection of vessels caused by the strong edges of bright lesions. To make this easier to seem, we have cropped and zoomed-in part of the images in Figures 3.25 (e) - (h). Figure 3.26 (a) shows a PDR retinal image, (b) is the hand-labeled ground truth of vessel map, (c) - (d) show the extracted vessel maps using the Hoover's method [20] and the proposed method. We see that the proposed method can detect most of the neovasculars (new vessels) and eliminate most of the false detection of vessels caused by the strong edges of bright lesions. We crop and zoom-in part of the images and show them in Figures 3.26 (e) - (h). It is seen that the false vessels caused by bright lesions (top left) in Figure 3.26 (g) are reduced greatly in Figure 3.26 (h) while the abnormal fine neovascular structures (bottom) being well detected.

Observing Figure 3.25 (d) (NPDR case) and Figure 3.26 (d) (PDR case), it is possible to distinguish PDR from NPDR because the PDR image tends to have more vessels in a local window and the neovasculars tend to have a large curvature [11][12]. As shown in Figure 3.26 (d), most of the neovasculars were extracted by our method and few false vessel detections were produced by our method. However, if we applly Hoover's method as shown at Figure 3.25 (c), we can see that the edges

of lesions could be misclassified as neovasculars because they have large local densities and large curvature.

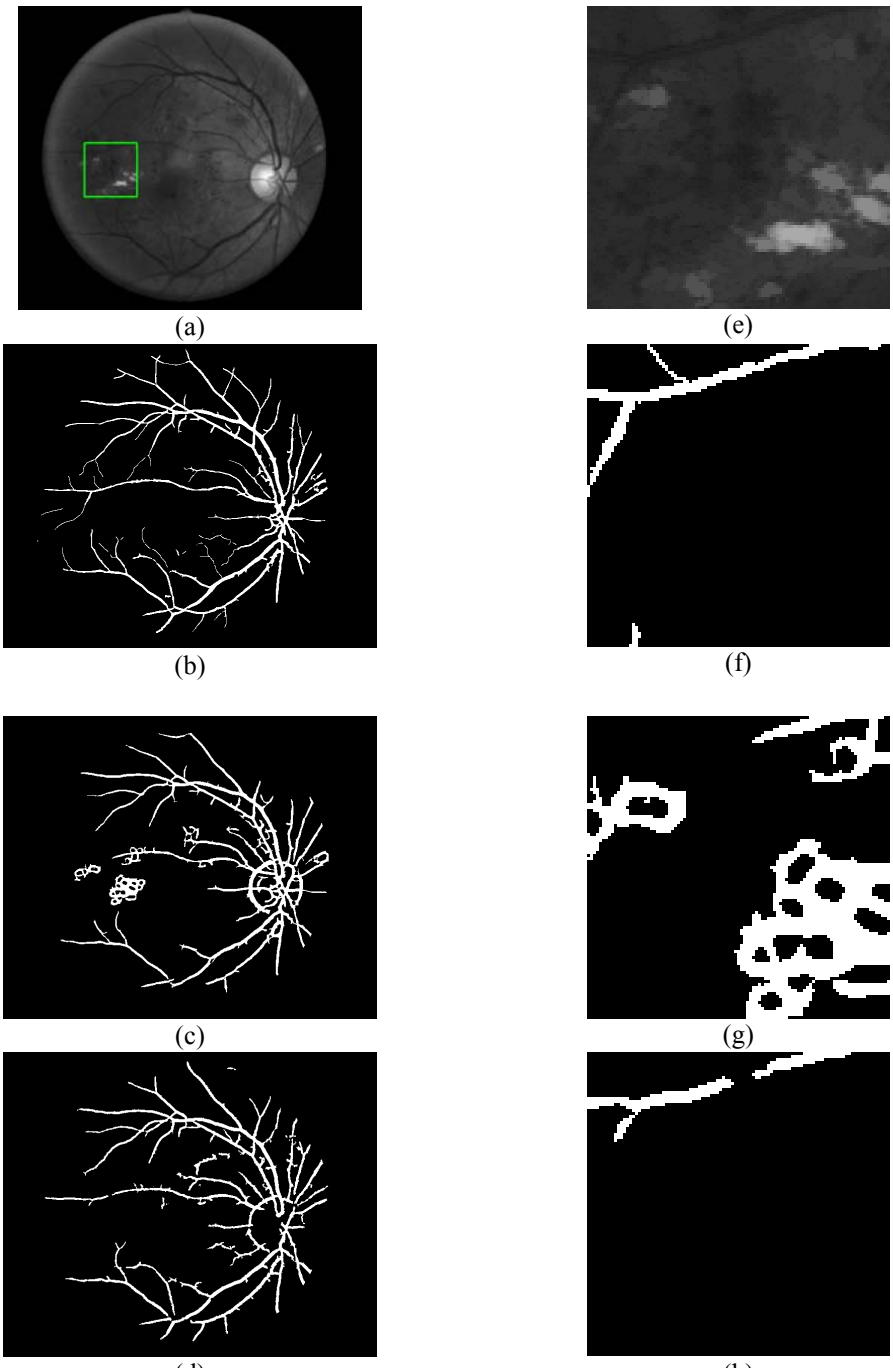

Figure 3.25. (a) An original NPDR image in ZUEYE database; (b) hand-labeled ground truth; (c) the extracted vessel map by the scheme by Hoover [20]: FPR = 0.0373, TPR = 0.7816; ACC = 0.9449; (d) the extracted vessel map by the proposed method: FPR = 0.0320; TPR = 0.7915; ACC = 0.9506; (e) - (h) are zoom-in images of (a) - (d). Note that the false vessel detection caused by strong edges of lesions in (g) is reduced greatly in (h).

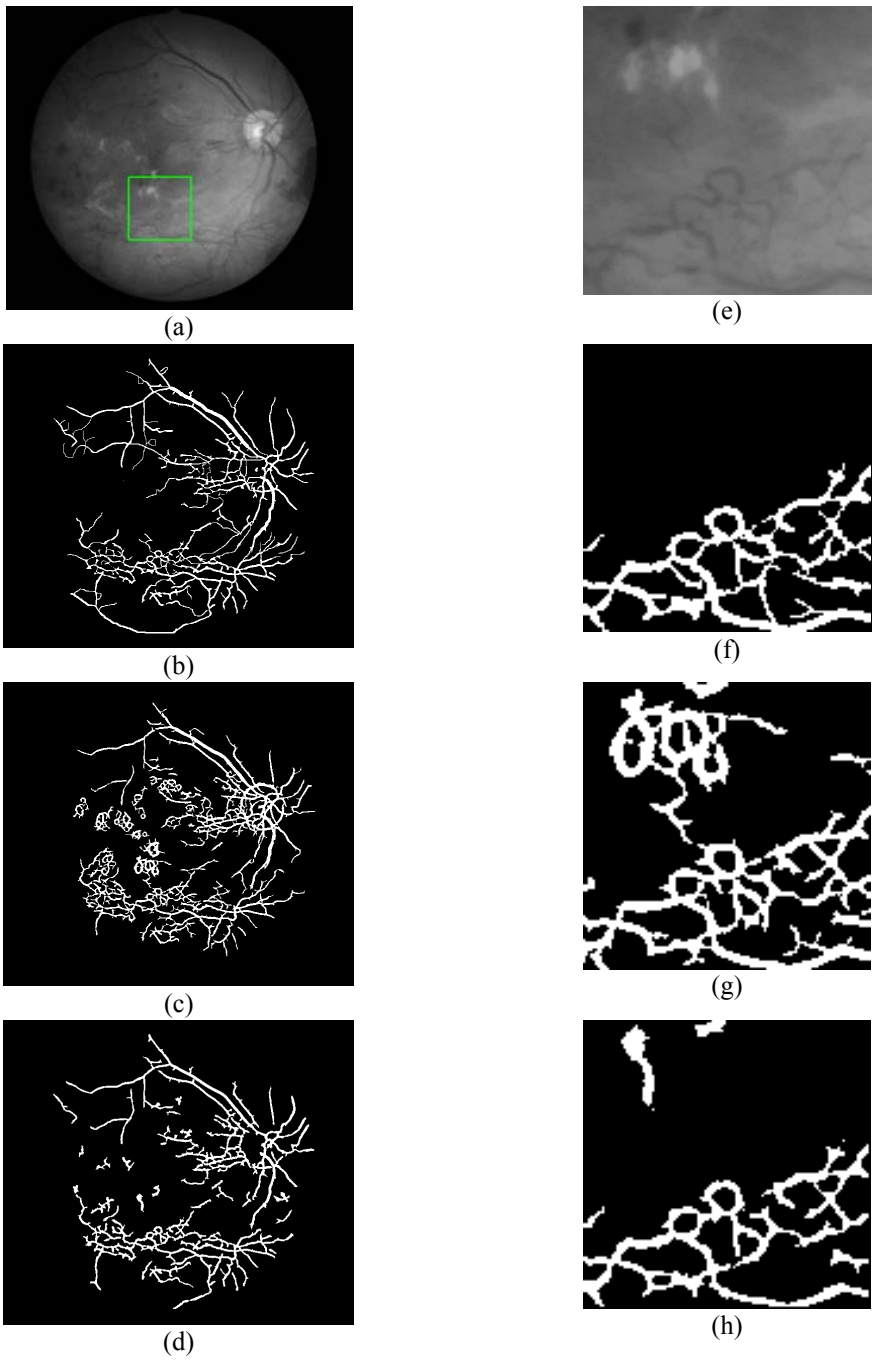

Figure 3.26. (a) An original PDR image in ZUEYE database; (b) hand-labeled ground truth; (c) the extracted vessel map by the scheme by Hoover [20]: FPR = 0.0479, TPR = 0.6754; ACC = 0.9243; (d) the extracted vessel map by the proposed method: FPR = 0.0324, TPR = 0.7959; ACC = 0.9502; (e) - (h) are zoom-in images of (a) - (d). Note that the false vessel detection caused by strong edges of lesions in (e) is reduced greatly in (h) and most of the neovasculars are extracted by the proposed method.

3.2.3.2 Evaluation on the public STARE database

In this section, we tested the ability of the proposed MMFDST scheme to suppress lesions, comparing its performance with the performance of two state-of-the-art schemes, those of Hoover [20] and Mendonça [23][4]. The STARE database consists of retinal images captured by the TopCon TRV-50 fundus camera at 35° FOV, digitized at 24-bits with a spatial resolution of 700×605 pixels. In [20], Hoover selected 20 images for experiments, ten images of healthy ocular fundus and ten images of pathological fundus As ground truth, we used images hand-labeled by the first observer (labels-ah). We set $\sigma_1 = 1$ to extract small vessels and $\sigma_2 = 2$ to extract large vessels. The best averaging accuracies for normal images and pathological images are listed in Table 3.5.

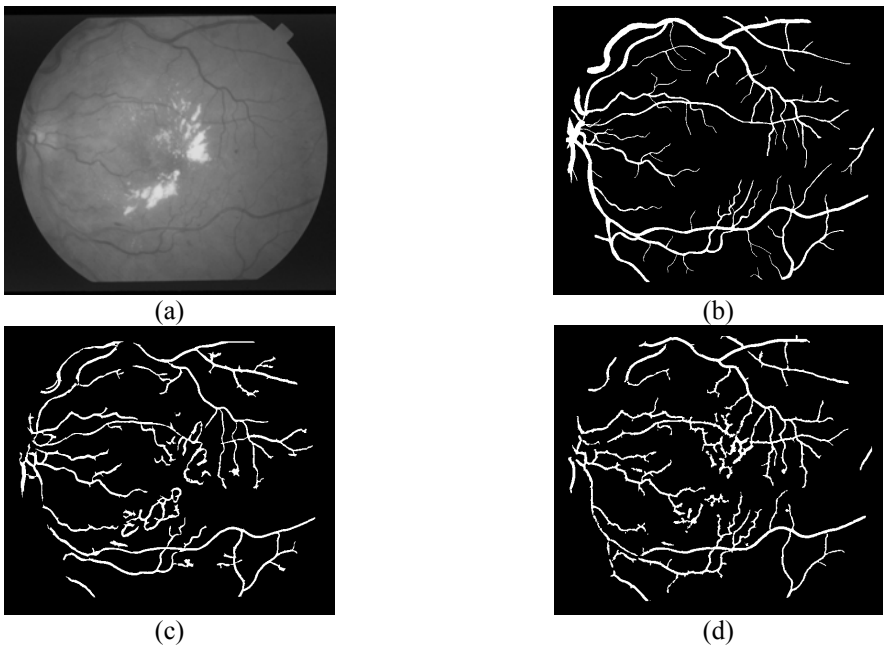

Figure 3.27. (a) An pathological image in the STARE database; (b) the hand-labeled ground truth; (c) the extracted vessel map by the scheme [4]: Accuracy = 0.9198, TPR = 0.5937, FPR = 0.0402; (d) the extracted vessel map by the proposed method: Accuracy =0.9302, TPR = 0.6619, FPR = 0.0368.

[4] The results of [23] in Tables II and III are copied from the original paper. That paper tested different color spaces for vessel extraction and found that the α channel gives best result. We copied that best result for comparison. To comparing with [20] as shown in Figure 3.27 and 3.28 and in Tables 3.V and 3.VI, we downloaded the segmented images on their website and calculated the quantitative assessments using those images.

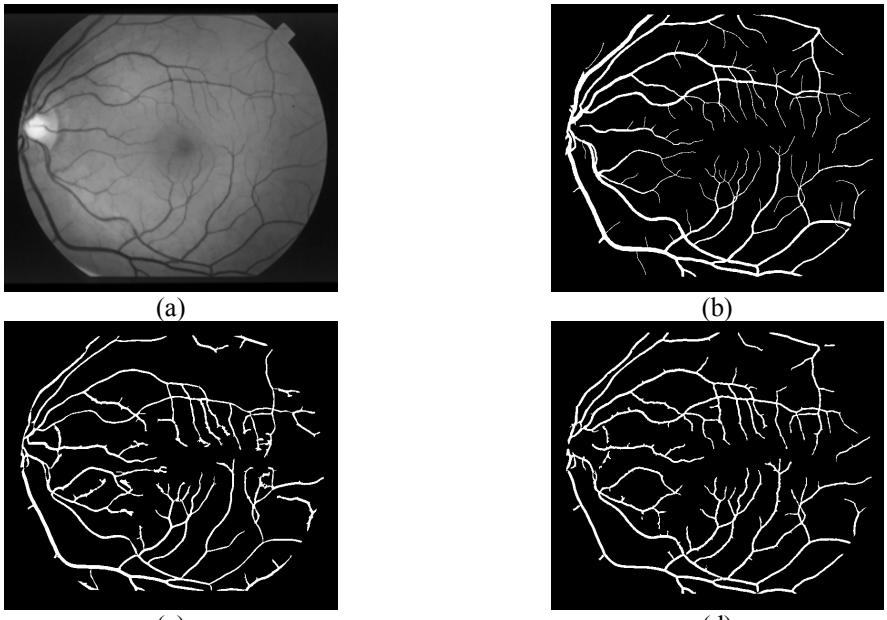

Figure 3.28. (a) A normal image in the STARE database; (b) the hand-labeled ground truth; (c) the extracted vessel map by the scheme in [4]: Accuracy = 0.9320, TPR = 0.6992, FPR = 0.0393; (d) the extracted vessel map by the proposed method: Accuracy = 0.9487, TPR = 0.7625, FPR = 0.0283.

The Hoover's method in [20] tries to eliminate the false positives caused by lesions through threshold-probing and the Mendonça's method described, in [23] tries to eliminate the false positives caused by lesions through combing the centerline detection and a modified top-hat operation. Figure 3.27 (a) shows a pathological image from the STARE database, (b) shows the ground truth as manually labeled by the first observer (labels-ah), (c) shows an image of a vessel extracted using the scheme [20] and (d) shows the vessel map extracted using the proposed method. The proposed method not only detects more small vessels than methods proposed by Hoover and Mendonça, [20] [23] else and does so at a lower FPR, it also makes many fewer false detections. These advantages are very important because the edges of bright lesions have large curvatures as shown at Figure 3.27 (c) so it is easy to misclassify them as neovascular.

Figure 3.28 (a) shows a normal image from the STARE database, (b) shows the ground truth as manually labeled by the first observer (labels-ah), (c) shows an

image of vessels extracted using the Hoover's method [20] and (d) shows the vessel map extracted using the proposed method. We see that the proposed method can detect more small vessels than Hoover's method [20].

Table 3.5 lists the results of ACC, TPR and FPR for the STARE database extracted by different methods. Table 3.6 compares the running time of the proposed method with those state-of-art methods. From Tables 3.IV and 3.V, we can see that the proposed method gets the highest TPR on the pathological images at a very low FPR. It also has a much lower computational complexity than that of Hoover's method [20] and Mendonça's method [23] [5].

Table 3.4 Extraction Results of ZUEYE Database

Method	Accuracy	TPR	FPR
Hoover [20]	0.9380	0.7462	0.0408
Proposed method	0.9536	0.7954	0.0311

Table 3.5 Extraction Results of STARE Database

Method	Accuracy	TPR	FPR
Normal cases			
2nd Human observer	0.9283	0.8252	0.0456
Hoover [20]	0.9324	0.6736	0.0528
Mendonça [23]	0.9531	0.7366	0.0178
Proposed method	0.9497	0.6611	0.0152
Pathological cases			
2nd Human observer	0.9425	0.8252	0.0456
Hoover [20]	0.9211	0.6736	0.0528
Mendonça [23]	0.9426	0.6801	0.0306
Proposed method	0.9416	0.7286	0.0372

Table 3.6 Running Time per Image in STARE Database

Method	System Environment	Running Time
Hoover [20]	P-III 1.5GHz, 512 Mb RAM, **Windows executable**	0.5 minute
Mendonça[23]	P-IV 3.2GHz, 960 Mb RAM, **Matlab**	3 minutes
Proposed method	P-III 1.5GHz, 512 Mb RAM, **Matlab**	0.5 minute

[5] Note that the running time of the algorithm [20] listed in Table III is not very long because it ran as a Windows executable file, while the other two schemes ran in Matlab programming environment.

3.3 Conclusion

This chapter has described the major difficulties in vasculature segmentation and the two proposed segmentation techniques to overcome some of the difficulties. This chapter makes two major contributions as follows.

First, we demonstrated that scale production is an efficient strategy for fusing multiscale vessel responses by identifying vessel pixels in the scale production domain. This scale production makes it possible to enhance vessels while suppressing noise because the vessels will have relatively strong responses to the matched filters along scale space while the background noise decreases rapidly. The experimental results show that the proposed method can extract both wide and thin vessels concurrently with low computational complexity.

Second, the matched filter does not work well on pathological images and therefore, we presented a modified matched filter approach that detects vessels in a retinal image while suppressing non-vessel edge structures. The modified matched filter does not remove the image background but uses a local double-side thresholding to avoid responding to non-line edges. The experiments on retinal images demonstrated that the proposed method does a good job of detecting the neovasculars and eliminating many non-vessel edges caused by bright lesions. This is a desirable property in PDR screening because the edges of bright lesions have large curvatures which make them easy to misclassify as neovasculars.

Chapter 4 A Top-Down Retinal Image Segmentation System for Diabetic Retinopathy Screening

Automated segmentation of colour retinal images can help eye-care specialists screen Diabetic Retinopathy (DR) in large populations. An automated retinal image segmentation system should have the ability to segment the images based on both pathological and physical features so that the DR could be diagnosed using the segmented results. DR may be diagnosed using either pathological or physical features. The pathological would include features such as red lesions (intraretinal hemorrhages, microaneurysms), bright lesions (hard exudates and cottonwool spots) while the physical would include features such as vessels, optic disc, and fovea [11]--[15]. In this chapter, we design an automated segmentation system which can segment most of the features so that most of the DR could be diagnosed.

The automated segmentation of red lesions was reported in [4][49][50][89][99][100] [101]--[110][111][112][113]. The automated segmentation of bright lesions was reported in [4][50][53][68][69] [73][74][86]--[91][92]--[94]. The automated segmentation of vessels was reported in [3][4][9][10][16]-[40]. As for non-pathological or physical features, the automated segmentation of optic disc and fovea was reported in [50][65][66][67]--[73][75][76][77]--[84].

Despite all of this work, retinal image segmentation remains a difficult task. The major difficulty comes from the fact that retinal objects-pathological and physical-mutually affect each other, producing false positives for one feature or another. For example, the extraction of vessels may be affected by bright lesions and red lesions; the extraction of bright lesions may be affected by the optic disc; and the extraction of the optic disc may be affected by bright lesions and vessels. There have been a

number of proposals made to obviate these phenomena. In [46], Walter *et al.* proposed a local contrast and water-shed based method that suppressed the effect of the optic disc when extracting bright lesions. In [90], a PCA based method was used to extract optic disc so as to avoid false positive bright lesions. However, both of these methods are less effective if there are many bright lesions. In [77][78], Hoover and Goldbaum detected the optic disc by finding vessel convergences but the false positives of vessels will cause this method less effective. In [16], Soares *et al.* proposed a supervised method for extracting vessels that demonstrated good performance that produced fewer false positives but still had problems processing the area close to bright lesions. In [35], Lam and Yan proposed a GVF based method that extracted vessels and was good at suppressing false positives caused by bright lesions but the vessel width information was not extracted well.

In [9], Staal *et al.* suggested removing all lesions before vessel extraction. In [34], Elena *et al.* also suggested that a method to eliminate all lesions has to be implemented for better vessel extraction. Since both the physical features and pathological features are all useful for diagnosis, a scheme to extract all these features in a flow with consideration on the affections among these features will be more efficient and more effective. The automated detection of vessels, optic disc, fovea, hemorrhages, microaneurysms, and hard exudates was reported in [50]. However, the information among features has not been sufficiently used by their scheme. This chapter proposes a Top-Down scheme to extract the features to diagnosis DR. The proposed scheme can suppress the affection among features during feature extraction. Figure 4.1 shows our Top-Down Scheme. As shown in Figure 4.1, the proposed scheme will segment all bright objects and red objects first. Then the bright objects will be classified into bright lesions and the optic disk. After

the erasing of all bright objects, the red objects will be classified into vessels and red lesions. Notice that in this Top-Down scheme the fovea is not defined as red objects simply because it is too large to be found by our "red objects finder". The fovea is finally located with the help of the location of the optic disk. As shown in Figure 4.1, the segmentation of bright objects will help the segmentation of vessels, and then the segmentation of vessels will help the segmentation of the optic disk, and then the segmentation of the optic disk will help the segmentation of the bright lesions and the fovea. Therefore the relations among different objects in retina have been efficiently used by our scheme.

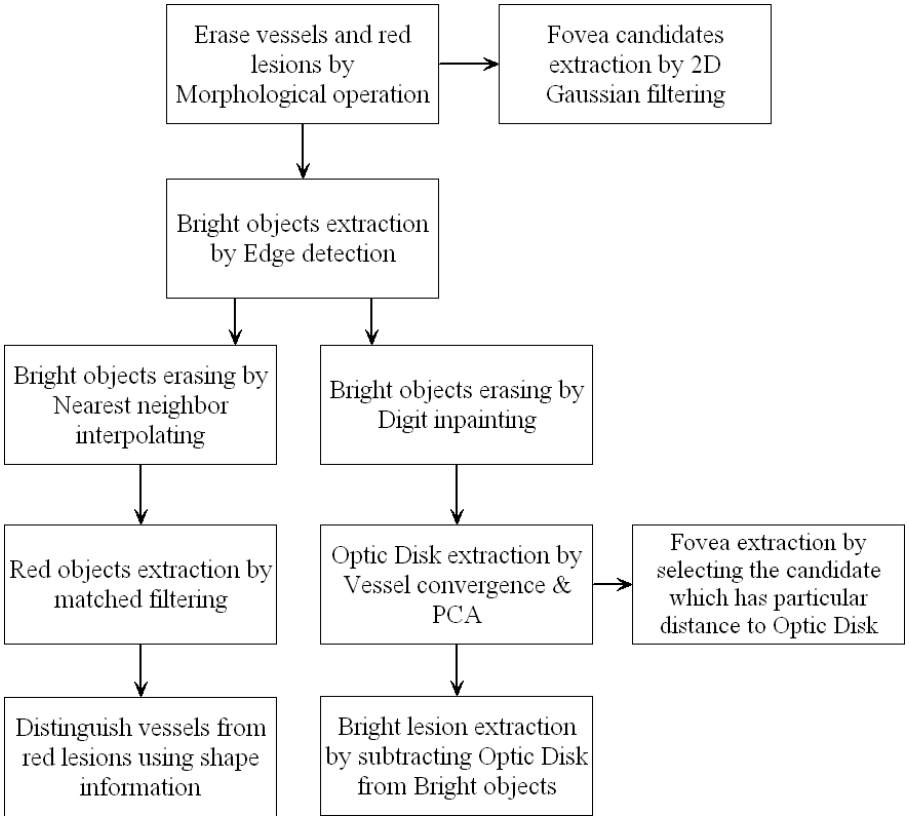

Figure 4.1. Proposed scheme to segment retinal images for DR diagnosis.

Our retinal image segmentation scheme is described in details in the rest of this chapter. Section 1 describes the segmentation of bright lesions and the optic disc. Section 2 describes the segmentation of red lesions and vessels. Section 3 describes the extraction of the fovea. Section 4 describes our experiments and results. Section 5 offers our conclusion.

4.1 Bright Object Segmentation

Retinal bright objects include bright lesions and the optic disc. As shown in Figure 4.1, we will segment all bright objects first. Then the optic disc will be separated from bright lesions.

4.1.1 Finding All Bright Objects

The size and brightness of bright objects can vary a lot in a retinal image with DR. Edge is the most robust feature to find all bright objects. We adopt the method proposed by Walter *et al.* [46] with some improvement, which is briefly described as follows:

Step 1): Eliminating vessels. Vessels produce strong edges. These strong edges must be eliminated before edge detection. In [46], Walter *et al.* applied a morphological closing before the edge detection. But the closing operation will generate many disc-like structures, which means the image will be not as smooth as before. These disc-like structures may result in false detection of bright lesions.

The morphological “erode followed by reconstruction” operation will usually produce smoother results than closing. But it may cause over-reconstructed images.

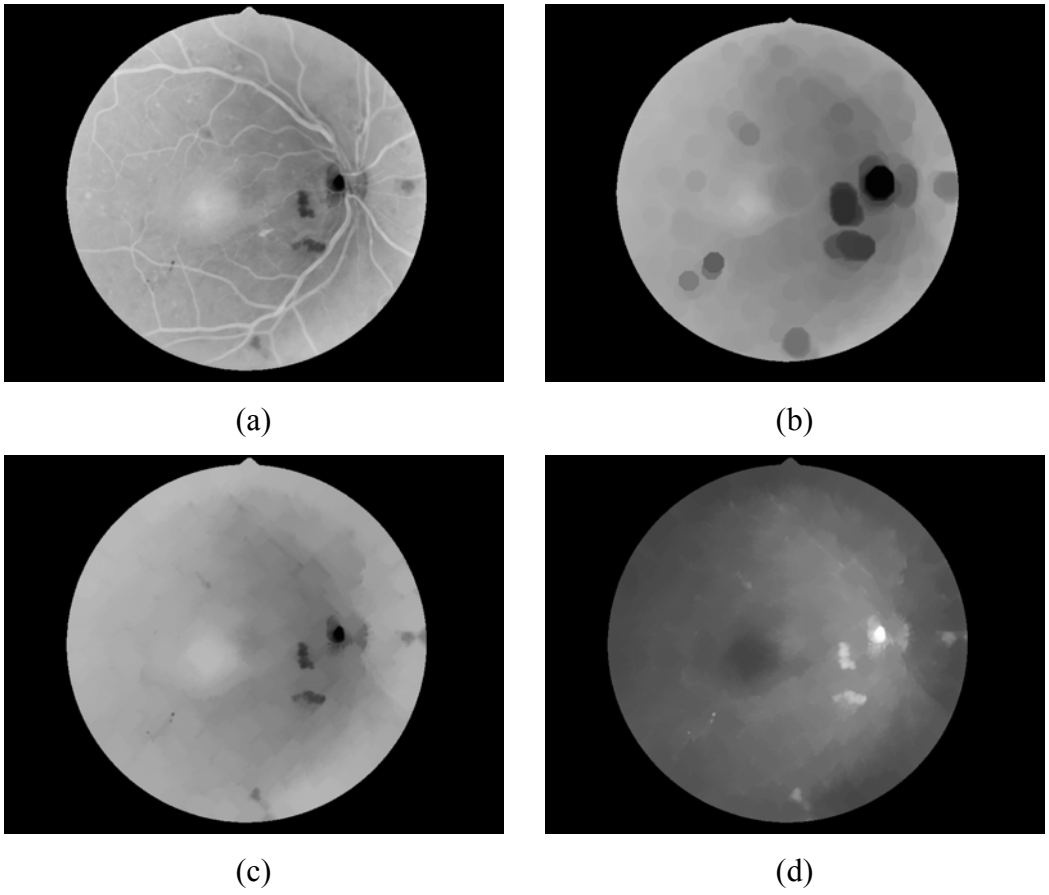

(a) (b)

(c) (d)

Figure 4.2. Eliminating vessels. (a) the inversed green channel $\overline{I_g}$, (b) I_1: eroded (b), (c) I_2: reconstructed I_1, (d) $\overline{I_2}$: inversed I_2

We propose a controlled reconstruction here. First, the vessels are eliminated by erode defined by Equation 4.1:

$$I_1 = \overline{I_g} \Theta B_{S1} \tag{4.1}$$

where $\overline{I_g}$ is the complement of the green channel of the original image, Θ is erode, B_{S1} is a disc structure with radius S1 pixels. S1 should be large enough to eliminate all vessels. After that, with initializing $I_2 = I_1$, the eroded image will be reconstructed by

$$R = \min\left(I_2 \oplus B_1, \overline{I_g}\right); \quad I_2 = R \tag{4.2}$$

where $\oplus$ is dilate, B_1 is a disc structure with radius 1 pixel. The minimum of dilated I_2 image and $\overline{I_g}$ is assigned to *R*. Equation 4.2 will be repeated N times where N is larger than S1. Figure 4.2 shows this step.

Step 2): Detecting edges. Once the vessels are eliminated, all edges remained on the image should be caused by bright lesions. We apply canny edge detector on $\overline{I_2}$ at two different scales and use scale multiplication to enhance the detection [116]. The edge detection filter used here is FDOG.

$$f(x) = -x \cdot e^{-x^2/2} \tag{4.3}.$$

The dilation of $f(x)$ by scale *s* is

$$f(x) = -x \cdot e^{-x^2/2s^2} / s^2 \tag{4.4}.$$

A small scale s_1 and a large scale s_2 are used to detect edges. The responses of canny edge detector at two scales can be denoted as $R_{s_1}(x)$ and $R_{s_2}(x)$. The scale multiplication is defined as the product of $R_{s_1}(x)$ and $R_{s_2}(x)$

$$P(x) = R_{s_1}(x) \cdot R_{s_2}(x) \tag{4.5}.$$

The double thresholding [55] strategy is used to threshold the canny filtering results. Double-thresholding imposes a low threshold t_l and a high threshold $t_h = 2t_l$ are imposed on $P(x)$, which produces two edge maps E_l and E_h. The final edge map is formed by selecting edges in E_l that link to the edges in E_h.This strategy is good at avoiding broken edges. Figure 4.3 shows this step. Figure 4.3(a)-(c) shows the effect of scale multiplication. The improvement from single scale to scale multiplication is obvious. Figure 4.3(d)-(e) shows the effect of double

thresholding. The segmented result has few broken edges and many fewer false edges.

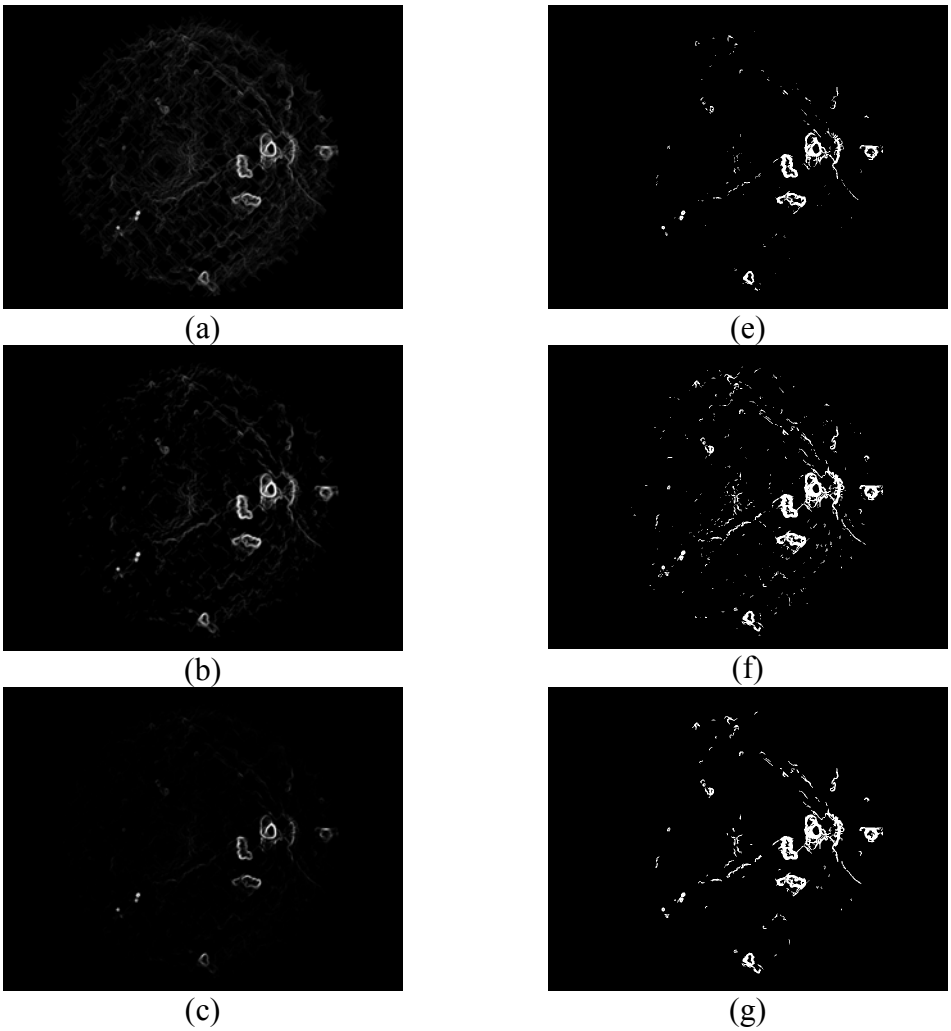

Figure 4.3. Detecting edges. (a) & (b) canny edge detector at two different scales, (c) scale production of (a) & (b), (e) thresholding (c) with a high threshold, (f) thresholding (c) with a low threshold, (g) I_3 : link (e) to (f).

Step 3): Finding the contours of bright objects. The method proposed by Walter et al. [46] is employed here to locate the final contour of the bright objects from among a selection of bright object candidates. After filling of the holes in I_3, the filled objects will be regarded as bright object candidates. The exact contour of the bright lesions will be extracted by morphological reconstruction. The marker image I_4 is generated by setting all the candidates to 0 in the green channel of the original image I_g. The mask image is I_g. The difference between the reconstructed image I_5 and

I_g is double thresholded to generate the bright objects I_6. Figure 4.4 shows this step.

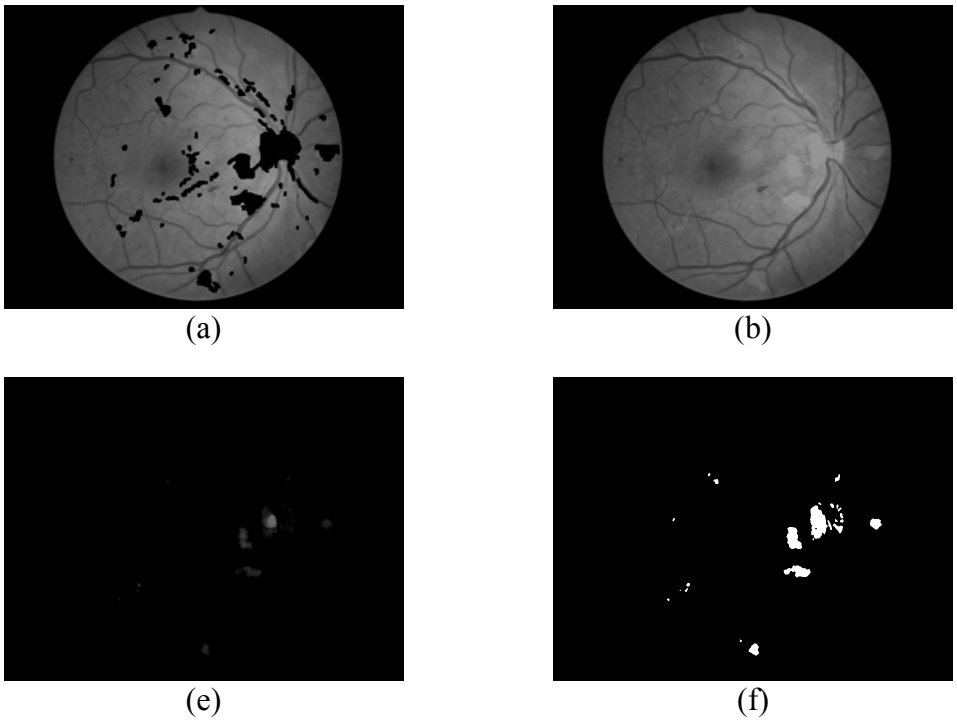

(a) (b)

(e) (f)

Figure 4.4. Finding contour of bright lesions. (a) reconstruction marker, (b) reconstructed image I_5, (c) difference between I_5 and I_g, (d) thresholding.

4.1.2 Extracting the Optic Disc and Bright Lesions

After bright objects have been extracted, they have to be classified into bright lesions and the optic disc. In this section, we propose a method for extracting the optic disc, which provides better accuracy. A major difficulty in optic disc segmentation is from the bright lesions, which are easy to be recognized as optic discs. Figure 4.5 shows an example using an image from the STARE database [20]).

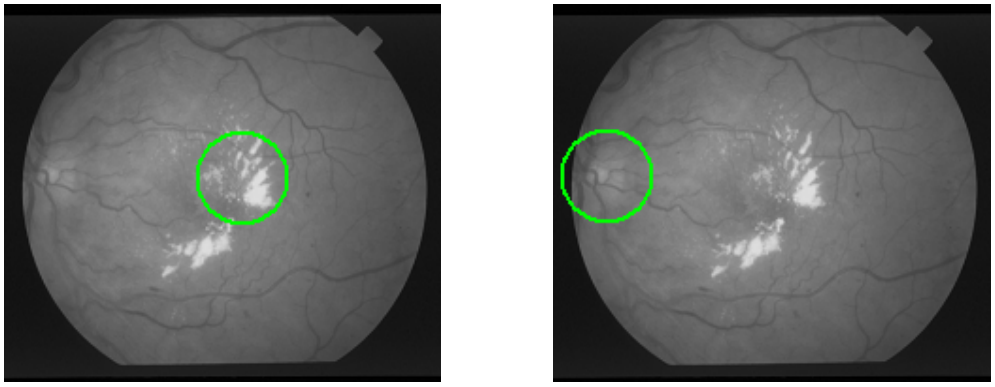

(a) (b)

Figure 4.5. Optic disc extraction. (a) PCA based method [67][68][69][90]; (b) our method.

In [67][68][69][90], the optic disc is located using a PCA based method. In [77][78], the optic disc is located as the convergence of vessels. Both of these methods are greatly affected by bright lesions. The PCA based method may be fail because the bright lesions and optic disc are all bright objects. The vessel convergence method may fail if the gaps between bright lesions may be recognized as vessels. To find the correct vessel convergence, we first erase all bright objects and then improve accuracy by combining the vessel convergence based method and the PCA based method together. The details are as follows.

Step 1): Erasing bright objects by digit inpainting. To find the vessel convergence, it is first necessary to find the vessels. The matched filter [3][20] can produce good vessel segmentation and avoid broken vessels. The optic disc must be at the convergence of large vessels. We use a matched filter with large σ to ignore small vessels. One problem of a matched filter is that it produces strong responses to the edges of bright objects. To avoid false positives of vessels, bright objects should be erased before applying a matched filter. A simple way to erase the bright objects is to pad the holes using morphological reconstruction as shown in Figure 4.4(a) & (b). But the edge of the area padded by this method is not smooth enough. We choose the exemplar-based inpainting described in [121] to pad the holes.

Inpainting depends upon a bright object being regarded as a single object, but a bright object that is split by vessels may be taken for background, so the first step in inpainting is to implement a closing. First a morphological eroding is applied to the closed image to ensure that the area surrounding bright objects is regarded as background. And then The eroded image and the original image can be used to generate the inpainting mask as shown in Figure 4.6(a). Finally, the inpainting can be applied based on that inpainting mask to generate the image I_7 that has no bright objects.

Figure 4.6(b) shows the result of inpainting. The edges are very smooth, which means that vessel false positives can be better suppressed. One problem of this method, however, is that it will make the vessels which is crossing bright objects grow to wrong orientations. As shown in Figure 4.6(b), some vessels crossing the optic disc have been extended. The orientations estimated by inpainting are not the same as the original but they are sufficiently similar that it does not affect the identification of vessel convergence.

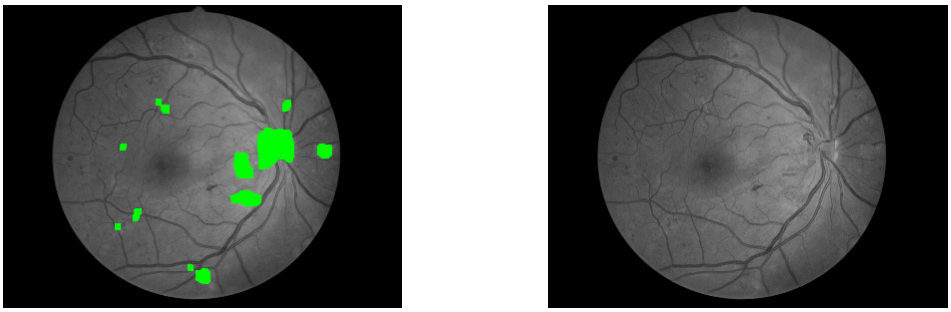

(a) (b)

Figure 4.6. Erasing bright objects. (a) The mask for inpainting, (b) inpainting result.

Step 2): Finding vessel convergence. Large vessels and those with a high local contrast can be extracted by applying a matched filter [3] with large σ (Figure 4.7 (a)). Regions of vessel convergence can be located by applying the fuzzy convergence proposed in [77][78]. Figure 4.7 (b) shows the vessel convergence. These regions of vessel convergence can be used as candidate optic disc.

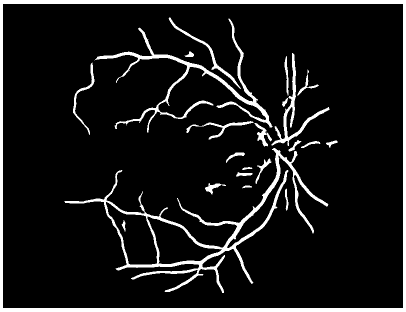

(a)

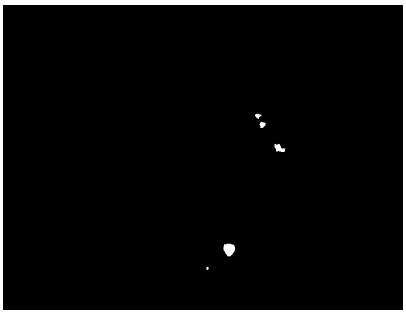

(b)

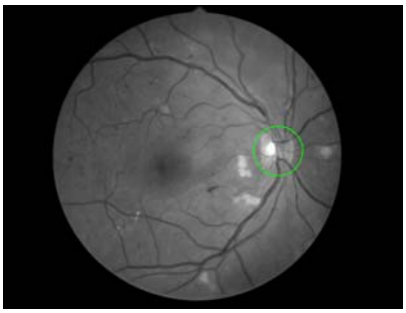

(c)

Figure 4.7. Finding optic disc. (a) vessels, (b) regions of vessel convergence, (c) optic disc located.

Step 3): Locating optic discs. The centers of regions of vessel convergence are used as initial points where we apply the PCA based method described in [67]. First, we manually cut some optic discs of the images are to obtain the training data. We then calculate the eigen vectors of the covariance matrix of the training data, which we then refer to as eigen optic discs. We next iteratively move a square window on the retinal image using the initial points obtained above as the initial position of the iteration. The sub-image inside the square window is projected onto the optic disc space and the reconstruction error is calculated. The sub-image with the minimum reconstruction error will be classified as the optic disc. We denote the radius of an

optic disc by D_O so that the optic disc center is located at the initial point's N by N neighborhood, where $N = 2 * D_O$. Figure 4.7 (c) shows the located optic disc. The optic disc of average radius is indicated with a green circle.

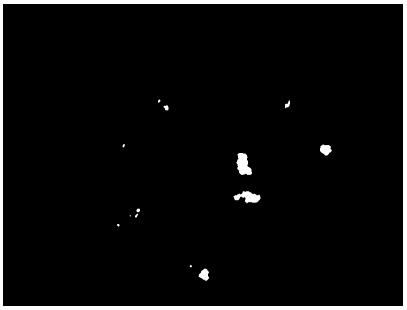

Figure 4.8. I_8: Bright lesions.

Step 4): Extracting bright lesions. Once the optic has been located, all bright objects outside the green circle shown in Figure 4.7(c) will be extracted as bright lesions which are shown in Figure 4.8.

4.2 Red Object Segmentation

The retinal red objects include red lesions and vessels. There are kinds of red lesions. We only focus on the segmentation of microaneurysm which is a major sign of DR and appear as small round objects. As shown in Figure 4.1, first, the bright lesions will be erased to avoid false detections. Then the microaneurysms and vessels are separated using the mathematical morphology based method proposed by Spencer *et al*. [41] and Frame *et al*. [42]. Finally, the microaneurysms are segmented based on the matched filter proposed by Spencer *et al*. [41] and Frame *et al*. [42]; and the vessels are segmented based on the matched filter proposed by Chaudhuri *et al*. [3]. This procedure is described as follows.

Step 1): Erasing bright objects by nearest neighbor interpolation. Bright objects will affect the detection of red objects and they should be erased before red object extraction. In Section 4.1, the bright objects were erased using exemplar based inpainting [121]. The problem of this technique is that it makes the vessels which are crossing bright objects grow to wrong orientations. This will not affect the finding of vessel convergence, but will affect vessel extraction. To erase the bright objects, we use nearest neighbor interpolation, which is similar to the technique in [16] for padding the area outside region of interest. First, the image to be padded is generated by impose the image without vessels $\overline{I_2}$ (Figure 4.2(d)) on the bright lesion image I_8. The bright lesions are used as markers for padding. We erase all vessels here so that only background is used to pad the marked area. The optic disk has not been erased because the padding of the optic disk generally cause the lost of vessels inside it. Second, pixels which are inside the marked area and within the 4-neighborhood of the pixels outside the marked area are replaced with the mean value of their 8 neighbors outside the marked area. This procedure is repeated until the marked area is full. Third, the minimum of this padded image and I_g (the green channel of the original image) is used to generate the image I_9 for following red object extraction. Figure 4.9 (a) shows the padding markers; Figure 4.9 (b) shows the padding result; Figure 4.9 (c) shows I_9; Figure 4.9 (d), (e) and (f) are blocks of the I_g, padded result, and I_9, respectively.

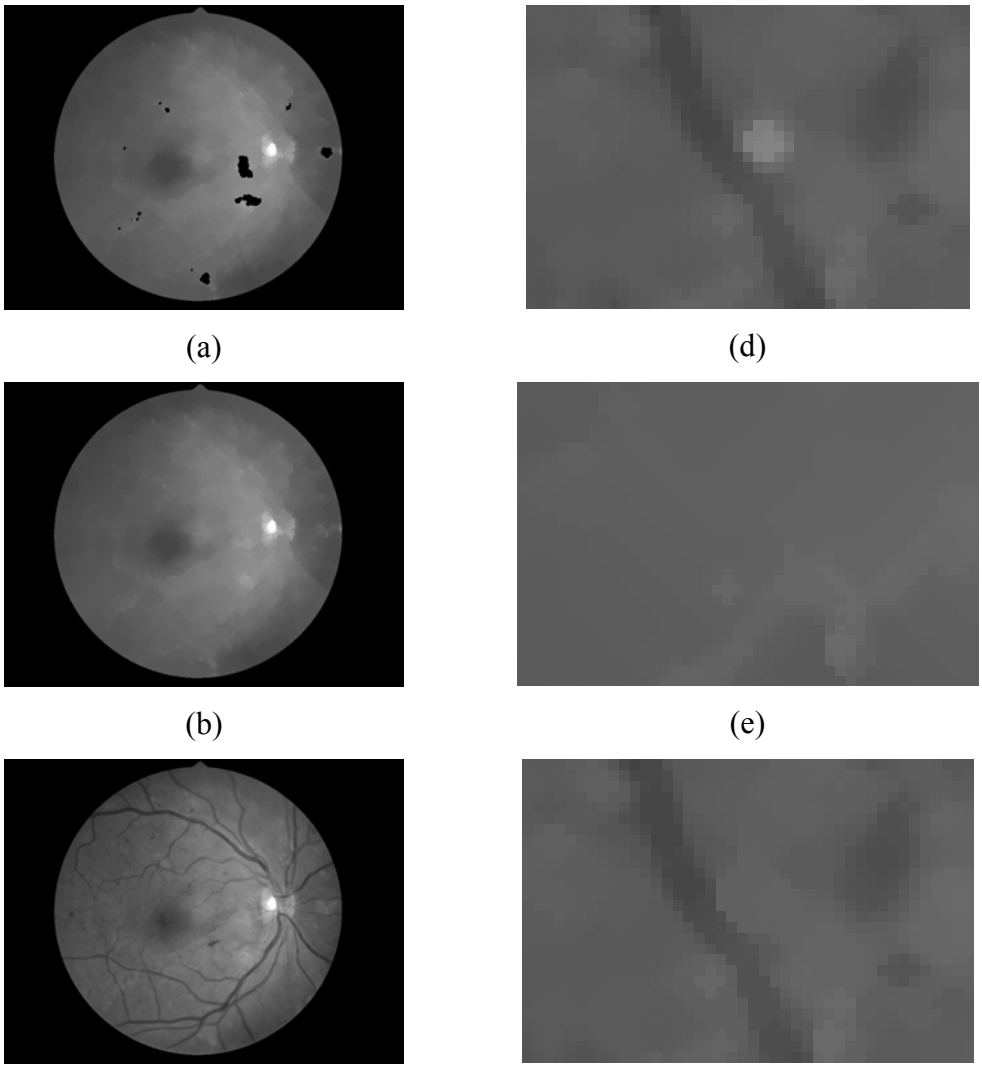

Figure 4.9. (a) Image to pad; (b) Image padded; (c) I_9: image for red objects extraction; (d), (e) and (f) are blocks of the I_g, padded result, and I_9, respectively.

Step 2): Microaneurysms and vessels separating. Spencer *et al*. [41] and Frame *et al*. [42] have proposed a modified morphological top-hat transformation to discriminate between circular, non-connected red lesions and the elongated vessels in FA images. In order to use their modified top-hat transformation, I_9 has to be complemented first (shown at Figure 4.10 (a), denoted as $\overline{I_9}$). A morphological opening with a linear structuring element at 12 different orientations is applied to $\overline{I_9}$. Using the maximum of the 12 opened images, we obtain an image I_{vessel} which only contains vessels. We then subtract I_{vessel} from $\overline{I_9}$ to obtain an image containing microaneurysms. Figure 4.10 shows this step.

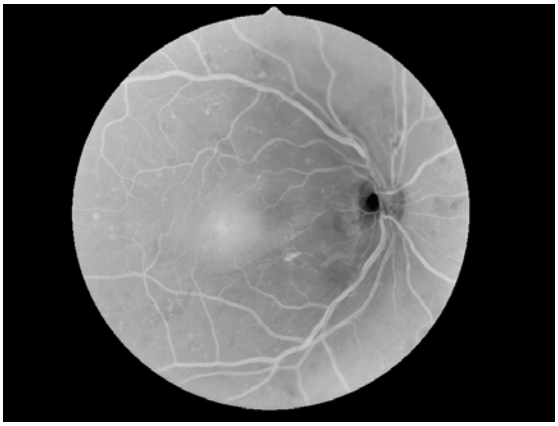

(a)

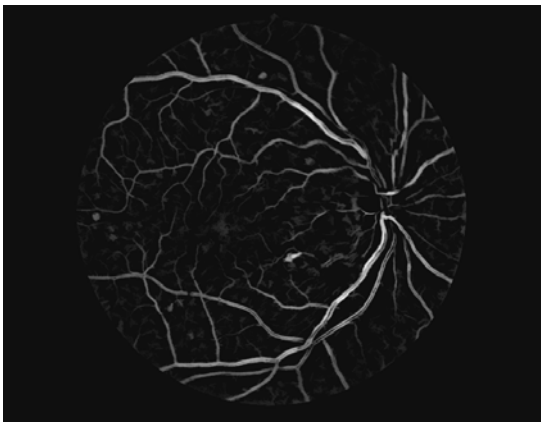

(b)

(c)

Figure 4.10. (a) $\overline{I_9}$: implement of I_9; (b) I_{vessel} : image contains vessels; (c) I_{ma} : image contains microaneurysms.

Step 3): Vessel extraction using MPMF. We segmented the vessels in the image I_{vessel} by applying the MPMF proposed in Chapter 3.1. Figure 4.11 shows this step.

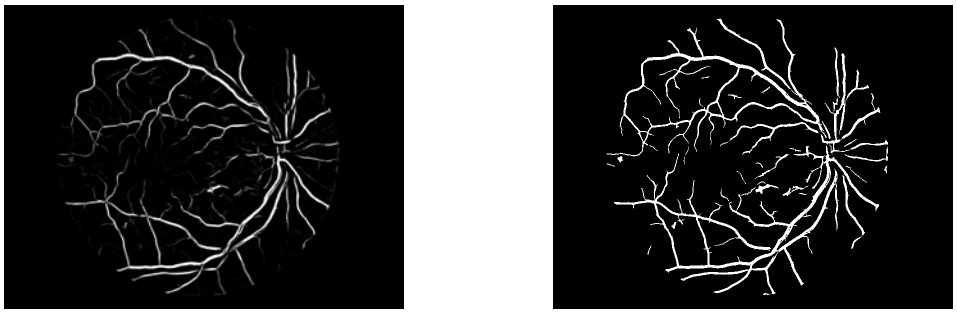

(a) (b)

Figure 4.11. (a) enhanced vessels; (b) segmented vessels.

Step 4): Microaneurysm extraction based on the matched filter proposed by Spencer *et al*. [41] and Frame *et al*. [42]. This matched filter is a 2-D Gaussian. Microaneurysms are enhanced and segmented as shown in Figure 4.12.

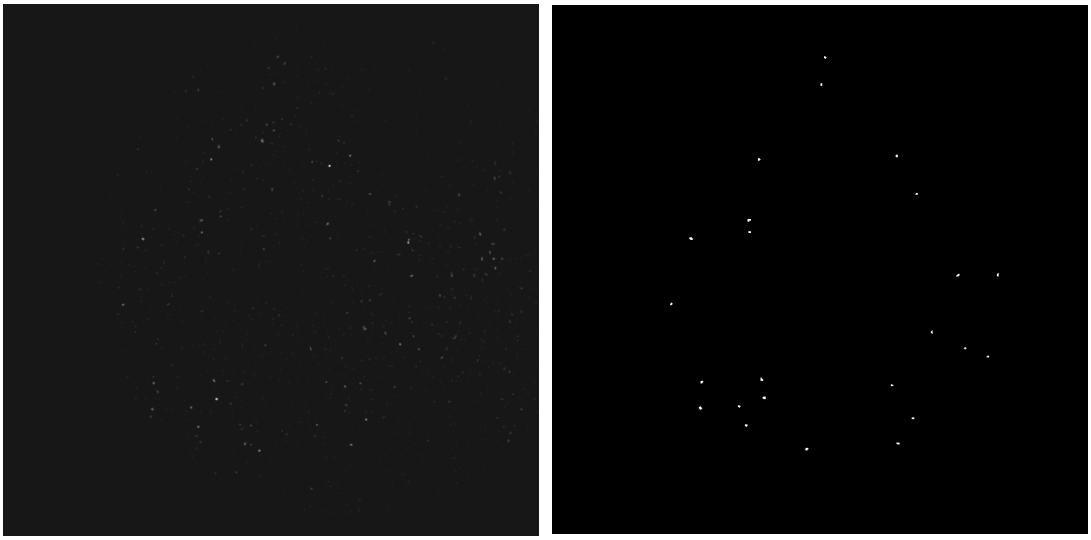

(a) (b)

Figure 4.12. (a) enhanced microaneurysms; (b) segmented microaneurysms.

4.3 Fovea extraction

To extract the fovea, we apply a 2D Gaussian filter with zero sum and σ 20 pixels to an image without vessels $\overline{I_2}$ (Figure 4.2(d)) so as to avoid the interference from vessels. The filter is defined as

$$G(x,y) = -\exp\left(-(x^2+y^2)/2\sigma^2\right) - m, \quad \text{for } |x| \le 3\sigma, \quad |y| \le 3\sigma \tag{4.6}$$

where σ represents the scale of the filter; $m = -\int_{-3\sigma}^{3\sigma}\int_{-3\sigma}^{3\sigma}(\exp\left(-(x^2+y^2)/2\sigma^2\right)dxdy)/\left(6\sigma\right)^2$ is used to normalize the mean value of the filter to 0 so that the smooth background can be removed after filtering.

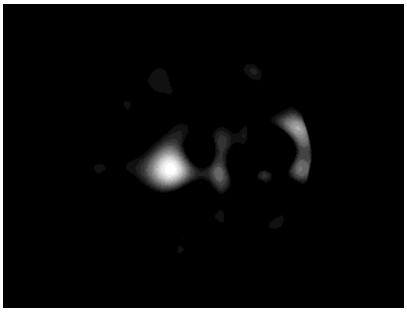

(a)

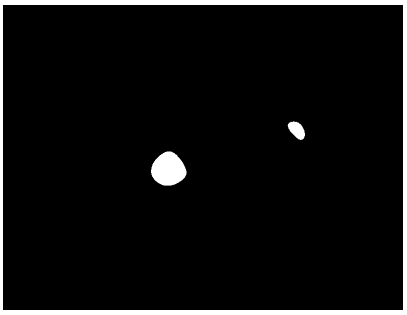

(b)

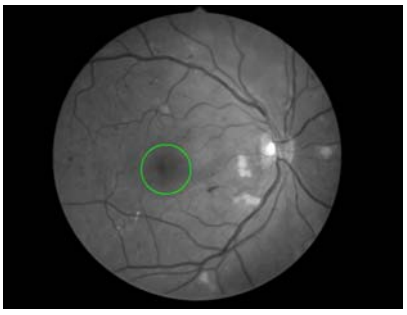

(c)

Figure 4.13. Finding fovea. (a) filter response, (b) fovea candidates, (c) fovea detected.

The filter response (Figure 4.13 (a)) will be thresholded to identify the candidate regions as shown in Figure 4.13(b). We already have the location of the optic disk. The distance between the center of optic disk and fovea should be $4*D_O$. The candidate region which can satisfy this constraint will be regarded as the fovea. This constraint can further ensure the accuracy of fovea detection.

4.4 Experimental Results

In this section we evaluate the performance of the proposed system by applying it to retinal images of ZUEYE database constructed from DR patients[6] . We use 20 images captured by using a Kowa VK-3 fundus camera at 45^o field of view (FOV). The images were stored in 24-bit digital format. The resolution of the images is 800×608. We asked ophthalmologists to manually segment the images as the ground truth. All 20 images have microaneurysms and 15 display bright lesions.

We evaluated the images in two ways, according to how many lesions were correctly classified and according to how many image pixels were correctly classified.

Pixel based evaluation was used to evaluate the performance of vessel segmentation and bright lesion segmentation. To evaluate the extraction of vessels and bright lesions, we use the same evaluation measures as were used in [46] True positives (TP), that is, vessel pixels correctly classified, are defined as

$$TP = \#\left[S\left(\delta^B(O_m) \wedge O_c\right)\right] \tag{4.7}$$

where # means "the number of", $S(f)$ is the support of f, $\delta^B(f)$ means dilating f using structure element B, $\wedge$ is the logical "and" operation, O_m are the manually segmented objects, and O_c is the computerized segmentation. Here we set B as a disk of 1 pixel radius. We define false positives (FP), that is, background pixels classified as vessel pixels, and false negatives (FN), vessel pixels classified as background pixels, as

$$FP = \#\left[S\left(O_c\right) \setminus S\left(\delta^B(O_m) \wedge O_c\right)\right] \tag{4.8}$$

[6] The images were collected from the patients in the Ophthalmologic Department, the First Affiliated Hospital of Zhengzhou University, Henan Province, China.

$$FN = \#\left[S(O_m) \setminus S\left(O_m \wedge \delta^B(O_c)\right)\right] \tag{4.9}$$

where \ is the set difference. We plot sensitivity against predictive value to evaluate the performance. The structure element B used in our experiments is a disk of 1 pixel radius. With this dilation, some pixels on the edge of the targeted objects will be ignored in the evaluation. Those pixels are easy to be misclassified but are not important for clinicians. The performance measures are defined as

$$sensitivity = \frac{TP}{TP + FN} = TPR \tag{4.10}$$

$$specificity = \frac{TN}{TN + FP} = TNR \tag{4.11}$$

$$predictive\ value = \frac{TP}{TP + FP} \tag{4.12}$$

As all microaneurysms are of a similar size, we use lesion based evaluation to evaluate their extraction. The performance measures are the same with those defined above but do not apply the dilation operation.

4.4.1. Experiments on bright lesion extraction

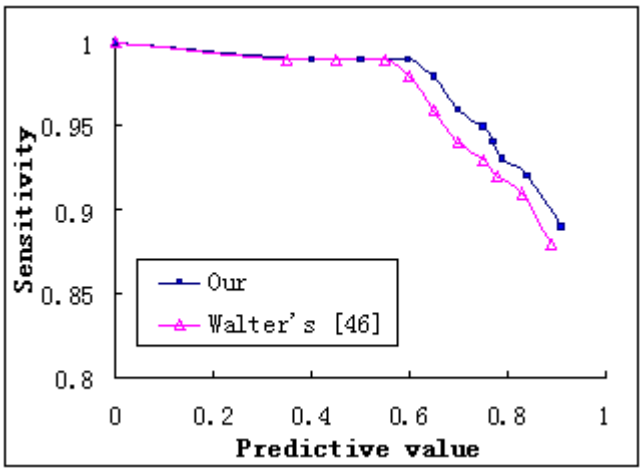

Figure 4.14. Bright lesion segmentation evaluation.

Figure 4.14 and Table 4.1 show the bright lesion extraction performance in terms of plot sensitivity against predictive value. While it is difficult to compare results on

different databases, our method compared well with Walter's [46] and Sinthanayothin's [50] We achieved a sensitivity of 89.5% and a predictive value 91.2% while the Walter's achieved a sensitivity of 88.4% and a predictive value 89.3%. The results reported by Sinthanayothin *et al.* [50] are a sensitivity of 88.5% and a predictive value of 82.6%. The improvement in accuracy provided by our bright lesion extraction method is satisfactory. We attribute it to improvements in controlled reconstruction, scale production, and double thresholding.

Table 4.1 Bright lesion segmentation

Method	Database	Sensitivity	Predictive value
Walter [46]	ZUEYE	88.4%	89.3%
Sinthanayothin [50]	St Thomas' Hospital	88.5%	82.6%
Proposed method	ZUEYE	89.5%	91.2%

4.4.2. Experiments on microaneurysm extraction

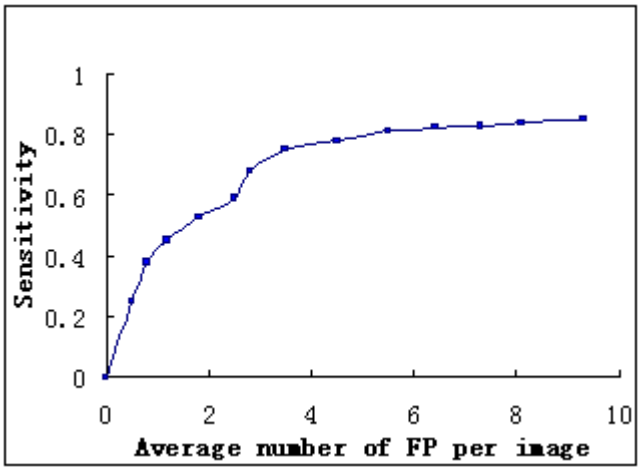

Figure 4.15. Microaneurysms extraction evaluation.

Figure 4.15 and table 4.2 show the performance of our approach to microaneurysm extraction in terms of plot sensitivity against FP per image. Our microaneurysm extraction is, based on a simple method proposed by Frame and Spencer [41][42], which was actually designed for FA images. Again we compare the results of our method with that of Walter *et al*. [53]. Their method achieved a sensitivity of 88.47%

at 2.13 FP per image. Our method achieves a sensitivity of 68.3% at 2.81 FP per image. While our method does not compare in terms of performance, it does show that a simple method normally used on FA images [41][42] can be applied to color retinal images after appropriate preprocessing and can provide segmentation that is useful for clinicians. It also efficiently suppresses false positives.

Table 4.2 MA detection

Method	Database	Sensitivity	FP
Walter [53]	Walter's	88.4%	2.13
Niemeijer [10]	DIARETDB1	85.6%	2
Proposed method	ZUEYE	68.3%	2.81

4.4.3. Experiments on vessel extraction

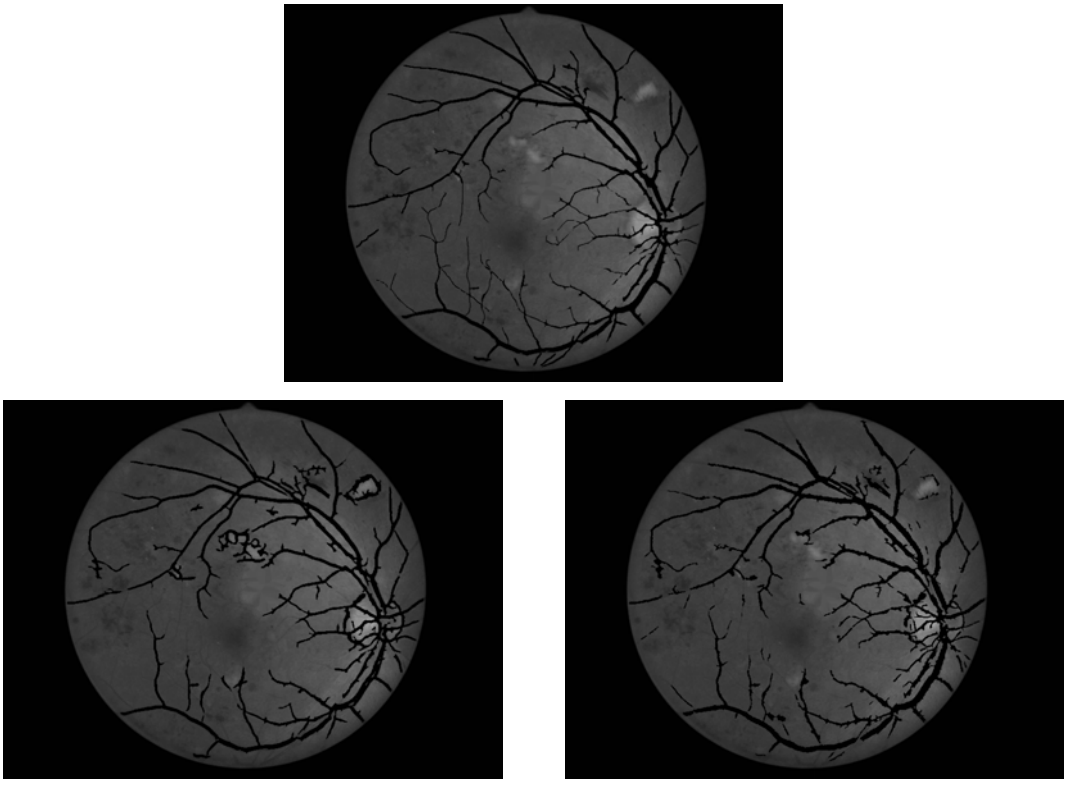

(b) (c)

Figure 4.16. An example of vessel extraction. (a) hand labeled ground truth; (b) Hoover's result : sensitivity=0.924, predictive value=0.846 (c) our result: sensitivity=0.937, predictive value=0.888.

Figure 4.16 shows an example of vessel extraction using our method. Figure 4.17

and Table 4.3 show the results for the extraction of red lesion in terms of plot sensitivity against predictive value comparing with Hoover's vessel extraction [20] method. Our method has erased bright lesions and thus, gets fewer false positives.

Table 4.3 Vessel segmentation

Method	Database	Sensitivity	Predictive value
Hoover［20］	ZUEYE	85.1%	93.5%
Proposed method	ZUEYE	90.2%	93.4%

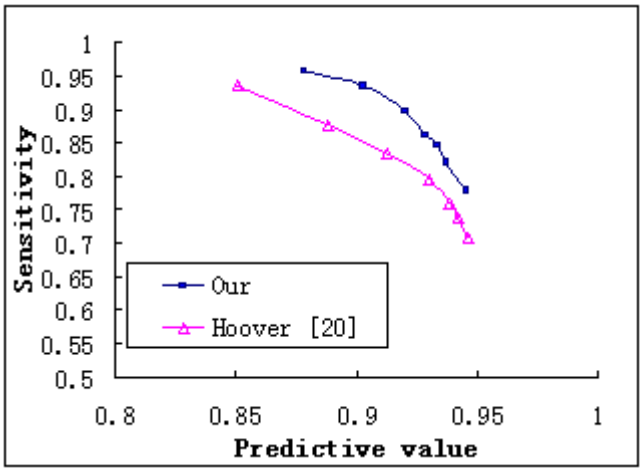

Figure 4.17. Vessel segmentation evaluation.

4.4.4. Experiments on optic disk

We evaluated the performance of our system at detecting the optic disk using STARE database. To compare with the PCA based method proposed by Li and Chutatape [67], we implemented their algorithm. We used a leave-one-out scheme in which 19 images were used for training and one for testing. On STARE database, all 20 optic disks were accurately located by our method while 19 optic disks were accurately located by Li and Chutatape [67], which we attribute to the erasure of bright lesions preventing the false detections.

Table 4.4 OD detection

Method	Database	Accuracy
Li [67]	ZUEYE	100%
Proposed method	ZUEYE	100%
Li [67]	STARE	95%
Proposed method	STARE	100%

4.4.5. Experiments on fovea

On our database, all 20 images present fovea clearly. On the experiment, all 20 foveae are accurately located because the correct location of optic disc provides a useful constraint for fovea detection.

Table 4.5 Fovea detection

Method	Database	Accuracy
Li [69]	Singapore national eye center	100%
Proposed method	ZUEYE	100%

4.5 Conclusion

In this chapter, we described a color image segmentation system that can extract major features of the retina for use in the diagnosis of diabetic retinopathy. The system accuracy is satisfied in DR screening in large populations. There are two advantages of our scheme. First, it can suppress the interaction among features during feature extraction. Second, it is efficient because it extracts all features in a single flow, which allows us to use earlier extracted features such as bright lesions and red lesions in the extraction of features later in the flow such as vessels, optic disks, and foveae. The experimental results show first erasing bright lesions and red lesions improves the extraction of vessels and that erasing bright lesions and accurate segmentation of vessels improves the extraction of optic disks. Further, the correct location of optic disks can provide a useful constraint for the foveae location and extraction.

Chapter 5 Conclusion and Future Work

5.1 Conclusion

Images of the ocular fundus, also known as images of the retina, can tell us about retinal, ophthalmic, and even systemic diseases such as diabetes, hypertension, and arteriosclerosis. The use of colour retinal images captured with digital fundus cameras provides a non-intrusive way of screening for retinopathy. A fully automated segmentation of colour retinal images can greatly help in the management of certain diseases, especially diseases like diabetic retinopathy which require the screening of large populations.

This thesis focuses on two major features that can assist in the diagnosis of DR: retinal blood vessel segmentation and segmentation of the major lesions caused by DR. The major contributions of this thesis have first been to describe the major difficulties in vessel segmentation and to propose two novel vessel segmentation methods and second to propose a novel system for segmenting the main regions and lesions of colour retinal images obtained from patients with diabetic retinopathy (DR), as described in the following.

5.1.1. Analysis and two novel vessel segmentation methods

Two initial difficulties in retinal vessel segmentation are first that there is great variation in the width of vessels and second that the contrast of small vessels is weak. To deal with these problems, we proposed a multiscale retinal vessel segmentation scheme, Multiscale Production of Matched Filters (MPMF), that multiplies the responses of matched filters at several scales. Since the vessels will have relatively strong responses to the matched filters along scale space while the background noise

decreases rapidly, scale production can enhance vessels while suppressing noise. We have demonstrated that scale production approach of picking up vessel pixels in the scale production domain is an efficient way to fuse multiscale vessel responses. We have also proposed a simple but effective retinal vessel detection scheme which can segment both wide and thin vessels concurrently with very low computational complexity.

A further difficulty of vessel segmentation is the effect that anatomical (e.g. the optic disc) and pathological features (e.g. lesions) have on each other. Some blobs in the retinal image (such as bright lesions and the optic disc) can lead to the false detection of vessels. This work has proposed a modified matched filter that can suppress false detections caused by bright blobs. Instead of using the traditional matched filter approach, which removes background by subtracting the local mean from the response and then detects vessels by thresholding, we first enhance the retinal image by using Gaussian filters and then use a our proposed double-sided thresholding operation, Modified Matched Filter with Double-Side Thresholding (MMFDST to analyze the local structures of the filtering outputs. The proposed modified matched filter does not respond to non-line edges, which greatly reduces the false detection of vessels. The proposed method has been shown to be able to effectively detect the neovasculars while eliminating many non-vessel edges caused by bright lesions. This is a most desirable property in PDR screening because the edges of bright lesions have large curvatures and can be easily misclassified as neovasculars.

Here we summery the advantages and limitations of MPMF and MMFDST. MPMF is good for small vessel segmentation and vessel width estimation. It is fast so that it is suitable for real time applications such as image mosaicking during

surgery. MPMF is not robust to pathological images but can be used on the well-preprocessed images. MMFDST is robust to pathological images so that it can bed used for the diagnosis of vessel tortuosity and PDR. MMFDST needs further improvement to segment small vessels so that mild PDR can be detected.

5.1.2. A novel system for segmenting the main regions and lesions of colour retinal images obtained from patients with diabetic retinopathy (DR).

This work has also proposed a novel system for segmenting the main regions and the lesions in colour retinal images obtained from patients with diabetic retinopathy (DR). This system for segmenting major objects would be of use in the diagnosis of DR, especially for screening DR in large populations. With sufficiently considering the interaction among different objects, this system organized one efficient working flow to segment all targeted objects.

The proposed system offers two particular advantages. First, it can suppress the interaction among different objects so that false positives can be suppressed. Second, it is efficient because it extract all features in a single flow so that the extraction of bright lesions and red lesions can help the extraction of vessels, optic disks, and foveae. The experimental results show that the extraction of vessels is improved by our scheme because it erases bright lesions and red lesions. Our scheme also improves the extraction of optic disks by erasing bright lesions and accurately segmenting vessels. Further, it improves the extraction of foveae is improved because the correct location of optic disks can provide a useful constraint for the location of foveae.

In summery, our top-down scheme is good for detection of bright lesion, OD, vessel, and fovea but not robust for detection of MA. It provides an image preprocessing method based on digit inpainting which can benefit all present vessel

segmentation methods. But the exemplar based inpainting may not be suitable under very rare circumstance when there is a very large bright lesion and the background illumination varies a lot.

5.2 Future work

In future work, we will continue to focus on retinal vessel segmentation and DR image segmentation.

First of all, we need build a good retinal database. Retinal diagnosis is a medication-related research area where most of works are reported on un-opened code and un-opened database. Therefore the comparison between different methods is difficult. Currently we are working on build a public database with large number of retinal images.

Another concern is the evaluation of retinal vessel segmentation. For a comprehensive testing of the proposed algorithm, it would be more convincing to conduct experiments covering both subjective evaluation and quantitative measures. In fact, the sole quantitative evaluation is not enough for retinal segmentation because it relies on a human labeled “ground truth” and this “ground truth” is not real truth. Therefore the visual inspection is very important for reliable segmentation. Unfortunately such visual inspection cannot be measured quantitatively easily. Currently, many researchers working on retinal vessel segmentation have noticed this problem. Currently we are working on exploring some statistical significance tests that will help assess the impact and significance of the experimental results.

Our future work on retinal vessel segmentation will attempt to improve the ability of our MPMF scheme to deal with bright lesions in pathological images and of our MMFDST scheme to segment small vessels. We hope to do this with a novel filtering scheme that we are currently working on that should be able to combine the

complementary strengths of MPMF and MMFDST. We also hope to advance our current vessel classification process which, as it uses only a simple double thresholding, may not make the most of the filtered images. To do this, we are trying to adapt our MPMF and MMFDST to some tracking based [12]--[18] and supervised methods [9][16][19][50].

Our current DR image segmentation scheme can accurately extract vessels, optic discs, foveae, and bright lesions but it does not do so well in extracting microaneurysms. This is in part because the Frame and Spencer scheme [41][42] that we apply after erasing of bright lesions is effective on FA images but no as good on color retinal images. To improve the extraction of microaneurysms, we will focus on the segmentation of hemorrhages, red lesions of unpredictable size and shape. The extraction of hemorrhages should provide more useful diagnostic features and appropriate learning methods.

Currently we are working on producing a fundus diagnosis system by combing and improving the techniques discussed in this thesis. Figure 5.1 illustrates this system. The Black boxes are finished work and the blue boxes are works on-going.

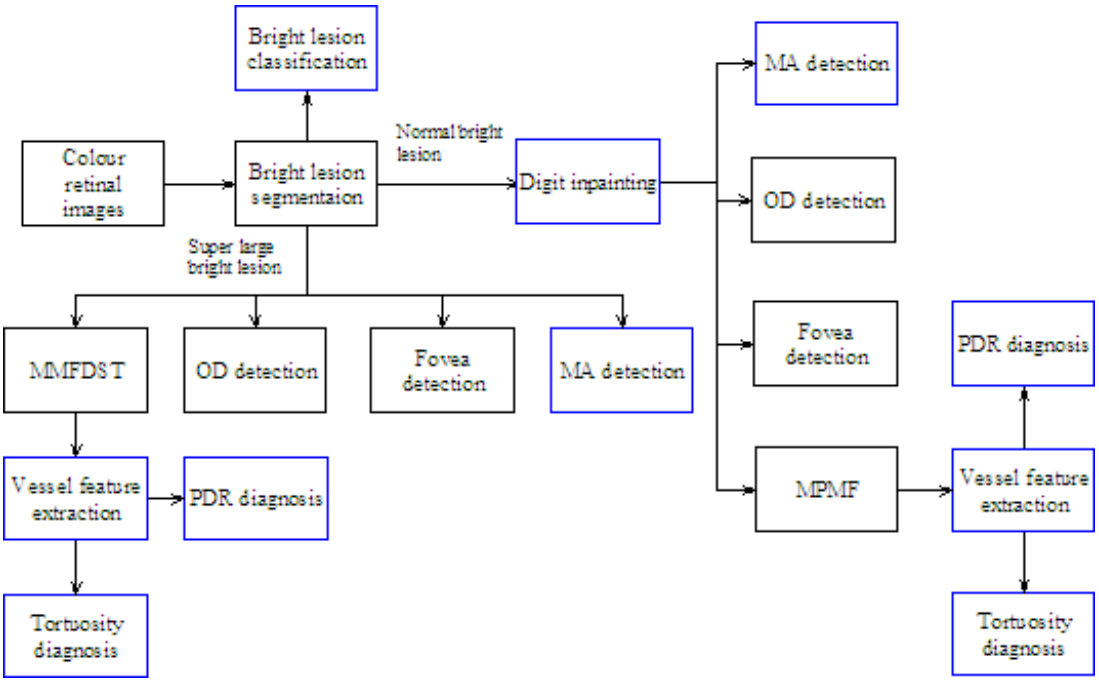

Figure 5.1. Future work.

References/Bibliographies

[1] ONJOPH.COM, Online Journal of Retinopathy, available at http://www.atlasophthalmology.com/.

[2] Structured Analysis of the Retina, available at www.parl.clemson.edu/stare.

[3] S. Chaudhuri, S. Chatterjee, N. Katz, M. Nelson, M.Goldbaum, "Detection of Blood Vessels in Retinal Images Using Two-Dimensional Matched Filters," *IEEE Transactions on Medical Imaging*, vol. 8, pp. 263-269, 1989.

[4] Michael Goldbaum, Saied Moezzi, Adam Taylor, Shankar Chatterjee, Jeff Boyd, Edward Hunter, and Ramesh Jain, "Automated Diagnosis and Image Understanding With Object Extraction, Object Classification, And Inferencing In Retinal Images," *IEEE conference on ICIP*, 1996.

[5] R. Pai, "Automated Diagnosis of Retinal Images Using Evidential Reasoning," *Master's thesis*, Elec. & Comp. Engineering Dept., Clemson University, 2001.

[6] R. Pai, A. Hoover, and M. Goldbaum, "Automated Diagnosis of Retinal Images Using Evidential Reasoning," *International Conference on SEng,* 2002.

[7] Website for EyeCheck project initiated by Dr. Michael Abràmoff, http://www.isi.uu.nl/Research.

[8] M. Abràmoff and M. Suttorp, "Web-based screening for diabetic retinopathy in a primary care population: The eye check project," *Telemedicine e-Health*, vol. 11, no. 6, 2005.

[9] J. J. Staal, M. D. Abràmoff, M. Niemeijer, M. A. Viergever, and B. van Ginneken, "Ridge based vessel segmentation in color images of the retina," *IEEE Transactions on Medical Imaging*, vol. 23, no. 4, pp. 501–509, Apr. 2004.

[10] M. Niemeijer, B. van Ginneken, J. Staal, M. S. A. S. Schulten, and M. D. Abramoff, "Automatic detection of red lesions in digital color fundus photographs," *IEEE Transactions on Medical Imaging*, vol. 24, no. 5, pp. 584–592, 2005.

[11] J. Kanski, S. Milewski, B. Damato, V. Tanner, *Diseases of the Ocular Fundus*, Elsevier Mosby, 2004.

[12] E. J. Sussman, W. G. Tsiaras, and K. A. Soper, "Diagnosis of diabetic eye disease," *J. Am. Med. Assoc.*, vol. 247, pp. 3231–3234, 1982.

[13] D. Klonoff and D. Schwartz, "An economic analysis of interventions for diabetes," *Diabetes Care*, vol. 23, no. 3, pp. 390–404, 2000.

[14] G. Bresnick, D. Mukamel, J. Dickinson, and D. Cole, "A screening approach to the surveillance of patients with diabetes for the presence of vision-threatening retinopathy," *Opthalmology*, vol. 107, no. 1, pp.19–24, 2000.

[15] C. P. Wilkinson, Frederick L. Ferris, Ronald E. Klein, Paul P. Lee, Carl David Agardh, Matthew Davis, Diana Dills, Anselm Kampik, R. Pararajasegaram and Juan T. Verdaguer, “Proposed international clinical diabetic retinopathy and diabetic macular edema disease severity scales”, *Ophthalmology*, vol. 110, Issue 9, pp. 1677-1682, Sep. 2003.

[16] J. V. B. Soares, J. J. G. Leandro, R. M. Cesar Jr., H. F. Jelinek, and M. J. Cree, “Retinal Vessel Segmentation Using the 2-D Gabor Wavelet and Supervised Classification,” *IEEE Transactions on Medical Imaging*, vol. 25, no. 9, pp. 1214–1222, Sep. 2006.

[17] C. Heneghan and J. Flynn and M. O'Keefe and M. Cahill, “Characterization of changes in blood vessel width and tortuosity in retinopathy of prematurity using image analysis,” *Medical Image Analysis*, vol. 6, pp. 407-429, Dec. 2002.

[18] R. Gelman and M. E. Martinez-Perez and D. K. Vanderveen and A. Moskowitz and A. B. Fulton, "Diagnosis of Plus Disease in Retinopathy of Prematurity Using Retinal Image multiScale Analysis", *Investigative Ophthalmology and Visual Science*, Vol. 46, pp. 4734-4738, 2005.

[19] R. Nekovi and Y. Sun, “Back-Propagation Network and its Configuration for Blood Vessel Detection in Angiograms,” *IEEE Transactions on Neural Networks*, vol. 6, no. 1, Jan. 1995, pp. 64-72.

[20] A. Hoover, V. Kouznetsova, and M. Goldbaum, “Locating Blood Vessels in Retinal Images By Piecewise Threshold Probing of A Matched Filter Response,” *IEEE Transactions on Medical Imaging*, vol. 19, no. 3, pp. 203–210, Mar. 2000.

[21] Pinz, S. Bernogger, P. Datlinger, and A. Kruger, “Mapping the human retina,” *IEEE Transactions on Medical Imaging*, vol. 17, pp. 606–619, Aug. 1998.

[22] D. Wu, M. Zhang, J. C. Liu, and W. Bauman, “On the Adaptive Detection of Blood Vessels in Retinal Images”, *IEEE Transactions On Biomedical Engineering*, Vol. 53, No. 2, pp. 341-343, Feb. 2006.

[23] A. M. Mendonça, and A. Campilho, “Segmentation of Retinal Blood Vessels by Combining the Detection of Centerlines and Morphological Reconstruction,” *IEEE Transactions on Medical Imaging*, vol. 25, no. 9, pp. 1200–1213, Sept. 2006.

[24] X. Jiang and D. Mojon, “Adaptive local thresholding by verification based multithreshold probing with application to vessel detection in retinal images,” *IEEE Transactions on Pattern Analysis and. Machine Intelligence*, vol. 25, no. 1, pp. 131–137, Jan. 2003.

[25] S. Tamura, Y. Okamoto, and K. Yanashima, “Zero-crossing interval correction in tracing eye-fundus blood vessels,” *Pattern Recognition*, vol. 21, no. 3, pp. 227–233, 1988.

[26] Y. Tolias and S. Panas, “A fuzzy vessel tracking algorithm for retinal images based on fuzzy clustering,” *IEEE Transactions on Medical Imaging*, vol. 17, pp. 263–273, Apr. 1998.

[27] A. Can, H. Shen, J. N. Turner, H. L. Tanenbaum, and B. Roysam, "Rapid automated tracing and feature extraction from retinal fundus images using direct exploratory algorithms," *IEEE Transactions on Information Technology in Biomedicine*, vol. 3, no. 2, pp. 125–138, Jun. 1999.

[28] I. Liu and Y. Sun, "Recursive tracking of vascular networks in angiograms based on the detection-deletion scheme," *IEEE Transactions on Medical Imaging*, vol. 12, no. 2, pp. 334–341, Jun. 1993.

[29] T. McInerney and D. Terzopoulos, "T-snakes: Topology adaptive snakes," *Medical Image Analysis*, vol. 4, pp. 73–91, Jun. 2000.

[30] R. Toledo, X. Orriols, X. Binefa, P. Radeva, J. Vitrià, and J. Villanueva, "Tracking of elongated structures using statistical snakes," i*n IEEE Conference on CVPR*, 2000, vol.1, p. 1157.

[31] S. R. Aylward and E. Bullitt, "Initialization, noise, singularities, and scale in height ridge traversal for tubular object centerline extraction," *IEEE Transactions on Medical Imaging*, vol. 21, no. 2, pp. 61-75, Feb. 2002.

[32] Michal Sofka and Charles V. Stewart, "Retinal Vessel Centerline Extraction Using Multiscale Matched Filters, Confidence and Edge Measures," *IEEE Transactions on Medical Imaging*, vol. 25, no. 12, pp. 1531-1546, Dec. 2006.

[33] M. E. Martínez-Pérez, A. D. Hughes, A. V. Stanton, S. A. Thom, A.A. Bharath, and K. H. Parker, "Retinal blood vessel segmentation by means of scale-space analysis and region growing," *in Proc. 2nd MICCAI*, 1999, pp. 90–97.

[34] M. E. Martínez-Pérez, Alun D. Hughes, Simon A. Thom, "Segmentation of blood vessels from red-free and fluorescein retinal images", *Medical Image Analysis*, vol. 11, pp. 47-61, Feb. 2007.

[35] Benson Shu Yan Lam and Hong Yan, "A Novel Vessel Segmentation Algorithm for Pathological Retina Images Based on the Divergence of Vector Fields," *IEEE Transactions on Medical Imaging*, vol. 27, no. 2, pp. 237-246, Feb. 2008.

[36] F. Zana and J.-C. Klein, "Segmentation of vessel-like patterns using mathematical morphology and curvature evaluation," *IEEE Transactions on Image Processing*, vol. 10, no. 7, pp. 1010–1019, Jul. 2001.

[37] A. Frangi, W. J. Niessen, K. L. Vincken, and M. A. Viergever, "Multiscale vessel enhancement filtering," *in Proc. 1st MICCAI*, 1998, pp. 130–137.

[38] M. Niemeijer, J. Staal, B. van Ginneken, M. Loog, and M. D. Abràmoff, J. M. Fitzpatrick and M. Sonka, Eds., "Comparative study of retinal vessel segmentation methods on a new publicly available database," *SPIE Med. Imag.*, vol. 5370, pp. 648–656, 2004.

[39] A. A. A. Youssif, A. Z. Ghalwash, and A. S. Ghoneim, "Comparative study of contrast enhancement and illumination equalization methods for retinal vasculature segmentation," *the 3rd Cairo Int. Biomed. Eng. Conf. (CIBEC'06)*, Cairo, Egypt, Dec. 21–24, 2006.

[40] A. A. A. Youssif, A. Z. Ghalwash, and A. S. Ghoneim, "Automatic segmentation of the retinal vasculature using a large-scale support vector machine," *in 2007 IEEE Pacific Rim Conf. Commun., Computers Signal Process.*, Victoria, BC, Canada, Aug. 22–24, 2007.

[41] T. Spencer, J. Olson, K. McHardy, P. Sharp, and J. Forrester, "An image processing strategy for the segmentation and quantification in fluorescein angiograms of the ocular fundus," *Comput. Biomed. Res.*, vol. 29, pp. 284–302, 1996.

[42] A. Frame, P. Undrill, M. Cree, J. Olson, K. McHardy, P. Sharp, and J.Forrester, "A comparison of computer based classification methods applied to the detection of microaneurysms in ophthalmic fluorescein angiograms," *Comput. Biol. Med.*, vol. 28, pp. 225–238, 1998.

[43] M. Cree, J. Olson, K. McHardy, P. Sharp, and J. Forrester, "A fully automated comparative microaneurysm digital detection system," *Eye*, vol. 11, pp. 622–628, 1997.

[44] Alan D. Fleming, Sam Philip, Keith A. Goatman, John A. Olson, and Peter F. Sharp, "Automated Microaneurysm Detection Using Local Contrast Normalization and Local Vessel Detection," *IEEE Transactions on Medical Imaging*, vol. 5, no. 9, pp. 1223-1232, 2006.

[45] H. Wang, W. Hsu, K. G. Goh, and M. Lee. "An effective approach to detect lesions in color retinal images," *IEEE Conference on Computer Vision and Pattern Recognition*, pp. 181-186, 2000.

[46] T. Walter, J. C. Klein, P. Massin, and A. Erginay, "A contribution of image processing to the diagnosis of diabetic retinopathy detection of exudates in color fundus images of the human retina," *IEEE Transactions on Medical Imaging*, vol. 21, no. 10, 2002.

[47] Anantha Vidya Sagar, S.Balasubramaniam, V.Chandrasekaran, "A Novel Integrated Approach Using Dynamic Thresholding and Edge Detection (IDTED) for Automatic Detection of Exudates in Digital Fundus Retinal Images," *IEEE Conference on Computing: Theory and Applications*, 2007.

[48] X. Zhang, O. Chutatape, "Detection and classification of bright lesions in color fundus images," *IEEE International Conference on Image Processing*, vol. 1, pp. 139-142, 2004.

[49] X. Zhang, O. Chutatape, "Top-Down and Bottom-Up Strategies in Lesion Detection of Background Diabetic Retinopathy," *CVPR*, vol. 2, pp. 422-428, 2005.

[50] C. Sinthanayothin, J. Boyce, T. Williamson, H. Cook, E. Mensah, S. Lal, and D. Usher, "Automated detection of diabetic retinopathy on digital fundus images," *Diabetic Med.*, vol. 19, pp. 105–112, 2002..

[51] Bernhard M. Ege, Ole K. Hejlesen, Ole V. Larsen, Karina Møller, Barry Jennings, David Kerr and David A. Cavan, "Screening for diabetic retinopathy using computer based image analysis and statistical classification," *Computer Methods and Programs in Biomedicine*, Volume 62, Issue 3, pp. 165-175, July 2000.

[52] A. D. Fleming, S. Philip, K. A. Goatman, J. A. Olson, and P. F. Sharp, "Automated microaneurysm Detection Using Local Contrast Normalization and Local Vessel Detection", *IEEE Transactions on Medical Imaging*, vol. 25, no. 9, September 2006.

[53] T. Walter, P. Massin, A. Erginary, R. Ordonez, C. Jeulin, J. C. Klein, "Automatic Detection of Microaneurysms in Color Fundus Images", *Medical Image Analysis*, vol. 11, pp. 555-566, 2007.

[54] R. C. Gonzales and R. E. Woods, *Digital Image Processing*, Reading: Addison-Wesley Publishing Co., 1993.

[55] J. Canny, "A computational approach to edge detection," *IEEE Transactions on Pattern Recognition and Machine Intelligence*, vol. PAMI-8, pp. 679-698, Nov. 1986.

[56] T.M. Koller, G. Gerig, G. Székely, and D. Dettwiler, "Multiscale Detection of Curvilinear Structures in 2-D and 3-D Image Data," *Fifth Int'l Conf. Computer Vision*, pp. 864-869. Los Alamitos, Calif: IEEE CS Press, 1995.

[57] L.A. Iverson and S.W. Zucker, "Logical/Linear Operators for Image Curves," *IEEE Transactions on Pattern Recognition and Machine Intelligence*, vol. 17, no. 10, pp. 982-996, Oct. 1995.

[58] J.B.A. Maintz, P.A. van den Elsen, and M.A. Viergever, "Evaluation of Ridge Seeking Operators for Multimodality Medical Image Matching," *IEEE Transactions on Pattern Analysis and Machine Intelligence*, vol. 18, no. 4, pp. 353-365, Apr. 1996.

[59] C. Steger, "An unbiased detector of curvilinear structures," *IEEE Transactions on Pattern Recognition and Machine Intelligence*, vol. 20, pp. 113--125, Feb. 1998.

[60] J. H. Van Deemter and J. M. H. Du Buf, "Simultaneous Detection of Lines and Edges Using Compound Gabor Filters," *International Journal of Pattern Recognition and Artificial Intelligence*, vol. 14, no. 6, pp. 757-777, 2000.

[61] Z.-Q. Liu, J. Cai, and R. Buse, *Handwriting Recognition: Soft Computing and Probabilistic Approaches*, pp. 31-57, Springer, Berlin, 2003.

[62] J.G. Daugman, "Uncertainty relation for resolution in space, spatial frequency, and orientation optimized by two-dimensional visual cortical filters," *Journal of the Optical Society of America A*, vol. 2, pp. 1160-1169, 1985.

[63] S. Theodoridis and K. Koutroumbas, *Pattern Recognition*, 1st ed.Burlington,, MA: Academic, 1999.

[64] R. O. Duda, P. E. Hart, and D. G. Stork, *Pattern Classification*. New York: Wiley, 2001.

[65] C. Sinthanayothin, J. Boyce, H. Cook, T. Williamson, "Automated localisation of the optic disc, fovea and retinal blood vessels from digital colour fundus images," *British Journal of Ophthalmology*, vol. 83 (8), pp. 902–910, 1999.

[66] T. Walter and J.-C. Klein, "Segmentation of color fundus images of the human retina: Detection of the optic disc and the vascular tree using morphological techniques," *in Proc. 2nd Int. Symp. Med.* Data Anal., 2001, pp. 282–287.

[67] H. Li and O. Chutatape, "Automatic location of optic disc in retinal images," *in IEEE Int. Conf. Image Process.,* Oct. 7–10, 2001, vol. 2, pp. 837–840.

[68] H. Li and O. Chutatape, “A model-based approach for automated feature extraction in fundus images,” *in 9th IEEE Int. Conf. Computer Vision (ICCV’03)*, 2003, vol. 1, pp. 394–399.

[69] H. Li and O. Chutatape, “Automated Feature Extraction in Color Retinal Images by a Model Based Approach,” *IEEE Transactions on Biomedical Engineering*, vol. 51, no. 2, pp. 246-254, 2004.

[70] M. Lalonde, M. Beaulieu, and L. Gagnon, “Fast and robust optic disc detection using pyramidal decomposition and Hausdorff-based template matching,” *IEEE Transactions on Medical Imaging*, vol. 20, no. 11, pp.1193–1200, Nov. 2001.

[71] A. Osareh, M. Mirmehdi, B. Thomas, and R. Markham, “Classification and localisation of diabetic-related eye disease,” *in 7th Eur. Conf. Computer Vision (ECCV)*, May 2002, vol. 2353, LNCS, pp. 502–516.

[72] A. Osareh, M. Mirmehdi, B. Thomas, and R. Markham, “Comparison of colour spaces for optic disc localisation in retinal images,” *in Proc. 16th Int. Conf. Pattern Recognition*, 2002, pp. 743–746.

[73] A. Osareh, “Automated identification of diabetic retinal exudates and the optic disc,” *Ph.D. dissertation*, Department of Computer Science, Faculty of Engineering, University of Bristol, Bristol, U.K., 2004.

[74] A. Osareh, M. Mirmehdi, B. Thomas, and R Marham,“ Automatic recognition of exudative maculopathy using fuzzy c-means clustering and neural networks,” *in Proc. Medical Image Understanding Analysis Conf.*, July 2001, pp.49-52.

[75] S. F. Barrett, E. Naess, and T. Molvik, “Employing the Hough transform to locate the optic disc,” in Biomed. Sci. Instrum., 2001, vol. 37, pp. 81–86.

[76] R. Abdel-Ghafar, T. Morris, T. Ritchings, and I. Wood, “Detection and characterisation of the optic disc in glaucoma and diabetic retinopathy,” *Med. Image Understand. Anal. Conf.*, London, U.K., Sep. 23–24, 2004.

[77] A. Hoover and M. Goldbaum, “Fuzzy convergence,” *in Proc. IEEE Computer Soc. Conf. Computer Vis. Pattern Recognit., Santa Barbara*, CA, 1998, pp. 716–721.

[78] A. Hoover and M. Goldbaum, “Locating the optic nerve in a retinal image using the fuzzy convergence of the blood vessels,” *IEEE Transactions on Medical Imaging*, vol. 22, no. 8, pp. 951–958, Aug. 2003.

[79] M. Foracchia, E. Grisan, and A. Ruggeri, “Detection of optic disc in retinal images by means of a geometrical model of vessel structure,” *IEEE Transactions Medical Imaging*, vol. 23, no. 10, pp. 1189–1195, Oct. 2004.

[80] J. Lowell, A. Hunter, D. Steel, A. Basu, R. Ryder, E. Fletcher, and L. Kennedy, “Optic nerve head segmentation,” *IEEE Transactions on Medical Imaging*, vol. 23, no. 2, pp. 256–264, Feb. 2004.

[81] K. W. Tobin, E. Chaum, V. P. Govindasamy, T. P. Karnowski, and O. Sezer, Reinhardt, M. Joseph, Pluim, and P. W. Josien, Eds., “Characterization of the optic disc in retinal imagery using a probabilistic approach,” *in Med. Imag. 2006: Image Process.*, 2006, vol. 6144, pp. 1088–1097.

[82] M. D. Abràmoff and M. Niemeijer, "The automatic detection of the optic disc location in retinal images using optic disc location regression," *in Proc. IEEE EMBC 2006*, Aug. 2006, pp. 4432–4435.

[83] M. Niemeijer, M. D. Abràmoff, "Segmentation of the Optic Disc, Macula and Vascular Arch in Fundus Photographs," *IEEE Transactions on Medical Imaging*, vol. 26, no. 1, January 2007.

[84] A. Youssif, A. Ghalwash, and A. Ghoneim, "Optic Disc Detection from Normalized Digital Fundus Images by Means of a Vessels' Direction Matched Filter," *IEEE Transactions on Medical Imaging*, vol. 27, no. 1, January 2008.

[85] T. F. Cootes, C. J. Taylor, D. Cooper, and J. Graham, "Active shape models – Their training and application," *Comput. Vision Image Understand.*, vol. 61, no. 1, pp. 38–59, 1995.

[86] N. P. Ward, S. Tomlinson, and C. J. Taylor, "Image analysis of fundus photographs – The detection and measurement of exudates associated with diabetic retinopathy," *Ophthalmol.*, vol. 96, pp. 80-86, 1989.

[87] R. P. Phillips, J. Forrester, P. Sharp, "Automated detection and quantification of retinal exudates," *Graefe's Archive for Clinical and Experimental Ophthalmology*, Vol. 231, pp.90-94, 1993.

[88] Z. Liu, O.Chutatape and S.Krishnan. Automatic image analysis of fundus photograph, *In Proceedings of 19th IEEE International Conference on Engineering in Medicine and Biology Society*, pages:524-525,1997.

[89] Bernhard M. Ege, Ole K. Hejlesen, Ole V. Larsen, Karina Møller, Barry Jennings, David Kerr and David A. Cavan, "Screening for diabetic retinopathy using computer based image analysis and statistical classification," *Computer Methods and Programs in Biomedicine*, Volume 62, Issue 3, pp. 165-175, July 2000.

[90] A. V. Sagar, S. Balasubramaniam, V.Chandrasekaran, "A Novel Integrated Approach using Dynamic Thresholding and Edge Detection (IDTED) for Automatic Detection of Exudates in Digital Fundus Retinal Images," *IEEE Proceedings of the International Conference on Computing: Theory and Applications (ICCTA'07)*, 2007.

[91] K. Estabridis, R. Figueiredo, "Automatic Detection and Diagnosis of Diabetic Retinopathy," *IEEE ICIP*, pp. 445 – 448, Sept. 2007.

[92] H. Wang, W. Hsu, K. G. Goh, and M. Lee. "An effective approach to detect lesions in color retinal images," *IEEE Conference on Computer Vision and Pattern Recognition*, vol. 2, pp.181-186, Jun. 2000.

[93] C. I. Sanchez, R. Hornero, M. I. Lopez, J.Poza. "Retinal Image Analysis to Detect and Quantify Lesions Associated with Diabetic Retinopathy," *in proceedings of the 26th Annual International Conference of the IEEE EMBS*.

[94] M. Garcia; R. Hornero; C. I. Sanchez, M. I. Lopez, A. Diez, "Feature Extraction and Selection for the Automatic Detection of Hard Exudates in Retinal Images," *IEEE EMBS*, pp. 4969 – 4972, Aug. 2007.

[95] N. Otsu, "A thresholding selection method from gray level histogram", *IEEE Trans.Syst, Man,Cybern,* Vol.9,pp.62-66,1979.

[96] S. Haykin, *Neural Networks: A comprehensive foundation*. Upper Saddle River, NJ: Prentice-Hall International, 1999.

[97] J. C. Bezdek and S. K. Pal, *Fuzzy models for pattern recognition*, IEEE Press, 1991.

[98] M. N. Muller, S. Mika, G. Ratsch, K. Tsuda, and B. Scholkopf, "An introduction to kernel–based learning algorithms," *IEEE Trans. Neural Networks*, vol.12, pp.181- 201, 2001.

[99] S. Abdelazeem, "Microaneurysm detection using vessels removal and circular Hough transform," *in IEEE Proc. 19th Natl. Radio Sci. Conf.*, Alexandria, Egypt, Mar. 2002, vol. 1-2, pp. 421–426.

[100] T. Spencer, R.P. Phillips, P.F. Sharp, J.V. Forrester, "Automated detection and quantification of microaneurysms in fluorescein angiograms," *Graefe's Archive for Clinical and Experimental Ophthalmology*, 1991.

[101] T. Spencer, J. A. Olson, K. C. McHardy, P. F. Sharp, J.V. Forrester, "An image processing strategy for the segmentation and quantification of microaneurysms in fluorescein angiograms of the ocular fundus," *Computers in Biomedical Research*, vol. 29, 284–302, 1996.

[102] A. J. Frame, P. E. Undill, M. J. Cree, J. A. Olson, K. C. McHardy, P. F. Sharp, J. F. Forrester, "A comparison of computer based classification methods applied to the detection of microaneurysms in opthalmic fluorescein angiograms," *Computers in Biomedical Research*, vol. 28, pp. 225–238, 1998.

[103] G. E. Øien, P. Osnes, "Diabetic retinopathy: automatic detection of early symptoms from retinal images," *in Proc. Norwegian Signal Processing Symposium*, September 1995, pp. 135–140.

[104] M. J. Cree, J. A. Olson, K. C. McHardy, P. F. Sharp, and J. V. Forrester, "A fully automated comparative microaneurysm digital detection system," *Eye,* vol. 11, no. 5, pp. 622–628, 1997.

[105] A. M. Mendonc, A. J. Campilho, J. M. Nunes, "Automatic segmentation of microaneurysms in retinal angiograms of diabetic patients," *in Proc. IEEE International Conference of Image Analysis Applications (ICIAP) 1999*, pp. 728–733.

[106] J. Hipwell, F. Strachant, J. Olson, K. McHardy, P. Sharp, and J. Forrester, "Automated detection of microaneuryss in digital red-free photographs: a diabetic retinopathy screening tool," *Diabetic Med.*, vol. 17, pp. 588–594, 2000.

[107] T. Walter, J. C. Klein, "Automatic detection of microaneurysms in color fundus images of the human retina by means of the bounding box closing," *in Lecture Notes in Computer Science (LNCS)*, vol. 2526, pp. 210–220, 2002.

[108] T. Walter, J. C. Klein, "Automatic analysis of color fundus photographs and its application to the diagnosis of diabetic retinopathy," *Handbook of Biomedical Image Analysis: Segmentation Models*, vol. 2. Kluwer Academic/Plenum Publishers, pp. 315–368 (Part B, Chapter 7), 2005.

[109] I. Autio, J. C. Borras, I. Immonen, P. Jalli, E. Ukkonen, “A voting margin approach for the detection of retinal microaneurysms,” *in: Proceedings: Visualization, Imaging and Image Processing*, Spain, September, 2005.

[110] Alan D. Fleming, Sam Philip, Keith A. Goatman, John A. Olson, and Peter F. Sharp, “Automated Microaneurysm Detection Using Local Contrast Normalization and Local Vessel Detection,” *IEEE Transactions on Medical Imaging*, vol. 25, no. 9, pp. 1223-1232, September 2006.

[111] G. G. Gardner, D. Keating, T. H. Williamson, and A. T. Elliott, “Automatic detection of diabetic retinopathy using an artificial neural network: A screening tool,” *Br. J. Ophthalmol.*, vol. 80, no. 11, pp. 940–944, 1996.

[112] P. Pallawala, W. Hsu, M. Lee, S. Goh, “Automated Microaneurysm Segmentation and Detection using Generalized Eigenvectors,” *in Proceedings of the Seventh IEEE Workshop on Applications of Computer Vision (WACV/MOTION)*, 2005.

[113] M. Niemeijer, B. Ginneken, J. Staal, M. Suttorp-Schulten, and M. D. Abràmoff, “Automatic Detection of Red Lesions in Digital Color Fundus Photographs,” *IEEE Transactions on Medical Imaging*, vol. 24, no. 5, pp. 584-592, May 2005.

[114] S. Mallat and S. Zhong, “Characterization of signals from multiscale edges,” *IEEE Trans. Pattern Anal. Machine Intell.*, vol. 14, pp. 710–732, July 1992.

[115] P. Bao and L. Zhang, “Noise Reduction for Magnetic Resonance Image via Adaptive Multiscale Products Thresholding,” *IEEE Trans. Medical Imaging*, vol. 22, pp. 1089-1099, Sept. 2003.

[116] P. Bao, L. Zhang, and X. L. Wu, “Canny Edge Detection Enhancement by Scale Multiplication”, *IEEE Trans. Pattern Analysis and Machine Intelligence*, Vol. 27, No. 9, Sept. 2005.

[117] K. S. Miller, *Multidimensional Gaussian Distributions*, New York: Wiley, 1964.

[118] T. Chan and J. Shen, *Image processing and analysis: variational, PDE, wavelet, and stochastic methods*. Philadelphia, PA: Soc. Indust. Appl. Math., 2005.

[119] J. A. Sethian, *Level Set Methods: Evolving Interfaces in Geometry, Fluid Mechanics, Computer Vision and Materials Sciences*. Cambridge, U.K.: Cambridge Univ. Press, 1996.

[120] S. Osher and R. Fedkiw, *Level Sets Methods and Dynamic Implicit Surfaces.* New York: Springer, 2003.

[121] Antonio Criminisi, Patrick Perez, Kentaro Toyama. “Object Removal by Exemplar-based Inpainting,” *CVPR*, 2003.

[122] T. Lindeberg, “Feature detection with automatic scale selection,” *Int. J. Comp. Vis.*, vol. 30, pp. 79–116, Nov. 1998.